



TECHNISCHE
UNIVERSITÄT
DRESDEN



Forschungszentrum
Dresden Rossendorf

Structural and transport property changes in austenitic stainless steel induced by nitrogen incorporation

Dissertation

zur Erlangung des akademischen Grades
Doctor rerum naturalium (Dr. rer. nat.)

vorgelegt von

Andrius Martinavičius

geboren am 25.09.1980 in Kaunas, Litauen

Supervisor: Prof. Dr. Wolfhard Möller

Fakultät Mathematic und Naturwissenschaften
der Technischen Universität Dresden

2010

Defect wind does not blow too far.

Prof. Dr. Wolfhard Möller

Acknowledgments

First and foremost I want to thank my supervisor Prof. Dr. Wolfhard Möller for his confidence in me, for his useful advices and valuable discussions, for his patients, and the exhausting proofreading of this thesis.

Special thanks to Dr. Gintautas Abrasonis for his intensive support, the code of the trapping-detrapping model, for keeping my motivation, and for pushing me to take yet another step into the unknown “forest” of science.

I want to thank Prof. Dr. Claude Templier for teaching me how to polish single crystals of austenitic stainless steel and actually helping to polish them. Thanks for valuable discussions and plasma nitriding experiments. I am grateful to him for doing the difficult task of reporting on this work.

I would like to thank the four department leaders to whom I belonged during these years: Prof. Dr. Andreas Kolitsch (FWII), Prof. Dr. Jürgen Faßbender (FWIN), Dr. Silke Merchel (FWIA) and Dr. Sibylle Gemming (FWIO).

My experimental work would be impossible without help of Romy Aniol who did the exhausting polishing of single crystals by hand. Many thanks to Dr. Jean-Charles Stinville for plasma nitriding experiments and EBSD measurements. I would like to express sincere thanks to Dr. Andreas C. Scheinost for a big help on the EXAFS analysis. In regards to the NRA measurements, I thank Dr. Rainer Grötzschel, former head of Ion Beam Analysis division, who kindly helped me with all sorts of NRA measurement problems, and the Tandetron team — Steffen Klare, Axel Weise, Andreas Vetter and Rene Mester. I know you did your best to give me the deuterium beam as stable as possible. In addition I want to thank Andreas Vetter for the “magical” liquid (Polyvinyl acetate) which fixed the leak in my vacuum chamber. Thanks to Andreas Henschke for help dealing with vacuum problems. I am very grateful to Marcel Kosmata for ERDA and to Dr. Georg Talut for Mössbauer measurements.

I want to thank Dr. Matthias Posselt for preparing the MD code for me. Unfortunately, it is not so easy to see a soliton. I am grateful to Dr. Oskar Liedke and Dr. Enric Menéndez for MFM measurements. Sorry that I didn't used them in the thesis. I am grateful for time spent with my office mate Dr. Markus Berndt, and for our memorable trip to the mountain Néron (Grenoble, France). I wish to thank Ph.D. Tim Kunze for his advices on Fortran language and pleasant coffee brakes. I would like to thank Dr. György Kovacs. He has made available his support in a number of ways.

I would like to thank all colleagues at FZD who contributed to the success of this work. My time at FZD was made enjoyable in large part due to the many friends who kept a

company during coffee breaks, lunch times and after-lunch walks.

I gratefully acknowledge the funding sources that made my Ph.D. work possible. I was funded by FZD and partly by the FOREMOST project. I would like to thank FZD additionally for the funding for my synchrotron trip.

I am very grateful to my family for their unending support.

Finally and above all, I would like to thank my wife Jurga and our daughters, Aušra and Giedrė, for their support and understanding, and for being my reason to hurry home after work.

Contents

Acknowledgments	v
Abstract	ix
1 Introduction	1
2 Basic principles and state-of-the-art	3
2.1 Stainless steel	3
2.2 Diffusion	6
2.2.1 Fick's equations	6
2.2.2 Diffusion mechanisms	9
2.3 Phase stability — decomposition	11
2.4 Ion irradiation effects	16
2.5 Stainless steel nitriding	20
2.5.1 History	20
2.5.2 S phase microstructure	21
2.5.3 Nitrogen diffusion in ASS	24
3 Experimental and Modeling Tools	31
3.1 Materials	31
3.2 Nitriding techniques	32
3.2.1 Plasma assisted nitriding	32
3.2.2 Ion beam nitriding	33
3.3 Analysis techniques	36
3.3.1 X-ray diffraction	36
3.3.2 Depth profile measurements	38
3.4 Chemical state and local coordination	41
3.4.1 Conversion Electron Mössbauer Spectroscopy	41
3.4.2 X-ray absorption spectroscopy	43
3.5 Modeling of the nitrogen depth profiles	51

3.5.1	Trapping-detrapping model	51
3.5.2	Fitting parameters	52
3.5.3	Evaluation of the fit	54
4	Structure and Composition	57
4.1	Introduction	57
4.2	Experimental	57
4.3	Results	58
4.3.1	Phase structure	58
4.3.2	Nitrogen depth profiles	59
4.3.3	Local environment	60
4.4	Discussion	76
4.5	Summary	81
5	N diffusion anisotropy in ASS	83
5.1	Experimental	83
5.2	N diffusion dependence on the crystal orientation	84
5.2.1	Phase structure	84
5.2.2	Lattice rotation	85
5.2.3	Nitrogen depth profiles	86
5.2.4	Fitting of the experimental profiles	88
5.3	Nitrogen diffusion: Dependence on the temperature	91
5.4	Influence of ion flux and energy on N diffusion	94
5.5	Discussion	99
5.6	Summary	106
6	Conclusions and Outlook	109
	References	123
	Erklärung	125

Abstract

The saturation of the near surface layers of metals with different elements is a powerful tool to change their surface properties. In this work, structure and transport changes induced by incorporation of large amounts of nitrogen at moderate temperatures ($\sim 370 - 430^\circ\text{C}$) in austenitic stainless steel are investigated. The structural study of the plasma nitrided ASS has been carried out using a combination of global (X-ray diffraction, nuclear reaction analysis) and local probe techniques (Mössbauer, X-ray absorption near edge structure, extended X-ray absorption fine structure spectroscopies). It reveals that nitriding at moderate temperatures ($\sim 400^\circ\text{C}$) results in the nitrided layer with Fe, Cr and Ni being in different local chemical environments: Cr in the CrN-like state, Fe in the Fe_4N -like state, Ni in the metallic state. The results demonstrate that the incorporation of interstitial nitrogen destabilizes homogeneous distribution of the ASS constituents, which leads to the segregation of the elements into small zones rich in Cr and Ni and provide strong evidence that the decomposition is of a spinodal nature. These experimental findings contradict the widely accepted view that the phase formed during nitriding at moderate temperatures is a homogeneous supersaturated nitrogen solid solution.

The nitrogen atomic transport study has been carried out by using ion beam nitriding of single-crystalline stainless steel, and the issues of the influence of the crystalline orientation, nitriding temperature, ion flux and ion energy are addressed. The diffusion coefficients have been extracted from the fitting of the nitrogen depth profiles by using the trapping-detrapping model. It is shown that the crystalline orientation plays a significant role in nitrogen diffusion: the penetration depth is largest, intermediate and lowest for the (001), (110) and (111) orientation, respectively. The pre-exponential factor D_0 varies by two orders of magnitude depending on the orientation, while the activation energy E is similar (~ 1.1 eV) for the (111) and (110) orientations and higher for the (001) orientation (~ 1.4 eV). It is found that the nitrogen ion energy and the flux have the effect on the nitrogen transport in the bulk with higher energies (or fluxes) showing larger diffusion coefficients. The ion energy effect is more pronounced for the (001) than for the (111) orientation, while the flux effect is similar in both orientations. In addition, the diffusivity during post-nitriding thermal annealing without ion irradiation is found to be independent of the crystalline orientation. The observed radiation enhanced diffusion and anisotropy are discussed on the basis of nitrogen incorporation induced changes in the matrix structure (ASS decomposition and formation heterogeneous structure), ion bombardment induced effects (defects, localized vibrations) and correlated diffusion.

1 Introduction

Stainless steels are an important class of alloys due to their excellent corrosion resistance, good strength, ductility, machinability and weldability. Their importance is manifested in the plenitude of applications ranging from low-end applications, like cooking utensils and furniture, to very sophisticated ones, such as space vehicles.

Unfortunately, stainless steel suffers from extensive wear and fairly low hardness, which hinders a wider applicability of the material and causes problems in the existing applications. In the early- and mid-eighties it was discovered that dissolution of large quantities of nitrogen or carbon in stainless steel at low temperature enhances tribological properties [1–4] without compromising the corrosion behavior [5]. The industrial application of surface-engineered stainless steels is obvious, because the potential of this widely used material is expanded to applications where a combination of corrosion and wear resistance is required. However, the lack of understanding of the forming microstructure and of nitrogen kinetic processes leads to limited reproducibility when successful nitriding of austenitic stainless steel is attempted on an industrial scale.

At treatment temperatures between 350° and 450°C, the modified surface layer consists essentially of a metastable phase, known as supersaturated or expanded austenite γ_N [6–10], S phase [11–13], or m phase [14–16]. Many nitriding approaches were used to produce this phase, including gas nitriding [17–19], plasma nitriding [20–23], plasma immersion ion implantation [6, 7, 24], ion beam implantation [24–27], low-pressure arc discharges [28] and reactive magnetron sputtering [29, 30].

Even though the first report on the S phase by Ichii et al. [31] dates back to 24 years ago and the working conditions to form this phase are now established, its structure is still a matter of debate. It has been suggested that the S phase exhibits a tetragonally distorted face-centred [12, 22], body-centred tetragonal [14, 15, 23, 32] or a triclinic lattice [9]. Recent studies, nonetheless, have suggested a face-centered lattice with elastic deformations (expansion [8], residual stresses depth profile [33]) and plastic deformations (lattice rotation [34], stacking faults [35–37]). Also it is not clear whether the S phase is homogeneous or heterogeneous [38–40]. Nitrogen diffusion kinetics is another fundamental challenge. The influence of alloy composition (especially Cr content) [41–44],

ion energy [2, 3, 8, 24, 25, 45–47], current density [3, 25, 48–50], and crystalline orientation [50–54] on the diffusion rate are still not fully understood. Thus, the understanding of the microstructure of the S phase is of great importance and could shed light on nitrogen transport mechanisms. Such fundamental data are essential to design new process variants, to tailor the process parameters to obtain optimal combinations of materials properties and simulate the development of the hardened case during processing. Also, such data are a prerequisite for the design of new materials with optimized performance towards this class of surface engineering treatments.

The purpose of this work is to study the surface modification induced on austenitic stainless steel during nitriding by techniques that employ ionized environments. The focus is on the identification and characterization of the microstructure of the nitrated layer and the influence of nitriding parameters on the nitrogen diffusion.

From the structure perspective, the S phase is analyzed using the combination of local (Mössbauer, X-ray absorption near edge structure, extended X-ray absorption fine structure spectroscopies) and global probe (X-ray diffraction, nuclear reaction analysis, glow discharge optical emission spectroscopy, scanning electron microscopy) techniques. This combination of techniques allows a direct comparison of the data obtained from the atomic up to macroscopic levels.

From the kinetics perspective, nitrogen diffusion dependencies on the crystal orientation, nitriding temperature, ion energy and flux are systematically investigated. In polycrystals, individual grains with different orientations exhibit different thicknesses of the nitrated layer, which contribute to an averaged depth profile [51, 55]. Thus, in the present work single crystalline ASS is used in experimental investigations of nitrogen diffusion, which allows a more straightforward theoretical interpretation and modeling. Ion beam nitriding is employed extensively, as it provides independent control of the parameters (ion energy and flux).

The work is structured as follows: in Chapter 2 basic considerations about stainless steel properties, diffusion processes, phase stability, ion irradiation effects and the state-of-the-art of nitriding are presented. Chapter 3 describes experimental and analytical methods. Chapter 4 deals with the structure investigation. Chapter 5 is focused on the nitrogen diffusion anisotropy in the stainless steel crystal, and its dependence on the ion energy and flux. Chapter 6 provides conclusions and an outlook.

2 Basic principles and state-of-the-art

2.1 Stainless steel

The word ‘steel’ means that iron constitutes the bulk of the material, while the use of the adjective ‘stainless’ implies absence of staining, rusting or corroding in environments where ‘normal’ steels are susceptible (for instance, in relatively pure, dry air). As chromium is added to steels, the corrosion resistance increases progressively due to the formation of a thin protective film of Cr_2O_3 , the so-called passive layer. With the addition of about 12% Cr, steels have good resistance against atmospheric corrosion, and the popular convention is that this is the minimum level of chromium that must be incorporated in an iron-based material in order to be classified as stainless steel. However, of all steel types, the stainless grades are the most diverse and complex in terms of composition, microstructure and mechanical properties. Stainless steels have found a very wide range of application, ranging from chemical, pharmaceutical and power generation industries on the one hand to less aggressive situations in architecture, domestic appliances and street furniture on the other hand.

Three main types of microstructures exist in stainless steels, i.e., ferritic, austenitic and martensitic. Out of these three main microstructures, stainless steels may be categorized into several main classes [56]. These are:

- Ferritic stainless steels,
- Austenitic stainless steels,
- Martensitic stainless steels,
- Duplex stainless steels,
- Precipitation hardened stainless steels,
- Mn-N substituted austenitic stainless steels.

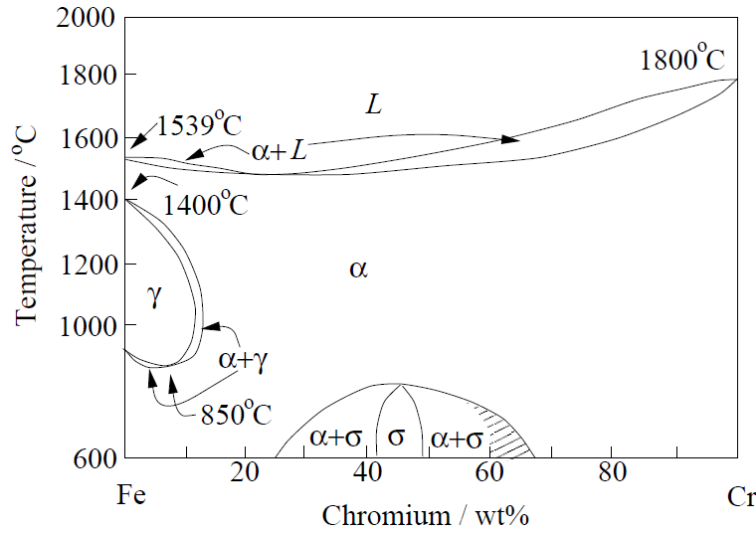


Figure 2.1: The Fe-Cr phase diagram [57].

The phases (crystal structures), which are observed in a simple iron-chromium alloy at ambient pressure (Fig. 2.1), are α , γ and σ : α is referred to as ferrite and is body-centered cubic, γ is commonly referred to as austenite and is face-centered cubic, and σ is an intermetallic compound of iron and chromium and is body-centered tetragonal.

Cr is a ferrite-stabilizer and results mostly in a ferritic structure. However, depending on the heat treatment and exact chemical composition, martensite can also be obtained. The martensite has a body-centered cubic or body-centered tetragonal crystal structure and is formed by a displacive decomposition of austenite. The addition of austenite stabilizing elements in sufficient quantities can allow an austenitic structure to be stable at all temperatures. Nickel is a basic substitutional element used to stabilize austenite. The equilibrium phases depend on the proportion of the Fe, Ni and Cr. Often, alloying elements, either interstitial, such as C and N, or substitutional, such as Mo, Mn, Ti, Nb, V, W, Cu, Al, ... are also used to obtain the required structure. They can be classified as ferrite-stabilizers or austenite-stabilizers, and their effect in this respect is often approximated using notion of chromium and nickel equivalents, calculated by the formulas, such as:

$$\text{Ni}_{eq} = \text{Ni} + \text{Co} + 0.5\text{Mn} + 30\text{C} + 0.3\text{Cu} + 25\text{N} \quad (2.1)$$

$$\text{Cr}_{eq} = \text{Cr} + 2.0\text{Si} + 1.5\text{Mo} + 5.5\text{Al} + 1.75\text{Nb} + 1.5\text{Ti} + 0.75\text{W} \quad (2.2)$$

Here, the composition has to be given in weight%. The use of such formulas is not always straightforward, as they rely on the austenite content, which can be modified by various

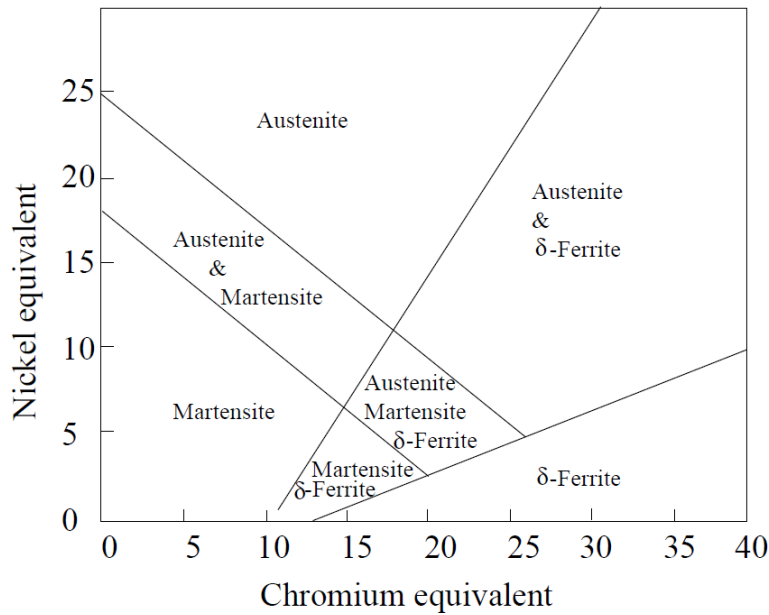


Figure 2.2: Schaeffer-Schneider diagram giving the basic effect of alloying additions on the structure of Cr-Ni stainless steels [58].

precipitation reactions involving these elements. Often stainless steels are classified by reference to the Schaeffer-Schneider diagram (Fig. 2.2). This gives the expected final microstructure for a given composition after cooling from a high temperature.

Increasing the nitrogen concentration in iron and iron alloys is an effective technique to improve mechanical properties of iron alloys, especially stainless steels. The Fe-N system has a rather complex phase diagram whose nitrogen-poor side is shown in Fig. 2.3 [59]. Since all Fe nitrides are metastable with respect to decay into N_2 and Fe, in the phase diagram it is assumed implicitly that the equilibrium nitriding potential is present as required for preventing decay [60]. Atomic nitrogen can be dissolved in α -Fe (*bcc*) to a concentration of about 0.4 at% at 865 K. At concentrations higher than ~ 2.4 at%, the *bcc* Fe lattice undergoes a tetragonal distortion in which the N atoms randomly occupy octahedral interstitial sites in the iron sublattice forming the so-called N-martensite or α' phase. At the Fe_3N stoichiometry, the α' phase can be transformed, by heat treatments at low temperatures, into α'' - $Fe_{16}N_2$, in which the N atoms are ordered.

When iron is in the austenite (γ , *fcc*) state (above 923 K), nitrogen can be dissolved to a maximum concentration of 10.3 at% [59]. The transformation of the iron sublattice from *bcc* to *fcc* also takes place when the γ' - Fe_4N phase, roaldite, is formed. Here, the N atoms occupy one-quarter of the octahedral interstitial sites, which leads to a primitive cubic translation lattice. At even higher concentrations of N, the iron sublattice transforms into a hexagonal phase called ϵ , that can accept N in the concentration range from 25 at%

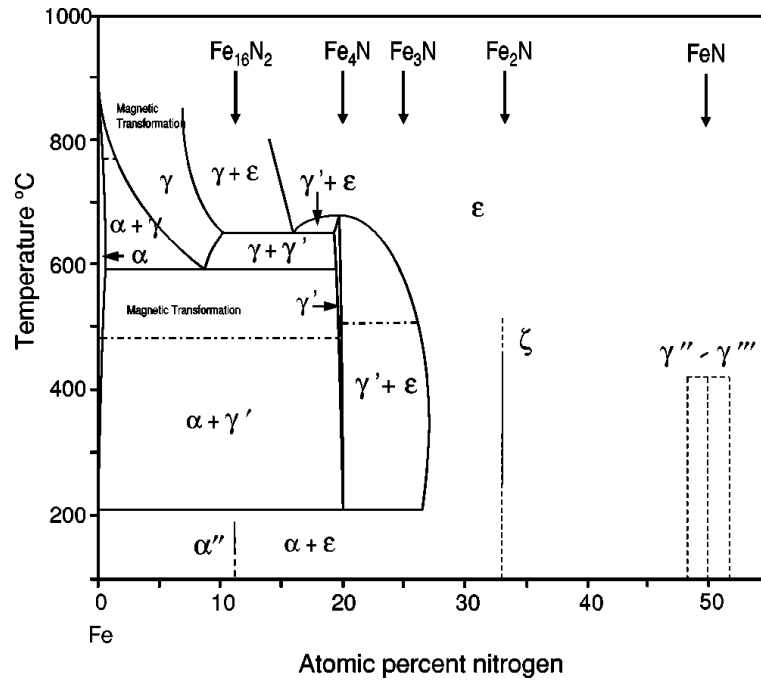


Figure 2.3: Phase diagram of the Fe-N system [59].

up to 33 at%. The N atoms are randomly distributed in the octahedra formed by the Fe sublattice. At the Fe₂N stoichiometry, the ϵ phase can be transformed into ζ -Fe₂N, which has an orthorhombic structure, by ordering the N atoms over the octahedral sites. Although the phases at the nitrogen-rich side are less known, recently the existence of two other cubic Fe-nitride phases have been reported with concentrations near 50 at% [61–64], which are γ'' -FeN with a ZnS type of structure, and γ''' -FeN, with a NaCl type of structure. The Fe sublattice in these phases is also *fcc*.

2.2 Diffusion

2.2.1 Fick's equations

Free diffusion is described by the so-called Fick's laws. These laws represent a continuum description and are purely phenomenological. A deeper physical understanding of diffusion in solids is based on the random walk theory and on the atomic mechanisms of diffusion, which are briefly discussed in the following sections.

The Fick's first law relates the diffusion flux J (number of atoms crossing a unit area per second) to the gradient of the concentration C (number of atoms per unit volume).

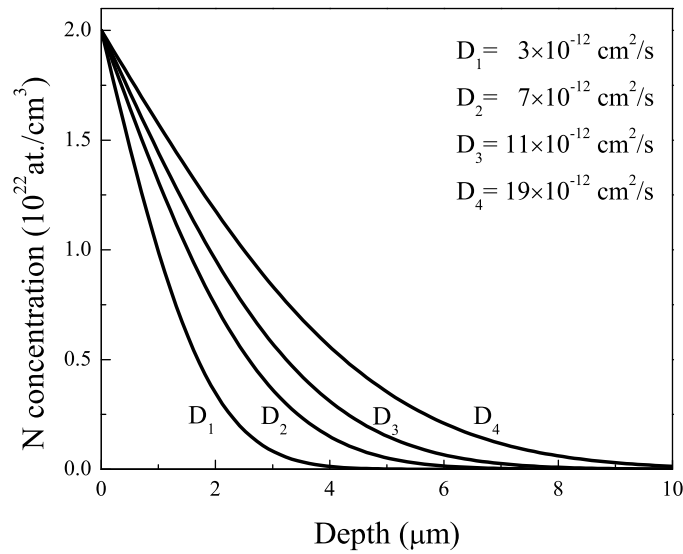


Figure 2.4: A schematic example of the shape of nitrogen depth profiles assuming “simple” nitrogen diffusion, calculated according to Eq. 2.5. $N(0, t) = 2 \times 10^{22}$ at./cm³ and $t = 1$ h.

For an isotropic medium it can be written as

$$J_x = -D \frac{\partial C}{\partial x} \quad (2.3)$$

The negative sign in Eq. (2.3) indicates opposite directions of diffusion flux and concentration gradient. Diffusion is a process which leads to a homogenization of concentration. The factor of proportionality, D , is denoted as the diffusion coefficient, or as the diffusivity of the species considered (the dimension of the diffusivity is length² time⁻¹).

For species that obey a conservation law, Eq. (2.3) can be transformed (assuming concentration independent diffusion) into a second-order partial differential equation often called Fick’s second law

$$\frac{\partial}{\partial t} C(x, t) = -D \frac{\partial^2}{\partial x^2} C(x, t), \quad (2.4)$$

where $C(x, t)$ is the time and depth dependent concentration of diffusing species. Relatively simple analytical solutions of Eq. 2.4 are available for a number of different initial and boundary conditions. A simple case is diffusion at constant surface concentration and zero initial concentration. The solution of Eq. 2.4 is then

$$N(x, t) = N(0, t) \times \left(1 - \operatorname{erf} \frac{x}{2\sqrt{Dt}} \right), \quad (2.5)$$

where erf is the error function. Fig. 2.4 shows depth profiles calculated according to

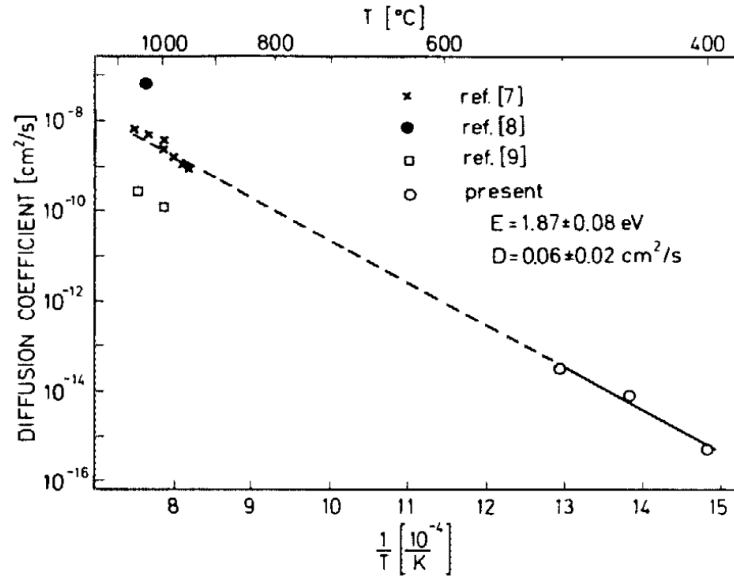


Figure 2.5: Arrhenius plot for diffusion of nitrogen in AISI 316 [66].

Eq. 2.5. The shape of such profile is called error functional. The depth x at which a given concentration is achieved and the amount of diffusing species that is introduced into the substrate per unit area increase with the square root of time, i.e. $x \sim \sqrt{Dt}$.

It is well known that in general diffusion coefficients in solids depend rather strongly on temperature. Empirically, measurements of diffusion coefficients over a certain temperature range may often be described by the Arrhenius relation [65]

$$D = D_0 \exp(-E/kT), \quad (2.6)$$

where E is the activation energy of diffusion, D_0 is the pre-exponential factor, k is the Boltzmann's constant and T is the temperature.

In the Arrhenius diagram the logarithm of the diffusivity is plotted versus the reciprocal temperature T^{-1} (Fig. 2.5). For a diffusion process with a temperature independent activation energy E , the Arrhenius diagram is a straight line with the slope $-E/k$. From its intercept for $T^{-1} \rightarrow 0$ the pre-exponential factor D_0 can be deduced. Such simple Arrhenius behavior, however, is not universal. Departures from it may arise for many reasons, ranging from fundamental aspects of the atomic mechanisms, temperature-dependent activation parameters, effects associated with impurities or microstructural features, such as grain boundaries. Nevertheless, Eq. (2.6) provides a very useful standard.

In an isotropic medium, physical and chemical properties are independent of direction, whereas in anisotropic media properties depend on the direction considered. Diffusion

is isotropic in gases, most liquids, in glassy solids, in polycrystalline materials without texture, and in cubic crystals. In isotropic materials the diffusivity is a scalar quantity. Numerous engineering materials have cubic structures. Examples are face-centered cubic metals (Cu, Ag, Au, Al, Pb, Ni, ...), body-centered cubic metals (V, Nb, Ta, Cr, Mo, W, ...), α -Fe and ferritic steels, which are body-centered cubic, and austenitic steels which are face-centered cubic.

2.2.2 Diffusion mechanisms

In a classical picture, atoms in crystals oscillate around their equilibrium positions. Occasionally these oscillations become large enough to allow an atom to overcome the barrier (activation energy from Eq. (2.6)) and change its site. These random jumps give rise to diffusion in solids. D_0 can be written as

$$D_0 = \beta a^2 \tilde{\nu} f \exp(\Delta S/k) \quad (2.7)$$

with the geometric factor $\beta = 1$ in the *fcc* lattice, the correlation factor $f = 1$ for interstitial diffusion, the lattice parameter a , the vibration frequency $\tilde{\nu} \approx 10^{13} s^{-1}$, and the entropy change ΔS .

Various atomic mechanisms of diffusion in crystals have been identified, and the main ones are briefly described in the following sections.

2.2.2.1 Interstitial diffusion

Solute atoms, which are considerably smaller than the solvent (lattice) atoms (e.g. hydrogen, carbon, nitrogen, and oxygen), are usually incorporated in interstitial sites of a metal. In this way an interstitial solid solution is formed. Interstitial solutes usually occupy octahedral or tetrahedral sites of the lattice (illustrated in Fig. 2.6). Interstitial solutes can diffuse by jumping from one interstitial site to the next. This mechanism is sometimes referred to as direct interstitial mechanism in order to distinguish it more clearly from the interstitialcy mechanism which is when an atom jumps from one substitutional position to another via an interstitial position. Typical activation energy values range from 0.2 eV for H in *bcc* Fe to 1.5 eV for N in *fcc* Fe [67].

2.2.2.2 Substitutional diffusion

Solute atoms, which are similar in size to the host atoms, usually form substitutional solid solutions. The diffusion of substitutional solutes and of solvent atoms themselves

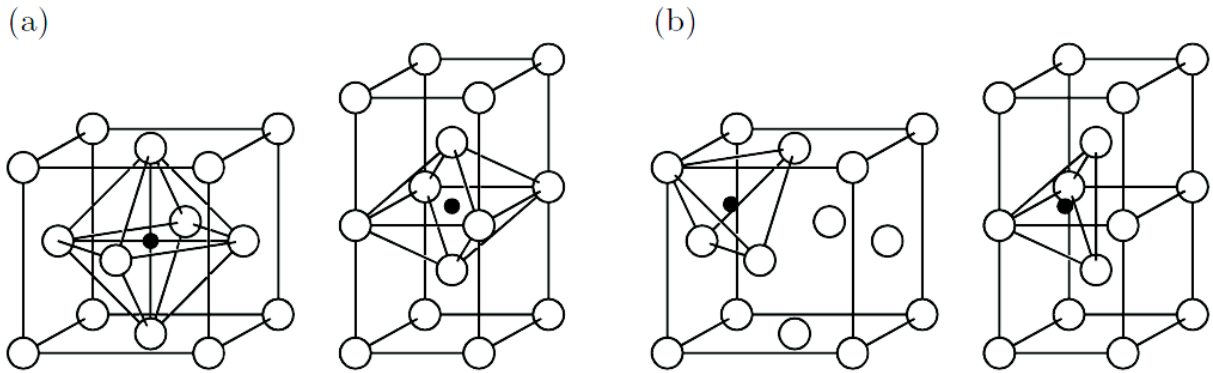


Figure 2.6: Octahedral (a) and tetrahedral (b) interstitial sites in the *fcc* (left) and *bcc* (right) lattice. Lattice atoms (open circles); interstitial sites (full circles).

requires a mechanism different from interstitial diffusion. In the 1930s it was suggested that self- and substitutional solute diffusion in metals occurs by a direct exchange of neighboring atoms, in which two atoms move simultaneously. In a close-packed lattice this mechanism requires large distortions to squeeze the atoms through. This entails a high activation barrier and makes this process energetically unfavorable. Thus practically in all cases vacancies are responsible for self-diffusion and diffusion of substitutional solutes in metals.

An atom diffuses by the vacancy mechanism when it jumps into a neighboring vacancy, so that the vacancy is moved in the opposite direction. The process can be viewed as the migration of either the vacancy or the atom, but the behavior of both is not identical. In a crystal of a pure element, the vacancy can jump towards any of its nearest neighbors at any time, the jumps being independent of each other. This is different for a tagged atom. When it jumps to the vacancy site, the reverse jump has a higher probability than a random jump. Each atom moves through the crystal by making a series of exchanges with vacancies, which from time to time are in its vicinity. Typical activation energy values range from 1.1 eV for Pb in *fcc* Pb to 6.2 eV for W in *bcc* W [67]. For Fe in *fcc* Fe it is 2.9 eV [67].

2.2.2.3 Other mechanisms

More complex mechanisms are possible. A point defect can be less localized than in the simple description. One such concept is the extended interstitial, which, for a string of atoms, is the “crowdion”. Another is a delocalized vacancy, which is just a small disordered or even amorphous zone. Also several elementary mechanisms can be operative simultaneously.

2.3 Phase stability — decomposition

A system is in equilibrium when it is in its most stable state and shows no tendency to change ad infinitum. The system has the lowest possible value of Gibbs free energy, i.e. $dG = 0$. However, there are systems which have configurations with several local minima in the free energy curve, which also satisfy $dG = 0$. Such configurations are in a so-called metastable equilibrium state. The metastability means that the Gibbs free energy of the system is at a local minimum but not at the lowest possible G value of the system. As a result of thermal fluctuation or some other energetic influence, the system in a local minimum may rearrange into a state with the lowest possible Gibbs free energy.

There are two types of phase transformation mechanisms: nucleation and growth and spinodal decomposition [68–71]. Which one of the mechanisms dominates in the decomposition process is commonly assumed to depend on the degree of instability of the initial state of a phase-separating system. The system is metastable if $\partial G/\partial C < 0$ and $\partial^2 G/\partial C^2 \geq 0$, where C is the composition, and the phase transition is supposed to proceed via nucleation and growth [69]. If $\partial^2 G/\partial C^2 < 0$, the system is thermodynamically unstable and the mechanism of spinodal decomposition is expected to govern the phase separation process [68–70].

In the nucleation process, a nucleus of an initially small size is formed stochastically with state parameters widely similar to the properties of the newly evolving macroscopic phases. The nucleus is separated from the parent matrix by a sharp interface. This change can be described as being large in the magnitude of the local change in structure and/or composition but spatially localized to the small fraction of the matrix. The majority of the matrix remains completely untransformed, at least initially, though subsequent growth of the nucleus into the matrix occurs. There is a local change in the free energy which is given, in the usual continuum description, as a decrease in the volume free energy, due to the transfer of atoms from a less stable to a more stable phase, and an increase in the interfacial free energy due to the increase of the area of the interface between the two phases. The total change of the free energy ΔF_t , when a new phase of volume V_β , and interface area A_β , forms is given as [72]:

$$\Delta F_t = V_\beta \Delta F_{\alpha\beta}^V + A_\beta \sigma + V_\beta \Delta F_E^V, \quad (2.8)$$

where σ is the specific energy of the $\alpha - \beta$ interface, ΔF_E^V is an additional increase in elastic strain energy per unit volume of precipitate and $\Delta F_{\alpha\beta}^V$ is the free energy change per unit volume of the new β phase. The first and last terms in Eq. (2.8) are both dependent on the volume of the nucleus and are treated together. The reaction can proceed only

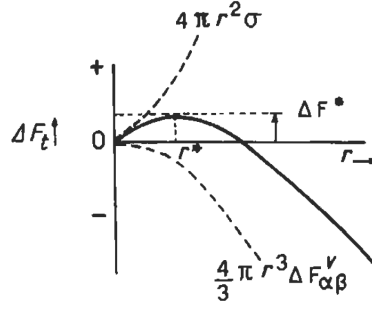


Figure 2.7: Free energy of a sphere of new phase as a function of the radius of the sphere [72].

if the first term is larger (more negative) than the third term, which is always positive. The volume of the nucleus increases as the third power of the nucleus size ($4\pi r^3/3$ if the nucleus is a sphere of radius r), while the area term, which is always positive and acts as the barrier to the process, increases only as the second power of the nucleus size ($4\pi r^2$ a sphere). Fig. 2.7 plots Eq. (2.8) for a spherical nucleus, and shows that at small radii the nucleus shows an increase of ΔF_t . Thus, it is unstable and tends to redissolve in the matrix. Only when the new phase has reached the critical radius r^* , and has acquired the critical free energy increase ΔF^* , the nucleus becomes potentially stable. After the addition of one further atom, $r > r^*$, it can grow with a continuous decrease of free energy. For a spherical nucleus the values of the critical parameters are given by [72]:

$$r^* = -2\sigma / (\Delta F_{\alpha\beta}^V + \Delta F_E^V), \quad (2.9)$$

$$\Delta F^* = \frac{16}{3} \frac{\pi\sigma^3}{(\Delta F_{\alpha\beta}^V + \Delta F_E^V)^2}. \quad (2.10)$$

At equilibrium, the concentration of critical-sized nuclei, n^* in a unit volume is given by [72]:

$$n^* = N^V \exp(-\Delta F^*/kT), \quad (2.11)$$

N^V is the number of atomic sites per unit volume on which the assembly of the nucleus could have started. For homogeneous nucleation this is all atom sites. The rate of nucleation $I_{\alpha\beta}^V$ is then the product of this concentration of critical nuclei and the rate of atomic addition to the nuclei to make them just supercritical [72]:

$$I_{\alpha\beta}^V = n^* A^* \nu \exp(-\Delta F_A/kT), \quad (2.12)$$

where A^* is the number of atomic sites on the surface of the critical nucleus to which

an atom can join after overcoming a growth barrier ΔF_A and ν is the atomic vibration frequency of an atom in the matrix at the interface, usually assumed to be of the order of 10^{13} Hz.

In contrast, spinodal decomposition is characterized by a small initial change in composition in any local region, but where the composition fluctuation is delocalized in space. The result of such a fluctuation is that the region of initially uniform composition develops a composition wave whose amplitude grows with time, but with, at least initially, a constant wavelength.

If D_A^* and D_B^* are the tracer diffusion coefficients of the two components of atomic fractions C_A and C_B , then the interdiffusion coefficient \tilde{D} is given by [72]:

$$\tilde{D} = (C_A D_B^* + C_B D_A^*) \left(1 + \frac{d \ln f_B}{d \ln \nu_B} \right), \quad (2.13)$$

where f_B is the activity coefficient of a B tracer and ν_B is the molar fraction of a B tracer. It can be shown by using standard solution thermodynamics, that [72]:

$$\frac{d^2 F}{dC_B^2} = RT \left(\frac{1}{1 - C_B} + \frac{1}{C_B} \right) \left(1 + \frac{d \ln f_B}{d \ln \nu_B} \right), \quad (2.14)$$

where F is a free energy. From Eqs. (2.13) and (2.14), we obtain:

$$\tilde{D} = (1 - C_B) D_B^* + C_B D_A^* \frac{C_B (1 - C_B)}{RT} \frac{d^2 F}{dC_B^2}, \quad (2.15)$$

$$\tilde{D} = M_D \frac{d^2 F}{dC_B^2}. \quad (2.16)$$

Equations (2.15) and (2.16) define the diffusional mobility M_D .

As a consequence of the sign of D being determined by the sign of $d^2 F/dC_B^2$, a homogeneous solid solution with $d^2 F/dC_B^2 < 0$ is unstable in the presence of an initial infinitesimal fluctuation. Any such sinusoidal perturbations of initially minimal amplitude can grow in amplitude. From the thermodynamics of inhomogeneous solid solutions, a correction for inhomogeneity is introduced as [73]:

$$\left(\frac{dF^V}{dC_B} \right)_{\text{inh}} = \frac{dF^V}{dC_B} - \frac{2K \nabla^2 C_B}{V_m}, \quad (2.17)$$

where V_m is the volume of one mole and K is the gradient-energy coefficient which is determined by the difference in number of like atomic neighbors between an atom in a homogeneous alloy and an atom in an alloy which has a variation in composition. The

change of composition with time, dC/dt , is obtained by substituting Eqs. (2.16) and (2.17) to the Fick's first law (Eq. (2.3)) and calculating the derivative with time. Omitting the subscript:

$$\frac{dC}{dt} = \frac{M_D d^2 F}{\nabla^2 C dC^2} - 2M_D K \nabla^4 C. \quad (2.18)$$

Cahn [74] showed that this differential equation has the following solution:

$$C = C_0 + \exp(R(\beta)t) \cos(\beta r), \quad (2.19)$$

with the initial composition C_0 , the wave number $\beta = 2\pi/\lambda_W$, where λ_W is the wavelength of a particular fluctuation. The ‘‘amplification’’ factor $R(\beta)$ is given by:

$$R(\beta) = -M_D \beta^2 \left(\frac{d^2 F}{dC^2} + 2K\beta^2 \right). \quad (2.20)$$

Since the diffusional mobility M_D is inherently positive, it can be seen, from the term in brackets in Eq. (2.20), that in a system showing unmixing, when K is positive, short-wavelength fluctuations will decay since $K\beta^2 > -d^2 F/dC^2$ for large values of β , but fluctuations below the critical wave number β^* can grow:

$$\beta^* = \left(\frac{d^2 F}{dC^2} \frac{1}{2K} \right)^{1/2}. \quad (2.21)$$

The fastest growing wavelength λ_{\max} is determined from Eqs. (2.19) and (2.20) as the wavelength having the maximum amplification factor $R(\beta)$.

An important addition to the theory comes from considerations of elastic strains that arise when there is a change of lattice parameter with a change of alloy content. With η defined as the unit strain per unit composition difference, $\eta = (da/dC)/a = (d \ln a/dC)$, a is the lattice parameter, Y is Young's Modulus and ν_p is Poisson's ratio, Eq. (2.20) is changed by the elastic strain to [73]:

$$R(\beta) = -M_D \beta^2 \left(\frac{d^2 F}{dC^2} + 2K\beta^2 \right). \quad (2.22)$$

The strain term acts, in addition to the gradient-energy term, to inhibit the separation reaction.

Fig. 2.8 (top) depicts the spinodal decomposition process in $\text{Ti}_{0.46}\text{Al}_{0.54}\text{N}$ alloy [75]. When the system is brought into the spinodal region (annealing at 900°C), concentration waves start to develop. The density of the system has now a wavy profile with maxima

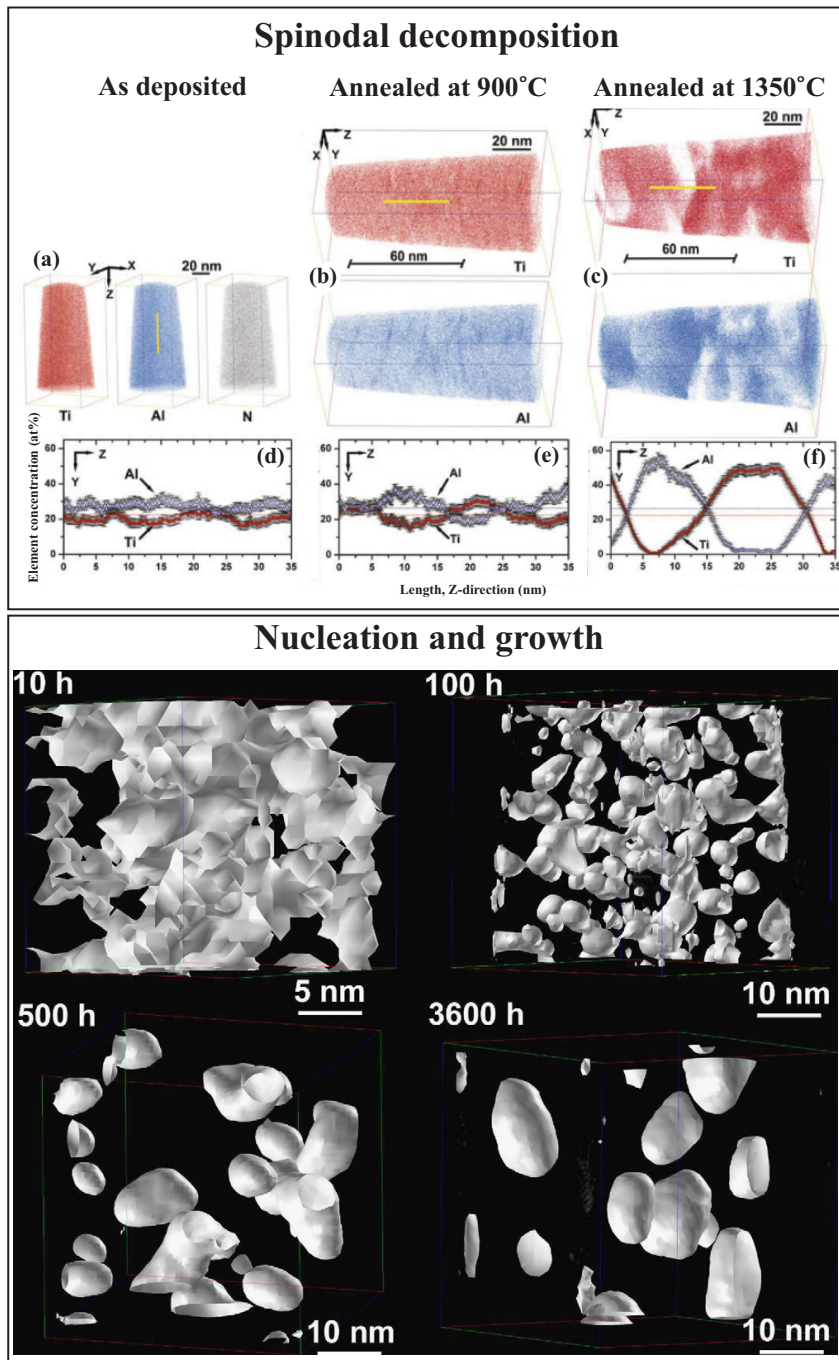


Figure 2.8: (Top) Spinodal decomposition in $\text{Ti}_{0.46}\text{Al}_{0.54}\text{N}$ alloy [75]. (a)-(c) 3D-atom maps of as-deposited, annealed at 900°C and 1350°C $\text{Ti}_{0.46}\text{Al}_{0.54}\text{N}$, obtained by atomic probe tomography, Ti (red), Al (blue) and N (grey) atoms. (d)-(f) 1D element concentration profile along the Z-axis calculated from volumes indicated in (a)-(c). (Bottom) Nucleation and growth of the Cr-enriched α' phase in Fe-based PM 2000TM oxide dispersion strengthened steel [76]. 3D-atom maps of 15% (10 h) and 25% Cr (100, 500 and 3600 h) isoconcentration surfaces after ageing between 10 and 3600 h at 748 K, obtained by atomic probe tomography.

and minima around the average density. After annealing at 1350°C the diffusion does not take place from higher to lower concentration (downhill), but, rather, opposite from lower to higher concentration (uphill), and the amplitude of concentration wave grows. This is the characteristic fingerprint of spinodal decomposition.

Fig. 2.8 (bottom) depicts the nucleation and growth mechanism of Cr-enriched α' phase in Fe-based PM 2000TM oxide dispersion strengthened steel [76]. The alloy contains 18.5 at% of Cr and is brought into unstable region at 475°C. A clear indication of phase separation into Cr-enriched α' and Cr-depleted α regions is evident after ageing for 100 h. Phase separation is finer and less well developed after 10 h. The size of the Cr-enriched α' nucleus is smaller and α' particles form a connected network. After 100 h, the morphology of the Cr-enriched α' phase is spheroidal and the size of the Cr-enriched α' phase increases with further ageing.

2.4 Ion irradiation effects

When energetic ion beams bombard solid surfaces, charged and neutral particles are emitted from the surface, as illustrated in Fig. 2.9(a) [77]. The charged particles include backscattered ions, emitted secondary ions, sputtered ions, etc. An energetic ion penetrating a solid target with an energy E_1 experiences a series of collisions with the target atoms and loses its energy in the process. In a solid target there are two main energy loss mechanisms for interactions between the energetic ion and the target atoms: (i) Nuclear collisions: in this kind of collision the incident ion transfers its energy to the target atom nucleus, the ion may be scattered at a large angle, and the transferred energy may displace lattice atoms. (ii) Electronic collisions: the incident ion excites or ionizes the electrons of the target atom, or causes the atom to capture electrons. Then, scattering angles of the ion are negligible as well as a lattice disordering.

If the energy loss of the implanted ion per unit distance is dE_1/dl , the energy loss of the ion along a path Δl is

$$\Delta E_1 = |dE_1/dl| \Delta l. \quad (2.23)$$

Once dE_1/dl is known, the ion path length in the target material can be calculated:

$$R_t(E_0) = - \int_{E_0}^0 \frac{dE_1}{-dE_1/dl}, \quad (2.24)$$

where E_0 is the initial energy of the ion. For practical purposes the projected range normal to the surface is mostly of interest, as it characterizes the implantation depth. For

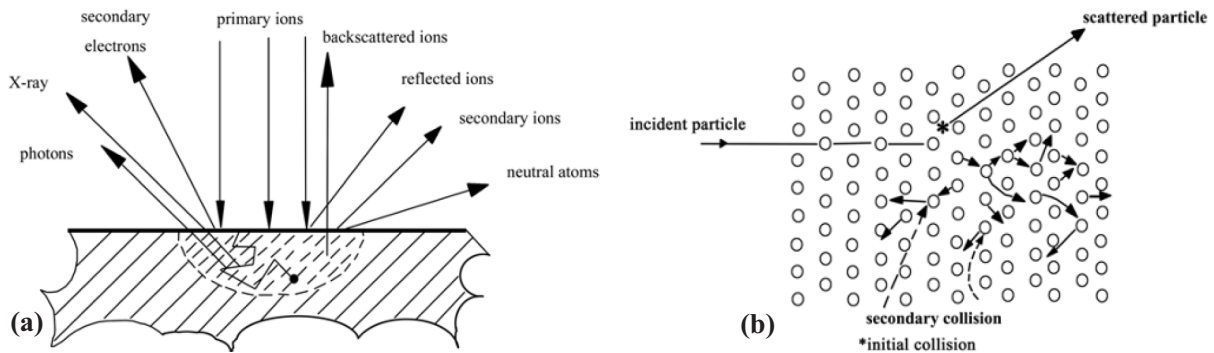


Figure 2.9: (a) Principle of interaction between ions and solid. (b) Collision cascade process [78].

certain regimes of parameters, the mean projected range can be calculated from the mean total path length. However, for more precise data of projected ranges, transport theory calculations or computer simulations of the binary collision approximation type have to be performed.

When an incident ion transfers its energy to target atoms in such a way that the kinetic energies of the particles participating in the collision are conserved, this is called an elastic collision. If the ion transfers energy to electrons, causing excitation or ionization, the mechanical energy of the particles participating in the collision are not conserved, and this is called the inelastic collision. In general, when the ion passes through a solid these two kinds of collision processes occur simultaneously. When the ion energy is high, inelastic collisions dominate, and when the ion energy is low, elastic collisions dominate.

If a lattice atom gains enough energy from a collision to exceed the binding potential that binds the atom to a fixed location in the lattice, the hit atom leaves its original position to enter the space between lattice atoms. This phenomenon is called the atomic displacement. The minimum energy required for the atomic displacement is called the displacement critical energy, denominated by E_d . The energy that every recoiling target atom loses when it leaves its lattice site and recoils in the target is the lattice binding energy E_{latt} . If the energy gained by the atom from the incident ion is far more than the displacement critical energy, the atom can further collide with its neighboring atoms (in a recoil collision) to displace other atoms and form a collision cascade (Fig. 2.9(b)).

Ion irradiation effects can be divided into primary (sputtering, cascade mixing, recoil implantation, etc.) and secondary phenomena (radiation enhanced diffusion, radiation induced segregation). If in the collision cascade atoms at the surface gain energy larger than the surface binding energy E_{surf} , they may be ejected. This phenomenon is called sputtering. The sputtering yield is a characteristic parameter describing sputtering and

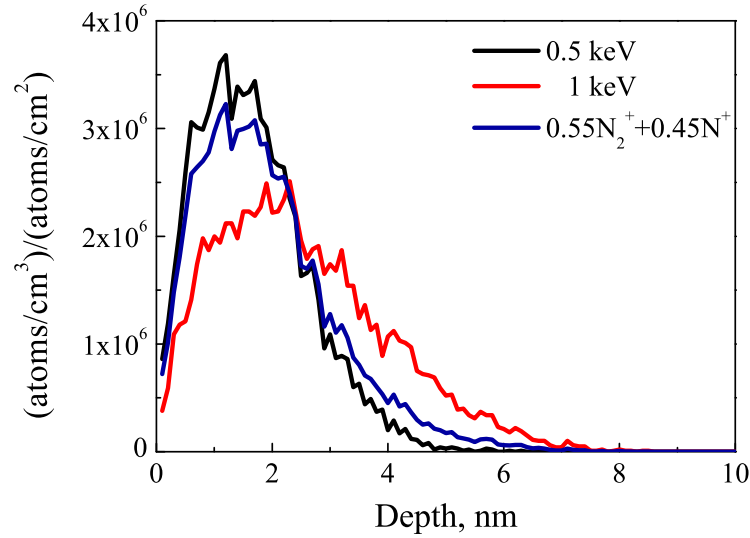


Figure 2.10: Nitrogen ion ranges in iron ($a=0.36$ nm, mass density 7.98 g/cm³) for 0.5 and 1.0 keV N ions, and a mixture assuming 55% of N_2^+ and 45% of N^+ . Calculations performed with SRIM2010 code [79].

is defined as

$$Y_{sp} = \frac{\text{number of sputtered target atoms}}{\text{number of incident ions}}. \quad (2.25)$$

Y_{sp} varies with the energy of the incident ion. The incident ion energy has a critical value below which no sputtering takes place. For most metal target materials this critical value is between ten and several tens of eV. As the incident ion energy increases, Y_{sp} reaches a maximum and then decreases as the incident ion energy is further increased. This can be attributed to a decreasing cross section of elastic collisions and to an increasing range of the implanted ions, so that displaced atoms cannot easily reach the surface.

Sputtering of multicomponent targets, i.e. materials consisting of more than one element, such as alloys or compounds, may change the surface composition due to preferential sputtering of one component. If the energy transfer is more efficient to one of the target components, and/or it is less strongly bound to the solid, it will sputter more efficiently than another. This leads to the formation of an altered layer and may change the total sputtering yield depending on the composition.

Radiation enhanced diffusion is one of the main mechanisms of radiation-stimulated phase changes accelerating the transfer of systems to the equilibrium condition. The diffusion during irradiation may be intensified by the introduction of an excess concentration of interstitial atoms and vacancies. Radiation induced segregation is the segregation under irradiation of different chemical species in an alloy towards or away from defect sinks. Radiation induced segregation occurs when there are persistent fluxes of vacancies

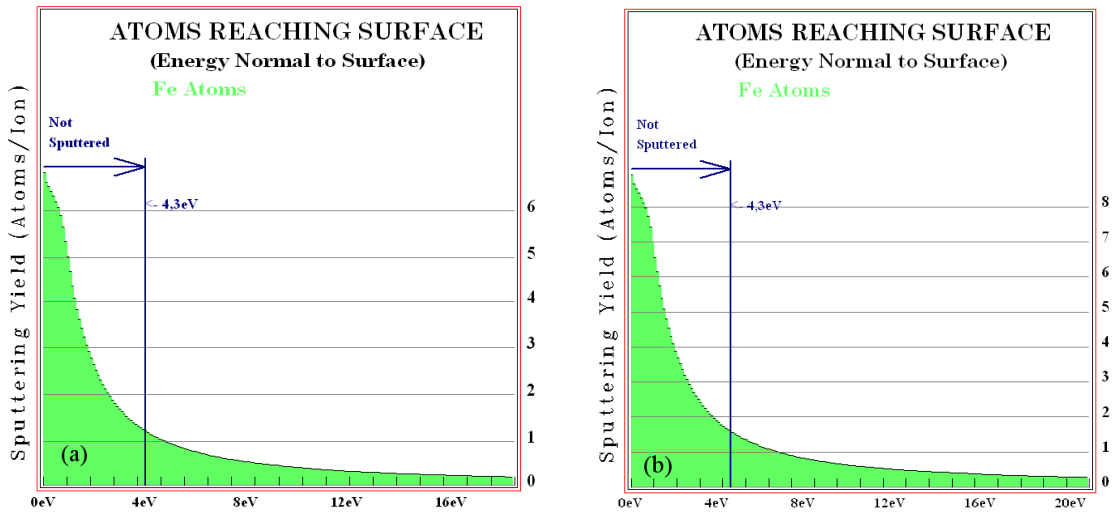


Figure 2.11: The integrated number of the Fe atoms reaching the surface for 0.5 (a) and 1.0 keV (b) N ions. Calculations performed with SRIM2010 code [79].

or interstitials, and some form of coupling between solute fluxes and fluxes of irradiation produced point defects.

Analytical expressions exist for a quantitative description of the above four mechanisms [77]. However, their application often suffers from a complicated structure and a restricted range of validity with respect to ion-substrate combinations and the energy regime. For practical purposes it is often more adequate to use computer simulation programs based on the Monte-Carlo or Molecular-Dynamic simulations. For purely collisional phenomena, one of the mostly used codes is SRIM (Stopping and Range of Ions in Matter) developed by Biersack [79], whose formalism is described by Ziegler [80]. SRIM produces information on the implantation depths, straggling, the number of vacancies and interstitials produced, sputtering yields...

A typical ion acceleration voltage used in the present work was 1 kV. The employed Kaufman ion source produces a nitrogen ion beam which consists of about 55% of N_2^+ and 45% of N^+ . The molecular nitrogen ions split on the surface producing two nitrogen atoms with the energy of 0.5 keV each. Thus, the irradiation effectively takes place with nitrogen atoms of 0.5 keV and 1.0 keV energy, with a share of 71% and 29%, respectively.

Fig. 2.10 shows nitrogen depth profiles for this situation normalized to the ion fluence. The density of the ASS used in these calculations is 7.98 g/cm^3 , which is obtained by assuming that steel consists only of iron atoms with the *fcc* structure and the lattice parameter of 3.6 \AA . The other main alloying elements are Ni and Cr which have masses very close to the iron mass. The default values for the binding energies are $E_d = 25 \text{ eV}$, $E_{surf} = 4.34 \text{ eV}$ and $E_{latt} = 3 \text{ eV}$. The nitrogen depth profile is Gaussian-like, which is

generally the case for small fluences of monoenergetic ions. Fluctuations of the nitrogen concentration versus depth are due to the statistical nature of the simulation. The mean projected range R_p is 1.6 and 2.5 nm for 0.5 and 1.0 keV ions, respectively.

Fig. 2.11 presents the integrated number of matrix atoms reaching the surface with different energies obtained during the elastic collisions in the cascades for the 0.5 and 1.0 keV N ions, respectively. It can be seen that the number of ions, coming to the surface with energies higher than surface binding energy, is relatively low compared to the total number of arriving atoms. The rest of the atoms have energy which is not sufficient to overcome the surface barrier, and they are re-deposited on the surface and become adatoms.

2.5 Stainless steel nitriding

As mentioned in Introduction, enhancement of the surface properties of austenitic stainless steels by nitriding has been a subject of intensive research for the past two decades. A variety of surface treatment techniques [81], such as low temperature plasma nitriding [5, 6, 82], magnetron sputtering [83] and plasma immersion ion implantation [2, 6, 7, 84], have been utilized to incorporate nitrogen into the surface region of stainless steels.

Above 500°C, nitriding, while enhancing wear resistance, degrades the corrosion resistance, because of the precipitation of chromium nitrides. Nitriding below ~450°C prevents the precipitation of nitrides and results in a nitrogen saturated layer. This nitrogen supersaturated layer enhances the hardness by the factor of 5 [21, 85] and the wear rate is reduced by ~2 orders of magnitude [86]. The corrosion resistance is even improved [87]. The nitrided layer also exhibits very interesting magnetic properties [88]. Depending on the amount of nitrogen, it is either paramagnetic [88–91] or ferromagnetic [3, 41, 88, 90, 91].

2.5.1 History

Low temperature plasma nitriding of ASSs was first investigated by two teams in the mid-1980s: Zhang and Bell [92] and Ichii et al [31]. The disagreement on the structure of the nitrogen implanted layer started immediately. Zhang and Bell [92] described it as a nitrogen supersaturated solid solution free from CrN precipitates, while Ichii et al [31] regarded it as a compound layer of metal nitrides. Over the years researchers also showed disagreement on the name. The term S phase was introduced by Ichii et al. [31]. Besides being called the S phase [11, 12, 31], the interstitial-saturated layer is also called expanded or supersaturated austenite [5, 6, 11, 83, 84], or denoted as γ_N [8, 50], the m

phase [15,16,23,32], or S' phase [91]. In this thesis, this thin supersaturated layer is called the S phase, as this is the most frequently used designation in the literature.

2.5.2 S phase microstructure

Incorporation of large nitrogen amounts in ASS results in lattice expansion, which can be up to 10% [93]. The characterization of the S phase using XRD shows the appearance of satellite peaks next to the austenite ones (Fig. 2.12(a)). The peaks shift to lower angles and broaden after nitriding [12,21,94]. It has also been observed that the change in the lattice spacing of the (200) plane is larger than that of the (111), (220), (311) and (222) planes [8,12,37,83,95].

Although there appears to be incipient consensus that the S phase exhibit a face-centered cubic crystallographic structure, the debate on the crystallographic arrangement of this phase is still ongoing. Some researchers [7,8,83] regarded the S phase as face-centered cubic having an expanded lattice parameter due to the incorporation of nitrogen. The afore-mentioned XRD observations, like the more severe change in the lattice spacing of the (200) plane, were explained in terms of the higher diffusion rate of nitrogen [8] and the higher residual stresses [83] associated with the (200) plane. On the other hand, Menthe and Rie [12] and Bacci et al. [22] have suggested that the S phase should possess a tetragonally distorted face-centred lattice. The *fcc* lattice was also ruled out by Marchev et al. [14] who further pointed out the inadequacy of the argument that faster diffusion of nitrogen and higher stresses were associated with the (200) plane. Marchev et al. [14,15,23,32] further concluded that the S phase has a body-centred tetragonal lattice. They also stated that although a high number of stacking faults might lead to the above-mentioned distinct features of the XRD pattern of the S phase, this was not very likely because deviation from the *fcc* XRD pattern occurred even at lower nitrogen levels [14]. A triclinic lattice has also been proposed by Fewell et al. [9]. Nonetheless, recent studies suggest that the S phase has a face-centered lattice with elastic deformations (expansion [8], residual stresses depth profile [33]) and plastic deformations (lattice rotation [34], stacking faults [35–37]).

The controversial results on the S phase structure given in literature in the past 20 years suggest that its microstructural characterization only by XRD is insufficient. Mössbauer spectroscopy has been successfully employed to identify and quantify Fe phases (Fig. 2.12(c)). The characteristic S phase Mössbauer spectra shows broad resonance line-widths, which are attributed to a distribution of hyperfine fields due to the different local N environments around Fe, and probably also due to the presence of the Cr and Ni alloying

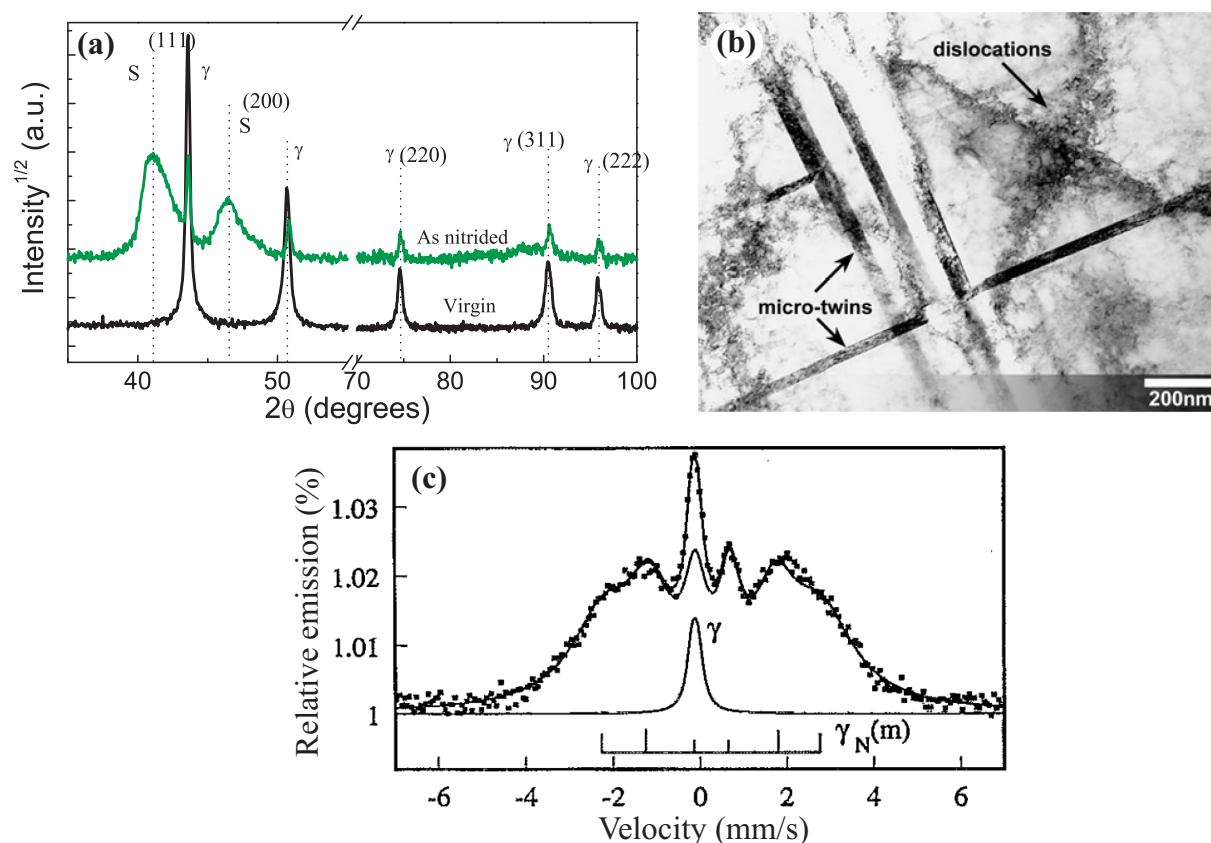


Figure 2.12: (a) XRD profiles before and after nitriding of AISI 316L ASS [96]. (b) TEM of low temperature plasma nitrided AISI 316L ASS showing high density of dislocations and micro-twins [97]. (c) Conversion electron Mössbauer spectroscopy data of ion beam nitrided AISI 304 ASS [89].

elements [89]. Usually, γ_N (magnetic), γ_N (paramagnetic), γ' -Fe₄N and ϵ -Fe₂N phases are identified in the S phase [41, 89, 91, 98]. Öztürk et al. [89] have shown that the S phase can be ferromagnetic or paramagnetic at high and low nitrogen content, respectively. Basso et al. [88] found that this transition occurs at N concentrations similar to Cr. It is suggested that the ferromagnetism due to N incorporation arises from two different mechanisms: the rearrangement of 3d electrons after changing the Fe–Cr–Ni atomic distances [89] and/or the formation of metallic nitrides [88]. However, Mössbauer spectroscopy cannot provide information about the local environment around Cr and Ni.

Electron microscopy is often used in addition to X-ray diffraction. Using transmission electron microscopy (TEM)(Fig. 2.12(b)) it was confirmed that the S phase has a high density of dislocations [13, 99], slip lines [13], deformation twins [13, 97], and stacking faults [99, 100]. Some authors also found nitrogen ordering in the S phase [100, 101], while others did not [99]. Menthe et al. [12] observed precipitates at a size of a few nanometers after nitriding at $\sim 450^\circ\text{C}$. In addition, areas with a lamellar structure were seen. Li

et al. [102] also observed the formation of very fine CrN precipitates forming lamellar structure during TEM *in-situ* heating. Xiaolei et al. [101] suggested, on the basis of electron diffraction patterns, that the S phase consists of γ' -Fe₄N with Cr-N clustering, without, however, precipitation of the compound CrN.

The alternative technique which is capable of probing the local environment of the elements is the X-ray absorption fine structure spectroscopy (EXAFS). However, EXAFS investigations of short range order of nitrogen in stainless steel are scarce [38, 40, 103–105]. The investigation by Oda et al. [103] addressed nitrogen containing 15Ni-15Cr austenitic stainless steel, i.e. with nitrogen contents being largely lower than for expanded austenite. The nitrogen atoms were found to form interstitial-substitutional complexes with chromium atoms.

Kizler et al. [104] investigated salt bath nitrided foils of stainless steel AISI 304 and AISI 316. Unfortunately, neither the nitriding temperature nor the duration of nitriding is stated in this work. However, salt bath nitriding is commonly carried out at temperatures above 763K, i.e. in the temperature range where precipitation of CrN occurs. The authors report a strong lattice distortion around the Cr and Mo atoms, whereas only small lattice distortions could be observed in the neighborhood of the Fe and Ni atoms. This observation was interpreted to indicate that dissolved nitrogen would prefer Cr and Mo as nearest neighbors, which would be consistent with the higher affinity of nitrogen to Cr and Mo as compared to Fe and Ni.

From the recent investigation by Munoz-Paez et al. [105] on nitrided Cr, Mo, Mn and V alloyed ferritic steels, an occurrence of “new non-crystalline domains involving nitrogen” was concluded. Cr, V and Mn were found to form austenitic *fcc* structures with the nitrogen atoms residing in the octahedral interstices upon nitriding. However, the study was performed on ferritic steels so that the findings do not necessarily apply to austenitic steels.

A recent EXAFS investigation by Oddershede et al. [38] on gas nitrided and denitrided AISI 316 austenitic stainless steel flakes showed the S phase being present in both the as-nitrided and denitrided samples, together with several other phases including CrN. The local structure of the Cr atoms was largely unaffected by denitriding in flowing hydrogen, whereas Fe atoms experienced a change in chemical surroundings. Furthermore, the local structure of the majority of Cr atoms was found to conform with the bond length of the chemical compound CrN, although only a fraction of the Cr atoms could be detected as CrN with XRD analysis. As a possible explanation for this observation, the authors suggest that part of the chromium nitrides diffracts coherently with the matrix and is present in the form of mixed substitutional–interstitial atom clusters or CrN platelets.

However, the nitriding conditions in this study were such that the partial decomposition of the nitrated material and development of CrN occurred. The authors repeated the study, from which they excluded the presence of CrN platelets or mixed substitutional–interstitial atom clusters, and suggested that the Cr atoms form a 3D network (cage structure) in the solid state [39, 40].

Summarizing this section, the results obtained by various techniques point to a rather complex microstructure of the S phase. The XRD results show that the S phase has an *fcc* structure with high density of elastic and plastic deformations. TEM and EXAFS suggest that Cr tends to form CrN clusters. However, the degree of Cr and N clustering at the typical nitriding temperatures ($\sim 400^\circ\text{C}$) is unclear, as is the shape and size of these clusters.

2.5.3 Nitrogen diffusion in ASS

As expected from a diffusion controlled growth, the dependence of the mean diffusion layer thickness $\langle X_N \rangle$ linearly increases with the square root of time, according to

$$\langle X_N \rangle \approx 2\sqrt{Dt}. \quad (2.26)$$

However, the shape of the nitrogen depth profiles is not consistent with the standard analytic solution of the diffusion equation that holds for concentration independent diffusion in a semi-infinite solid with the constant surface concentration (Fig. 2.14). Rather, the depth profiles exhibit plateau-type shapes slowly decreasing from the surface, followed by a sharp leading edge. This leading edge is not an artifact of the NRA measurements, as the NRA depth resolution at 2 μm depth is about 0.15 μm , while the leading edge extends over about 0.3 μm . Also, the experimental values do not fit with theoretical data for N diffusion in ASS at low N concentrations or in pure $\gamma\text{-Fe}$ [8]. Fig. 2.13 shows the dependence of the nitrogen diffusion coefficient on temperature, as reported by different authors [8, 50, 66, 106–109]. All data show Arrhenius behavior with, however, different parameters D_0 and E (see Eq. (2.6)). The diffusion parameters have been determined within the temperature range of 1283–1573 K in Ref. [106]. In other references the temperature range is similar to the plotted range. The lower set of lines are from the early studies with $D_0 = 0.06 \text{ cm}^{-2} \text{ s}^{-1}$, $E = 1.87 \text{ eV}$ [66], and $D_0 = 3.6 \text{ cm}^{-2} \text{ s}^{-1}$, $E = 2.16 \text{ eV}$ [106] for AISI 316 and a stainless steel with 19 wt% Cr and 11 wt% Ni, respectively. However, here the N concentration was low (some at%), and the N diffusion was strongly influenced by Cr. The upper set of lines is obtained at higher nitrogen concentrations and have been selected from the literature for roughly consistent ion fluxes of $\sim 0.5 \text{ mA cm}^{-2}$ and ion

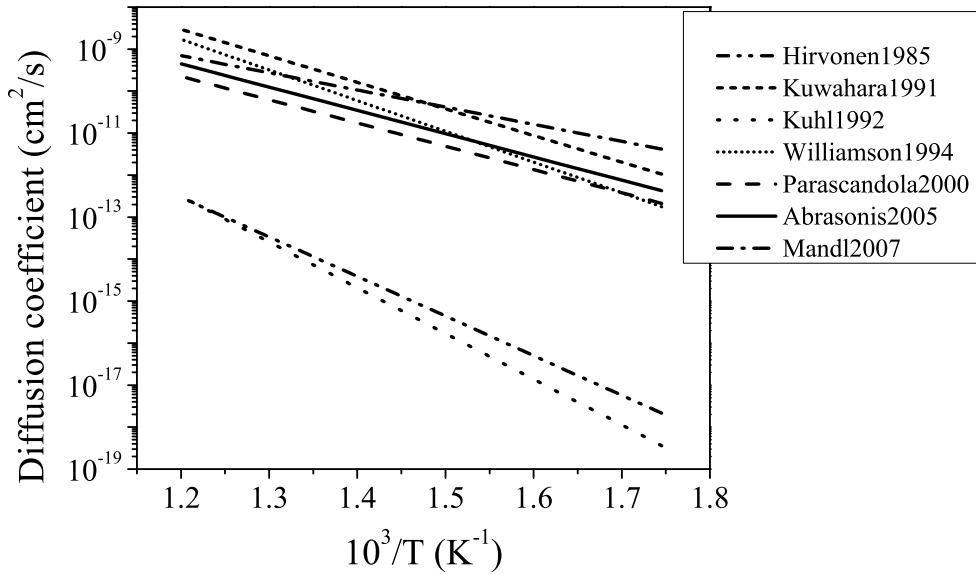


Figure 2.13: Comparison of nitrogen diffusion coefficients in ASS, based on literature data as provided in the text. The data of K uhl et al. is extrapolated from the temperature range of 1283–1573 K.

energies of ~ 1 keV [8, 50, 107–109]. It is evident that nitrogen diffusion in the S phase (at high nitrogen content) is significantly faster than in austenite at low nitrogen content. In this group the values of diffusion coefficient scatter by an order of magnitude. The diffusion activation energy ranges from 0.81 to 1.45 eV, while D_0 changes by five orders of magnitude from 1 to $5.5 \times 10^{-5} \text{ cm}^{-2} \text{ s}^{-1}$. Such discrepancy likely occurs because of the influence of material composition, texture, ion energy and flux on the nitrogen diffusivity. Different nitrogen diffusion models were used to extract the diffusion coefficients. Up to date, there is no systematic investigation of nitrogen diffusivity which would take into account all diffusion anomalies.

Presently, there is no convincing explanation of this phenomenon of enhanced diffusion, although some interesting suggestions are available in literature [3, 8, 83, 108, 110]. Saker et al. [83] introduced the modified nitrogen diffusion coefficient D_N :

$$D_N = (1 + A_{gr}(C_N)^2)D, \quad (2.27)$$

where C_N is the local nitrogen content, A_{gr} is a constant depending on the ASS grade. M andl and Rauschenbach [110] solved the Boltzmann-Matano equation [65] and obtained a concentration diffusion dependent coefficient $D(C_N)$, which significantly increases at increasing nitrogen content in the range 5–17 at%. A change in the electronic structure with the lattice expansion was proposed as a physical reason for this phenomenon. How-

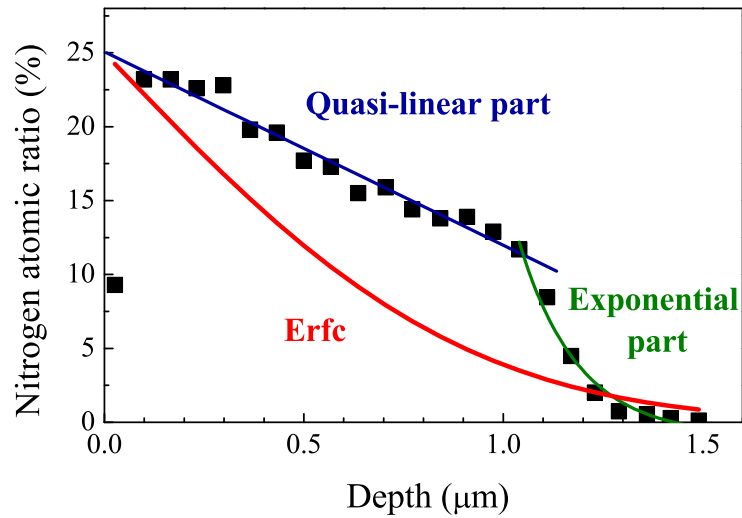


Figure 2.14: Typical nitrogen depth profile obtained by NRA compared to the analytic solution of the diffusion equation for concentration independent diffusion in a semi-infinite solid with a constant surface concentration (Eq. (2.5)).

ever, the $D(C_N)$ dependence reported in [110] is somewhat puzzling as very sharp peaks appear at certain nitrogen concentrations. This can probably be ascribed to the omission of trapping effects in the evaluation [33]. In the following, the concentration-dependent diffusion model will be referred to as “ $D(C_N)$ ” model.

A trapping-detrapping (TD) model was proposed by Williamson, Parascandola and Möller [3, 8, 108]. The TD model is based on the assumption that Cr atoms act as trap sites for the nitrogen and, once all traps are saturated, a faster diffusion of nitrogen is observed. The trapping energy is not very large, thus, nitrogen can be detrapped and diffuse further. The TD model was shown to reproduce the shape of the profile accurately [53]. The model was further confirmed in a refined experiment using ^{15}N and ^{14}N sequential implantation [108]. The intersection point between quasi-linear and exponential parts lies between $C_N = 13$ and 15 at% (Fig. 2.14). As pointed out by Abrasonis et al. [53] this value corresponds to the chromium content at this depth.

Christiansen et al. [33] reported experimental data confirming a concentration dependent diffusion, and combined $D(C_N)$ and trapping models to describe the observations. As indicated in Ref. [33], the $D(C_N)$ model alone leads to strong underestimation of the diffusion coefficient for low concentrations where the trapping has its most prominent influence. The resulting diffusion coefficient increases with the nitrogen content up to a maximum value of ~ 31 at%, and decreases again at higher nitrogen concentrations. The $D(C_N)$ model was suggested to be consistent with the expansion of the austenite lattice

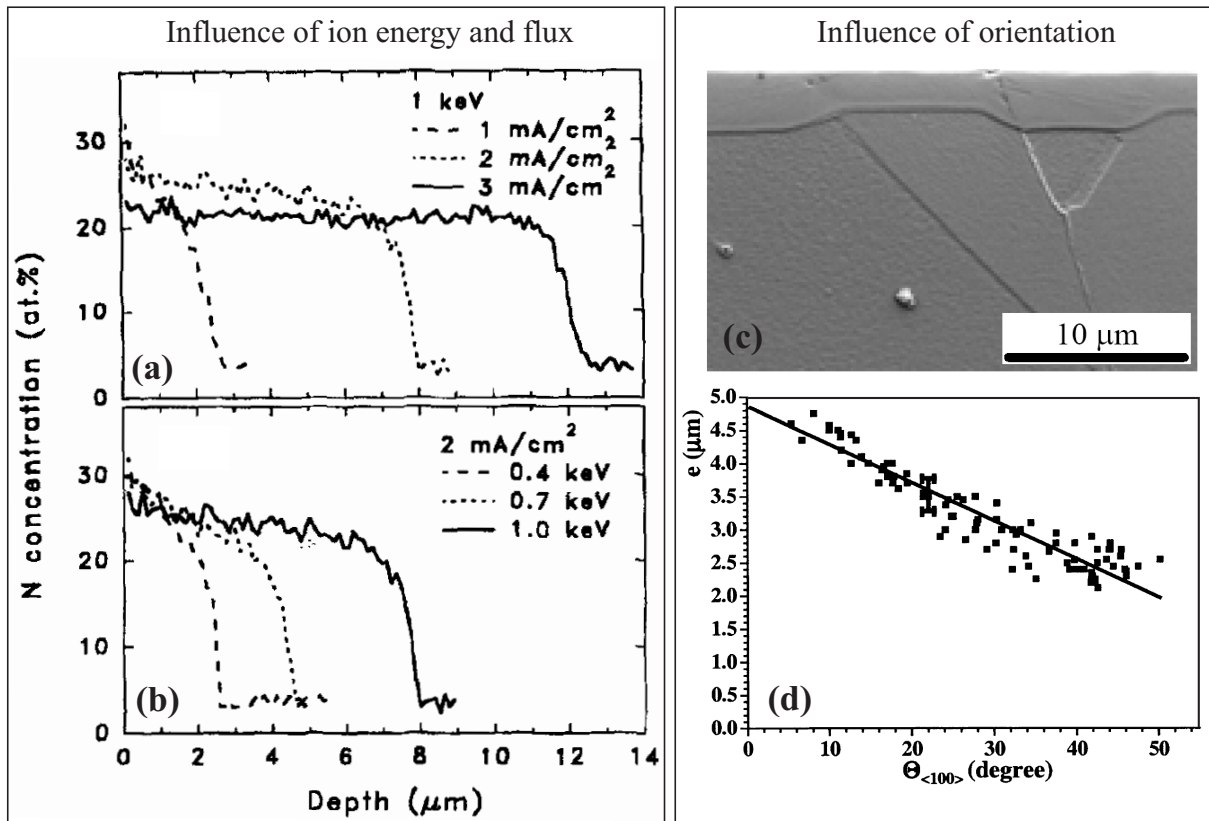


Figure 2.15: Auger electron spectroscopy depth profiles of N at either (a) fixed ion energy or (b) fixed ion flux. The processing temperature and time were fixed at 400°C and 60 min, respectively [3]. (c) Scanning electron microscopy cross-section picture of Inconel 690 plasma nitrided in a 95% N₂-5%H₂ gas mixture at 200 Pa for 4 h at 400°C showing different layer thickness for grains with different orientation [51]. (d) Nitrided layer thickness e in individual grains as a function of an angle between surface and {001} planes [51].

by dissolution of nitrogen, which is likely to facilitate the transfer of nitrogen atoms from octahedral to tetrahedral interstitial sites, the latter being considered as the activated state for the interstitial diffusion in *fcc* lattice. Accordingly, the activation energy for diffusion of nitrogen is reduced.

Irrespective of their ability to reproduce the shape or even to fit the nitrogen depth profiles, the above models cannot explain the dependence of the diffusivity on the ion energy [2,3,8,24,25,45–47], current density [3,25,48–50], and crystalline orientation [50–54]. Williamson et al. [3] reported for ion beam nitriding experiments a linear dependence of the thickness of the nitrided layer either on ion energy or current density (Fig. 2.15(a),(b)). The nitrogen transport rate within the depth of a few micrometers was shown to depend on the nitrogen supply rate at the surface. Moreover, the comparison between gas, glow

discharge, plasma-immersion ion implantation and ion beam nitriding procedures at 400°C demonstrates the later to be most efficient in terms of nitrified depth per unit of time [24]. This is consistent with the direct introduction of nitrogen below the surface during ion bombardment, so that the increased amount becomes available for the subsequent diffusion. Nonetheless, the formation of a thicker nitrified layer additionally requires the increased diffusivity. Abrasonis et al. [50] also reported increased nitrogen diffusivity at the increasing flux. It was also shown that the flux effect on the nitrogen diffusivity can be observed if pre-nitrified samples are bombarded with argon ions [111]. Based on this observation, a quasi-particle-enhanced mobility was proposed. On the contrary, the recent study by Manova et al. [112] shows that at 460°C the thickness of a nitrified layer is independent of ion energy or flux.

He et al. [51] used electron backscatter diffraction to establish a quantitative correlation between grain orientation of the substrate and the local thickness of the nitrified layer. The measurements were done on the cross-section of an Inconel 690 sample nitrified for 4 h. at 400°C (Fig. 2.15(c)). From this figure it is obvious that different layer thicknesses are observed for differently oriented grains. Grains with (001) orientation are associated with deeper diffusion layers as compared to (111) oriented grains (Fig. 2.15(d)). It is easier to observe this phenomenon on nickel based alloys [113], but it also occurs on AISI 316L [52,96]. An anisotropic stress-strain [51,114] development was proposed to explain the diffusion anisotropy; however, still the dependence of the diffusion on ion irradiation flux cannot be explained.

The role of ion energy is closely related to surface effects. The oxide layer commonly formed on the top of a metal prohibits nitrogen diffusion. Thus, ion energy has to be high enough that nitrogen could be implanted behind the oxide layer. Another way is to use such ion energies and fluxes that the sputtering is higher than the regeneration of the oxide layer [115]. However, the oxide layer can have a positive effect on the formation of the nitrified layer. Firstly, it also acts as a barrier layer against out-diffusion of the implanted nitrogen, and thus increases nitrogen retention. Secondly, nitrogen bombardment sputters not only the oxide layer, but also the substrate. So, the nitrogen, which was implanted, is sputtered with the substrate atoms. Thus, the effectiveness of nitriding decreases. It was shown theoretically by Dimitrov et al. [116] and experimentally by Parascandola [117] that the maximum of the nitrified layer is finite because of sputtering and is equal to $x_{\infty} = 2D/V_s$, where x_{∞} is the steady-state nitrified layer thickness, D is the diffusion coefficient and V_s is the sputtering rate.

Summarizing this section, nitrogen depth profile exhibits a non-conventional shape. Several models were proposed to explain this feature. It was shown that Cr atoms form

trap sites for N, and that N diffusion depends on the concentration. Despite the ability to reproduce or even fit the nitrogen depth profile, the models do not provide the information about the actual nitrogen diffusion mechanisms. The models are not able to explain the nitrogen diffusion dependence on the ion flux, energy and crystal orientation.

3 Experimental and Modeling Tools

3.1 Materials

Austenitic stainless steel of two grades, AISI 304L and AISI 316L, was investigated in this work. Polycrystalline and single crystalline AISI 316L samples with (001), (110) and (111) orientations were used. The single crystals were fabricated by float zone processing [118]. In order to ensure homogenization, the samples were vacuum annealed at 1100°C for 24 h and quenched in water. The composition of the material determined by Energy Dispersive X-ray analysis is shown in Table 3.1.

The samples were discs of 10 mm in diameter and ~ 1 mm in thickness. Before nitriding, they were polished under a water stream with SiC abrasive papers with an increasing paper grade from 500 to 1200, then using diamond spray with decreasing diamond grain sizes from 6 to 0.25 μm , and cleaned in an acetone and alcohol ultrasonic bath. Finally, the samples were polished using colloidal silica in water to remove the cold-working hardened layer.

Table 3.1: Composition of stainless steel grades AISI 304L and AISI 316L

Element	Symbol	AISI 304L (at%)	AISI 316L (at%)
Chromium	Cr	19.0	18.0
Nickel	Ni	13.0	13.0
Molybdenum	Mo	0.1	1.5
Manganese	Mn	1.5	1.8
Carbon	C	0.15	0.09
Nitrogen	N	0.3	0.3
Silicon	Si	0.7	0.7
Cobalt	Co	0.2	0.1
Copper	Cu	0.06	0.3
Iron	Fe	Balance	Balance

3.2 Nitriding techniques

Two nitriding techniques were employed in the present work: plasma assisted and ion beam nitriding. The plasma assisted nitriding (PAN) was used to obtain thick nitrided layers for X-ray absorption measurements. PAN employs low energy N ions, thus, there is almost no sputtering. The ion beam nitriding has the advantage of independent parameter control, i.e. the ion energy and the flux can be controlled separately. However, higher ion energies result in significant substrate sputtering. Thus, at these conditions nitrided layers of up to a few micrometers only can be obtained.

3.2.1 Plasma assisted nitriding

The thermally assisted plasma reactor URANOS at the University of Poitiers (France) [119,120] has been used for plasma nitriding (Fig. 3.1). The discharge in a silica tube 2 m in length and 0.2 m in diameter is generated through a matching network by a 13.56-MHz radio frequency excitation at a typical power of 700 W. This excitation is coupled to the tube by an outer electrode acting as a surfatron. Under this condition, a 2-m long plasma column is generated in the insulating tube. The electron temperatures and the ion density, measured by a Langmuir probe, are 3 eV and 10^{10} cm^{-3} , respectively. The plasma provides active nitrogen species, which can adsorb on the surface and diffuse further in the bulk. At these conditions, there is virtually no sputtering of the substrate material.

Treatments were performed under floating potential conditions. The samples were first heated in vacuum 20°C below the desired temperature. Then the chamber was fed with the gas mixture of 60 sccm $\text{N}_2 + 40 \text{ sccm H}_2$. The total pressure was 7.5 Pa. When the

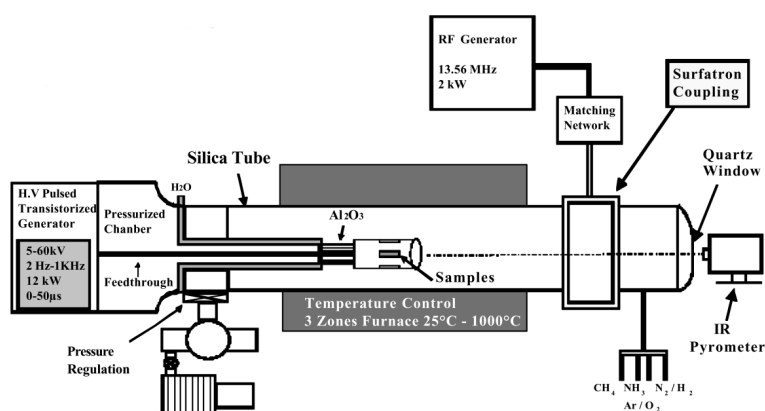


Figure 3.1: The set-up of thermally assisted plasma reactor URANOS [119].

plasma is switched on, the temperature rises up to the desired value within 15 minutes. It remains stable for the remaining treatment. The duration of nitriding was 30 hours.

3.2.2 Ion beam nitriding

3.2.2.1 Kaufman ion source

Ion beam nitriding was performed by using a Kaufman-type ion source with 3 cm beam diameter (Fig. 3.2). The hot filament broad ion beam source is equipped with two extraction grids. It can operate at inert and reactive gases. A tungsten alloy filament (filament voltage U_f) emits electrons which are accelerated towards the anode (discharge voltage U_d). The electrons ionize gas molecules and the homogeneous plasma is created inside the ion source. The inner body is on the positive potential which determines the energy of extracted ions (beam voltage U_b). The positively charged ions are extracted by planar two grid system produced from carbon. A negative voltage with respect to ground is applied to the accelerator grid (acceleration grid voltage U_a). The potential difference between the screen and the accelerator grids together with the geometrical dimensions define the ion optical parameters of the source. The ion source has been operated at $U_a = 100$ V, and $U_d = 40$ and 59 V using Ar and N gas, respectively. The beam voltage was varied from 0.5 to 1.2 keV. The ion source produces the ion beam with sharp energy distribution (< 2 eV). The work of Zeuner et al. [121] shows that at these parameters the Ar ion beam consists mainly of singly charged Ar ions. The N ion beam consists of $\sim 55\%$ N_2^+

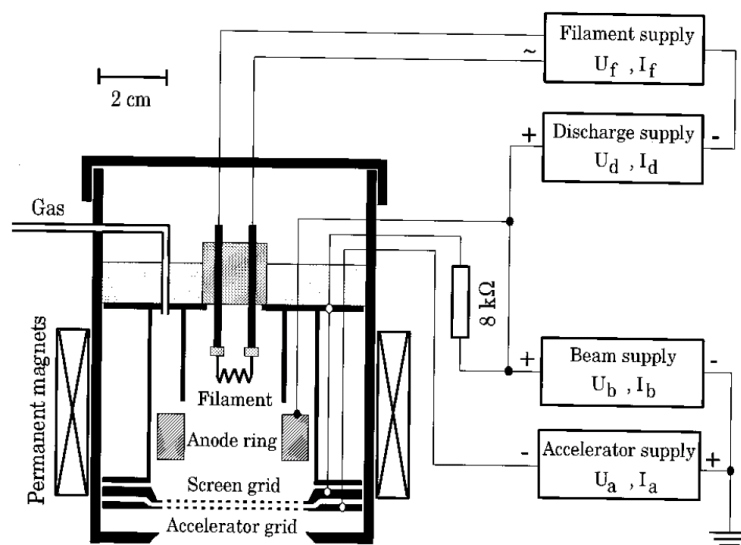


Figure 3.2: Schematic view of the Kaufman ion source [121].

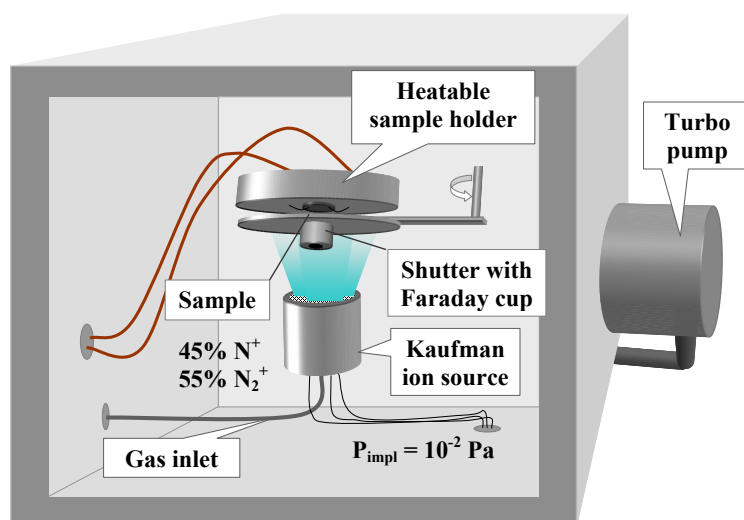


Figure 3.3: Sketch of the ion beam nitriding system.

and $\sim 45\%$ N^+ . Thus N^+ ions are implanted with the energy corresponding to U_b , while molecular ions N_2^+ break up arriving at the sample surface and give an effective particle's energy of $eU_b/2$, where e denotes the elementary charge constant.

3.2.2.2 Ion beam nitriding system

A schematic representation of the ion nitriding system is given in Figure 3.3. A high vacuum chamber houses the hot filament ion source. The broad ion beam produced by the ion source is directed towards the sample. A rotary motion feedthrough holds a shutter with a Faraday cup, later being used for the control of the ion current density. Secondary electrons are suppressed by the negative voltage of 30 V applied to the electrode surrounding the ion collector electrode. The ion current density was measured before each

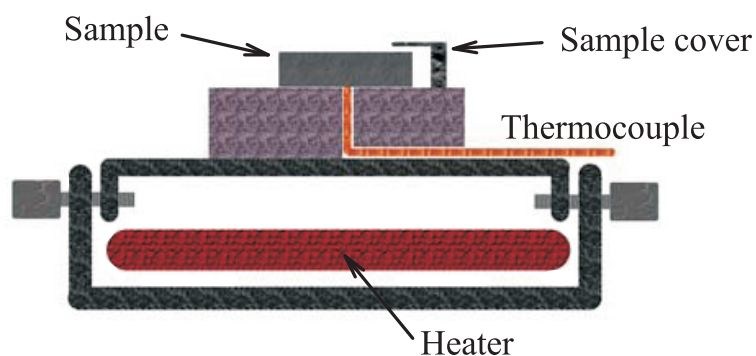


Figure 3.4: A sketch of the sample holder.

experiment. The vacuum chamber is pumped by a turbomolecular pump coupled with a rotary pump, resulting in a base pressure of $\sim 2 \times 10^{-4}$ Pa. A Pirani gauge head (operating from 100 Pa to 0.1 Pa) and a cold cathode gauge (operating from 0.1 Pa to 10^{-5} Pa) were used to measure the total pressure. The gas flux to the source is controlled by a mass flow controller. Gas fluxes of 3 and 2 sccm were used for Ar and N, respectively, resulting in working pressures of 1.3×10^{-2} and 6×10^{-3} Pa.

The sample holder is made of stainless steel mounted onto a boron nitride heater (Fig. 3.4), which permits heating of the samples up to 600°C . An isolated Ni/NiCr thermocouple is passed through the middle of the disk, on which the sample is fixed, and touches the backside of the sample. The actual temperature of the irradiated surface differs from the measured temperature by < 2 K under steady-state irradiation conditions [117]. In the following, the measured temperature will be used as the sample temperature.

3.2.2.3 Treatment conditions

Before nitriding, the samples were heated in vacuum to $\sim 350^\circ\text{C}$, and then sputter-cleaned for 20 min with the Ar^+ beam at the energy of 1 keV and the current density of 0.5 mA cm^{-2} . During this procedure, the heating power is adjusted to reach the desired steady state temperature under irradiation. The Ar^+ beam was then gradually changed to a pure N^+ ion beam during less than 1 min. During this step the temperature rose by a few $^\circ\text{C}$ and stabilized within a few minutes. During subsequent nitriding, the temperature varied

Table 3.2: Processing parameters of ion beam nitriding and the range over which they have been varied

Processing parameter	Range of variation
Ar ion beam	
Ion energy (keV)	1
Flux (mA cm^{-2})	0.5
Flux ($\text{cm}^{-2} \text{ s}^{-1}$)	3.1×10^{15}
Time (min)	20
Fluence (cm^{-2})	3.8×10^{18}
N ion beam	
Ion energy (keV)	0.5 – 1.2
Flux (mA cm^{-2})	0.3, 0.5, 0.7
Flux ($\text{cm}^{-2} \text{ s}^{-1}$)	2.9×10^{15} , 4.8×10^{15} , 6.8×10^{15}
Time (min)	100, 60, 43
Fluence (cm^{-2})	1.8×10^{19}
Temperature ($^\circ\text{C}$)	370 – 430

by less than 1°C. The nitriding was performed in the temperature range of 370 – 430°C in order to avoid the formation of chromium nitrides [122]. The energy of the N ion beam and the ion current density were varied in the range of 500 – 1200 eV and 0.3 – 0.7 mA cm⁻², respectively. The parameters are summarized in Table 3.2.

3.2.2.4 Annealing

To investigate the diffusion without ion bombardment, as-nitrided single crystals were subsequently annealed *ex-situ*. The samples were pre-heated during 18 min in vacuum with similar temperature evolution as described above and then kept at a constant temperature for 30 min. After the processing, the samples were left to cool in the chamber under vacuum. For the first 3 min the cooling rate was ~30°C/min, thus, any changes of the N depth profiles during the cooling stage can be neglected.

3.3 Analysis techniques

The phase structure has been determined by X-ray diffraction (XRD). Elemental depth profiles have been determined by elastic recoil detection analysis (ERDA), nuclear reaction analysis (NRA) and glow discharge optical emission spectroscopy (GDOES). The chemical state has been characterized by Mössbauer spectroscopy (MS), X-ray absorption near edge structure (XANES) and extended X-ray absorption fine structure (EXAFS). These techniques and the applied parameters are described below.

3.3.1 X-ray diffraction

Since the wavelength of X-rays (0.5-2.5 Å) is of the same order of magnitude as the inter-atomic distances in solids, X-rays are frequently used to study the crystalline structure of materials. When X-ray photons interact with electrons, some photons from the incident beam will be deflected away from their original direction and may interfere with each other (Figure 3.5). The condition for constructive interference is given by the Bragg law:

$$n\lambda = 2d_{hkl}\sin\theta. \quad (3.1)$$

As shown in Fig. 3.5, d_{hkl} is the distance between the lattice planes, λ the X-ray wavelength, θ the angle of the incident light with respect to equidistant hkl lattice-planes, and n the order of diffraction. By varying the angle θ , the Bragg's Law conditions are satisfied by different d-spacings. Plotting the angular positions and intensities of the resultant

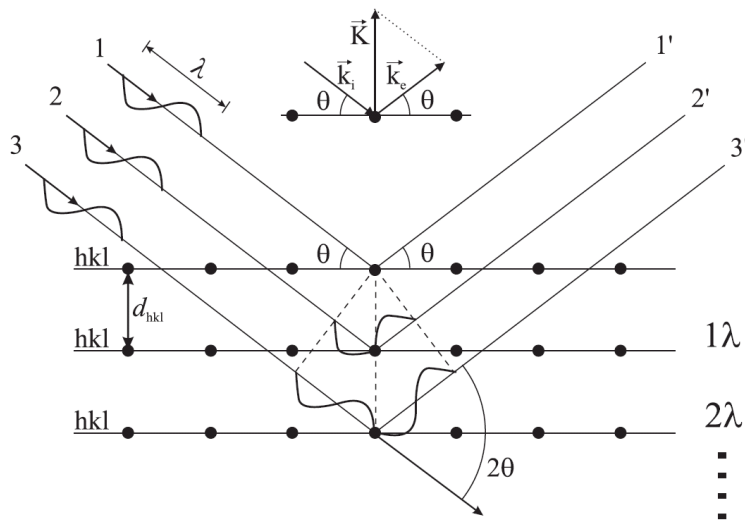


Figure 3.5: Reflection of X-rays from different atomic planes, illustrating Bragg's law. The scattering vector is defined in the inset.

diffracted peaks results in an XRD pattern, which is characteristic of the sample. Where a mixture of different crystalline phases is present, the resultant diffractogram is formed by addition of the individual patterns.

For X-ray diffraction, the Bruker D8 diffractometer with the $\text{CuK}\alpha$ ($\lambda = 0.15406 \text{ nm}$) radiation was used in the conventional $\theta/2\theta$ Bragg-Brentano and grazing incidence $\alpha/2\theta$ geometries (Fig. 3.6). In $\theta/2\theta$ geometry X-rays penetrate deep (the attenuation length is $\sim 5 \mu\text{m}$) into the sample and the signal comes from nitrated as well as from non-nitrated layers. In $\alpha/2\theta$ geometry the incidence angle is small ($\alpha = 1^\circ$) and the probed depth is $\sim 0.1 \mu\text{m}$, thus, only the nitrated layer can be analyzed. In grazing incidence geometry, planes making an angle up to 90° with the surface are probed while in the Bragg-Brentano geometry only planes parallel to the surface contribute to a Bragg reflection.

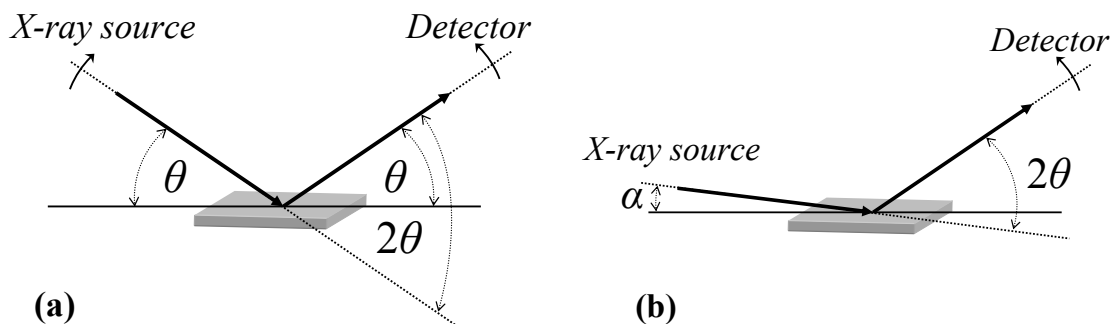


Figure 3.6: Schematic diagrams of $\theta/2\theta$ Bragg-Brentano (a) and grazing incidence $\alpha/2\theta$ geometries (b).

3.3.2 Depth profile measurements

3.3.2.1 Glow discharge optical spectroscopy

Optical emission spectroscopy from a special glow discharge lamp was used to determine nitrogen depth profiles for larger thicknesses (up to $30\ \mu\text{m}$). Fig. 3.7 shows the layout of the apparatus where the sample forms the cathode. First the lamp is evacuated by a rotary pump, then the argon valve is opened (1). The discharge is initiated by applying the voltage of typically 500–1000 V. Ar^+ -ions are created (2) which bombard the surface of the sample (3). The sputtered sample atoms diffuse into the plasma (4). Some sample atoms are excited (6) by collision with electrons (5). The emitted light is analyzed with an optical emission spectrometer (7). Using a computer system, qualitative depth profiles of intensity versus time are obtained. By measuring the depth of the sputtered crater afterwards, it is possible to convert the intensity evolution to quantitative profiles of concentration versus depth. GDOES profiles were calibrated according to NRA results.

3.3.2.2 Elastic Recoil Detection Analysis

Elastic recoil detection analysis was used to obtain elemental concentration depth profiles in the near surface layer (typically to a depth of several 100 nm). A 35 MeV Cl^{7+} ion beam was directed to the sample at an incidence angle of 5° with respect to the sample surface. Recoiling sample atoms are detected at the angle of 15° . The atoms recoiled from the surface exhibit larger energy than the atoms coming from larger depths, because the

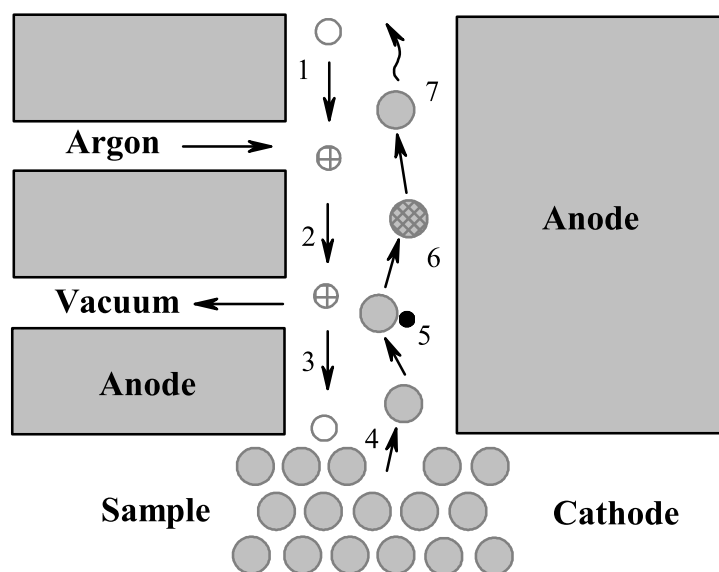


Figure 3.7: GDOES schematic view.

projectiles as well as the recoiled atoms lose energy on their way through the sample due to interaction with its electrons and atoms. For the known stopping powers dE/dx (energy loss dE of a projectile after passage of a material of thickness dx) of the projectile and recoil it is possible to calculate the depth x of the recoiling event from the measurement of the recoil energy. The obtained ERDA spectra were fitted using the IBA DataFurnace program [123]. Rather than the geometrical depth, ion-beam analysis naturally produces a depth scale in terms of an areal density. For conversion to the geometrical depth, the lattice parameter was taken as 3.8 Å. The lattice parameter variation depending on the nitrogen concentration was omitted, since the nitrogen concentration varies but little in the analyzed depth.

3.3.2.3 Nuclear Reaction Analysis

Nuclear reaction analysis is used to measure low- Z elements, such as carbon, nitrogen, oxygen, and boron. With NRA, the primary projectile induces a nuclear reaction with the low- Z nuclei in the target material and ejects particles with kinetic energies characteristic for a specific nuclear reaction.

In this work the $^{14}\text{N}(d, \alpha_1)^{12}\text{C}$ nuclear reaction is used to determine ^{14}N depth profiles. The reaction cross section was taken from Ref. [124] (Fig. 3.8(b)). The incident deuteron energy was 1.4 MeV. In the energy range 1.4-1.0 MeV the reaction cross section is roughly constant. This approximately corresponds to the analyzing depth of $\sim 3 \mu\text{m}$ in steel [125]. The deuterium beam was produced by a 3 MV Tandetron accelerator. The beam hits the sample surface perpendicularly. The α particles are collected by the ion implanted silicon detector of 100 μm nominal thickness operated at a reduced bias voltage of 40 V in order to suppress proton induced signals in the energy range of interest. The detector was placed at a scattering angle of 165° . The energy resolution of the detector is about 11 keV, which results in depth resolution of $\sim 0.1 \mu\text{m}$ near the surface and $\sim 0.15 \mu\text{m}$ at the depth of 2.5 μm . The deuterium current was $\approx 5 \text{ nA}$ in order to keep dead-time corrections below 5%. If the concentration calibration is done properly, the concentration error is mainly determined by counting statistics. The quasi-linear part of the nitrogen depth profiles can be fitted with a line. The fit error is approximately equal to the concentration error, which is $\sim 2 \text{ at}\%$. An example of the NRA spectrum is shown in Fig. 3.8(a). The spectrum is dominated by elastically backscattered deuterium from the main constituents of ASS, Fe, Ni and Cr, at energies below the incidence energy (1.4 MeV). Peaks at higher energies appear from protons and α particles resulting from nuclear reactions with N and C.

The obtained NRA spectra were fitted using the IBA DataFurnace program [123]. For conversion of the resulting areal density scale to the length scale, the lattice swelling

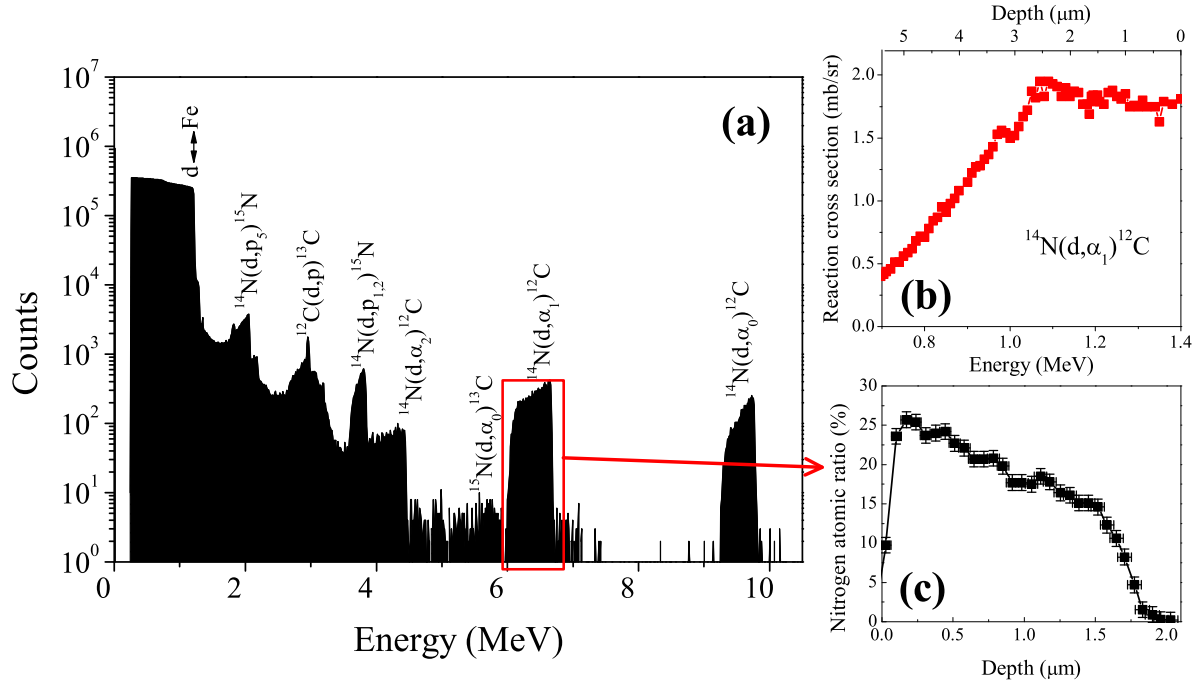


Figure 3.8: An example of a NRA spectrum obtained from a nitrided single crystal (a). $^{14}\text{N}(d, \alpha_1)^{12}\text{C}$ reaction cross-section [124] (b). Calculated nitrogen depth profile with experimental errors (c).

was taken into account which results from the N incorporation into the ASS matrix during nitriding. The resulting lattice constant can be approximated using Vegard's law according to

$$a_{lat} = a_{lat}^0 + \beta \cdot c, \quad (3.2)$$

where $a_{lat}^0 = 3.6 \text{ \AA}$ denotes the lattice constant of the untreated steel, β the expansion coefficient and c the atomic concentration of nitrogen. For an Fe-N *fcc* alloy $\beta = 7.8 \times 10^{-4} \text{ nm/at\%}$ [126], which was also found to be valid for AISI 304L steel [50]. In view of the similarity between AISI 304L and AISI 316L steels, the same value was employed. This dependence is also in a good agreement with XRD results and with recent results obtained from homogeneously expanded austenite synthesized by gas nitriding of AISI 316 [93]. A typical nitrogen depth profile is shown in Fig. 3.8(c).

3.3.2.4 Determination of sputtering rate

In order to determine the sputtering rate a part of the sample surface was hidden from the beam by a mask. The step height between the covered and uncovered areas was measured by a profilometer for each sample. The sputtered depth after Ar^+ bombardment for 20 min was assessed for each orientation separately. The sputtered depth with Ar^+ was later

subtracted from the depth measured after nitriding. The step height after nitriding is due to the interplay between sputtering and swelling. If the nitrided layer is 2 μm deep (typical depth in the sample with (001) orientation after 1h nitriding at 400°C), and the average lattice parameter is taken as 3.8 Å, i.e. expanded by 4 %, the surface moves due to swelling by ~ 100 nm. If the nitrided layer is 1 μm deep (a typical depth in the sample with (111) orientation after 1h nitriding at 400°C), the surface moves due to swelling by ~ 80 nm. Thus, there is a little difference compared to the sputtering depth (typically more than 500 nm). For simplicity, the measured step height was assumed to be only due to sputtering, thus, the swelling is included into the effective sputtering.

3.4 Chemical state and local coordination

3.4.1 Conversion Electron Mössbauer Spectroscopy

The Mössbauer effect makes use of resonant absorption of gamma rays by atoms of the same isotope. In our case, the source of gamma rays is radioactive ^{57}Co , which undergoes a nuclear decay to ^{57}Fe , which emits a γ -ray. With a static source, γ -ray can only be absorbed by ^{57}Fe in the sample, if the decaying Co atom is surrounded by the same atoms as the absorbing Fe. By oscillating the source mechanically, the energy of the γ -ray is modulated in very small increments due to Doppler effect. Where the modulated γ -ray energy matches precisely the energy of a nuclear transition in the absorber with the arbitrary chemical environment of ^{57}Fe , the γ -rays are resonantly absorbed. The basic elements of a Mössbauer spectrometer are a source, sample, detector, and a drive to move the source or the absorber. Most commonly, the velocity of the source towards and away from the sample is varied linearly with time. Fig. 3.9 shows the experimental setup for Conversion Electron Mössbauer Spectroscopy, which records the conversion electrons emitted by the resonantly excited nuclei in the absorber.

The Mössbauer spectrum is mainly affected by three mechanisms:

- Isomer shift (IS) resulting from the difference in the electron densities at nuclear sites in the emitting and absorbing atoms. This difference in density changes the Mössbauer transition energy, so that the entire spectrum is shifted. Therefore, the isomer shift allows to distinguish, e.g., different ionic charge states in the solid.
- Quadrupole splitting (QS). Nuclei in states with an angular momentum quantum number $I > 1/2$ exhibit a non-spherical charge distribution. This produces a nuclear quadrupole moment. The presence of an electric field gradient (produced by an

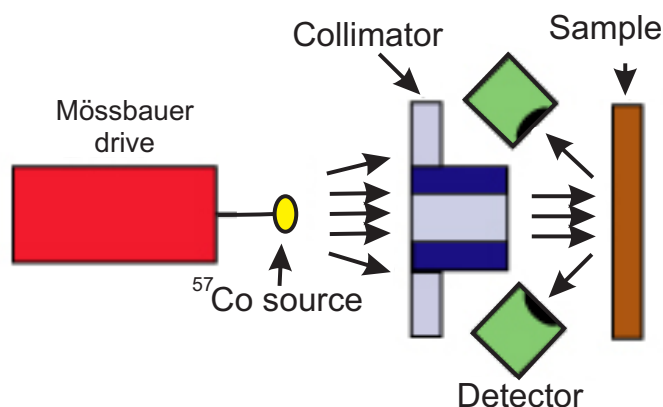


Figure 3.9: An experimental setup sketch for Conversion Electron Mössbauer Spectroscopy.

asymmetric electronic charge distribution or ligand arrangement) leads to a two-level hyperfine splitting.

- Magnetic splitting (MS). In the presence of an internal magnetic field the nuclear spin moment experiences a dipolar interaction with the magnetic field resulting in splitting of a given nuclear spin I into $(2I+1)$ substates.

CEMS was employed to investigate the local surroundings, charge states and magnetic properties of ^{57}Fe in the nitrated samples. The technique is sensitive to 2.2 % of the total Fe concentration, according to the abundance of ^{57}Fe in natural Fe. The CEMS spectra were measured at room temperature by placing the sample in the He-CH₄ gas

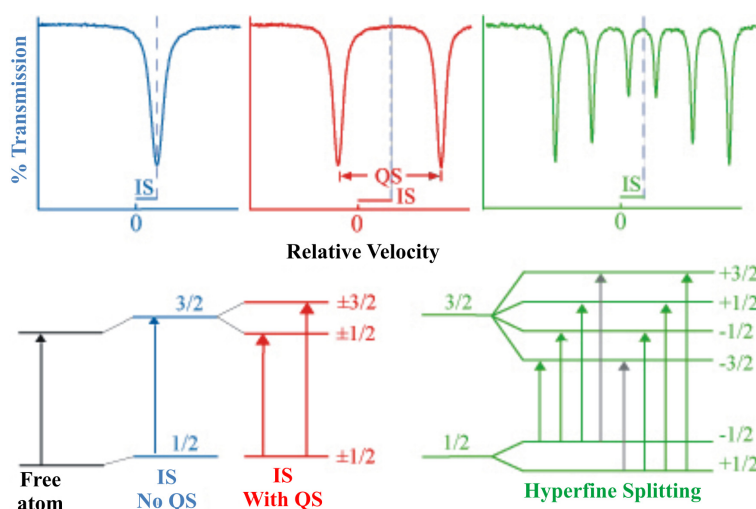


Figure 3.10: Isomer shift (IS), isomer shift with quadrupole splitting (QS) and magnetic splitting with isomer shift.

filled proportional counter. Below, all isomer shifts will be given with respect to an α -Fe foil, which is the commonly used reference.

3.4.2 X-ray absorption spectroscopy

X-ray photons may be absorbed in the matter through the photo-electric effect. In this process, an atom absorbs an X-ray of energy E and induces electronic transitions from core levels with energy E_0 into unoccupied states which provide exactly the right energy and angular momentum. The kinetic energy of the photoelectron is then $E - E_0$. Following absorption, the core state is eventually filled ejecting a fluorescent X-ray or an Auger electron. There are several experimental strategies that are readily available, which are the registration of the fluorescence yield, the electron yield, or the measurement of photoabsorption in transmission mode. The number of both fluorescent photons and Auger electrons is proportional to the number of core holes created by X-ray absorption. The relative yields of fluorescence decay versus Auger decay are strongly dependent on the atomic number of the absorber. For light atoms (e.g. C, N, O), Auger processes dominate. As the atomic number increases, the rate of fluorescence yield relative to Auger increases exponentially. For iron, nickel and chromium, fluorescence decay dominates. Thus, in the present work the fluorescence mode was used. Only a part of the fluorescence yield for

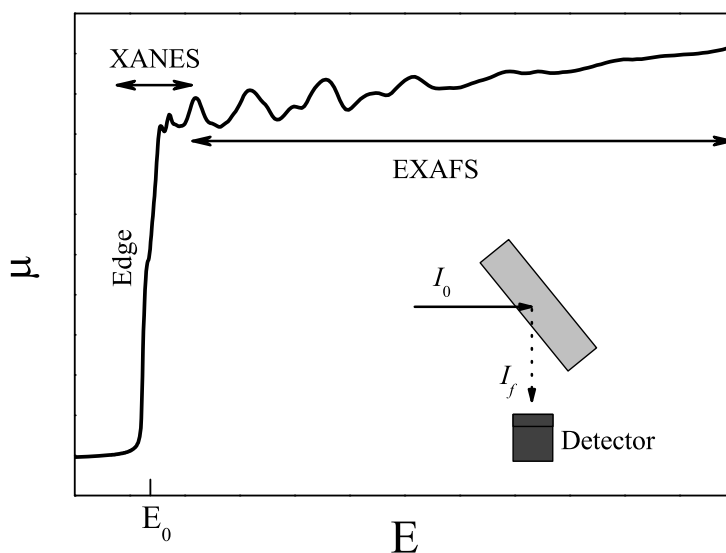


Figure 3.11: Schematic representation of the fluorescence experiment and the resulting X-ray absorption spectrum μ vs E for the K absorption edge of an iron atom in ASS which corresponds to the ejection of $1s$ electron by absorption of an X-ray photon with $E \geq E_0$, where E_0 is the binding energy.

each element was collected to avoid influence with the emission from other elements.

X-ray absorption is characterized by the absorption coefficient μ as a function of photon energy E . In a fluorescence experiment, $\mu(E)$ is determined as

$$\mu(E) \propto I_f/I_0, \quad (3.3)$$

where I_0 is the intensity of the incident beam and I_f is the intensity of a fluorescence line associated with the absorption process, which is proportional to the absorption rate. Fig. 3.11 shows the K absorption edge of an iron atom in ASS. The sharp rise in $\mu(E)$ due to the Fe $1s \rightarrow 4p$ transitions is followed by oscillations in $\mu(E)$. This X-ray absorption spectrum is typically divided into two regimes: X-ray absorption near-edge spectroscopy (XANES) and extended X-ray absorption fine-structure (EXAFS). XANES typically corresponds to the absorption within 50 eV from the main absorption edge, being strongly sensitive to oxidation state and local coordination symmetry of the absorbing atom. EXAFS is used to determine the distances, coordination number, and species of neighbor atoms. This will be described in greater details in the following.

3.4.2.1 XANES

The analysis of XANES oscillations in the spectrum of a particular sample can provide information about vacant orbitals, electronic configuration, and the site symmetry of the absorbing atom. In addition, the absolute position of the edge is related to the oxidation state of the absorbing atom, because the shielding of the core electrons depends on the occupation of the other electronic levels. At higher energies the modulations become weaker, and single scattering effects dominate. The emitted photo-electron wave interferes constructively and destructively with its back scattered intensity from the surrounding atoms. Hence, the observed fringes contain structural information, like inter-atom distances and coordination numbers. In addition, XANES probes the electronic structure, and hence, X-ray absorption spectroscopy is capable of probing both structural order and electronic properties.

Current theories of XANES in condensed systems employ one-electron and dipole approximations. In the XANES region electron transitions occur towards unoccupied states inside the excited atom, while in the EXAFS region the energy of the electron is high enough to ionize the atom. Therefore, the XANES region can be related to a partial density of states of the absorbing atom, since the absorption process must obey the transition rules. For instance, in the case of K-edge absorption the $1s$ electron can only be excited to a state with p -character, since $l = +1$ for photon absorption, when only the dipole

approximation is considered. Multipole excitations disturb this simple picture, however, they are often very weak in intensity. In addition, hybridized atomic bands might also facilitate initially forbidden transitions. Although these aspects can involve complicated transitions in the electronic structure, the greatest difficulties in XANES arise due to the multiple scattering events on the structure. Due to the complications brought by multiple scattering effects, the XANES theory is complex, and not yet fully understood. The analysis is therefore often done in comparison with similar materials for which successful ideas have been developed for interpreting the XANES features. Nevertheless, theoretical models have been refined in the last decade. A current state-of-the-art code is FEFF8 [127], which is able to simulate ab-initio XANES spectra including the self-consistent real-space multiple scattering theory. In many cases it allows a quantitative interpretation of XANES data.

3.4.2.2 EXAFS

EXAFS is characterized by an oscillatory structure found in the post-edge region of the X-ray absorption spectra. In this region, the photoelectrons carry higher energies and are only weakly scattered by neighboring atoms. The ejected photoelectron can be represented as an outgoing spherical wave originating from the absorbing atom (Fig. 3.12a). The outgoing spherical wave has a wavelength $\lambda = 2\pi/k$, where

$$k = \sqrt{\frac{2m}{\hbar^2}(E - E_0)}. \quad (3.4)$$

Here E_0 is the absorption edge energy and m is the electron mass. In the presence of the neighboring atoms (Fig. 3.12b) the outgoing photoelectron can be backscattered from the neighboring atoms, thereby producing an incoming wave which can interfere either constructively or destructively with the outgoing wave near the origin depending on the environment and electron energy resulting in the oscillatory behavior of the absorption rate. The amplitude and frequency of this sinusoidal modulation of μ vs E depend on the type of the neighboring atoms and their distances away from the absorber, respectively.

The modulation of the absorption rate in EXAFS is defined as

$$\chi(E) = \frac{\mu(E) - \mu_0(E)}{\Delta\mu_0(E)}, \quad (3.5)$$

where $\mu(E)$ is the measured absorption coefficient, $\mu_0(E)$ is the smooth background function representing the absorption of an isolated atom, and $\Delta\mu_0(E)$ is the measured jump in the absorption $\mu(E)$ at the threshold energy E_0 . In order to relate $\chi(E)$ to structural

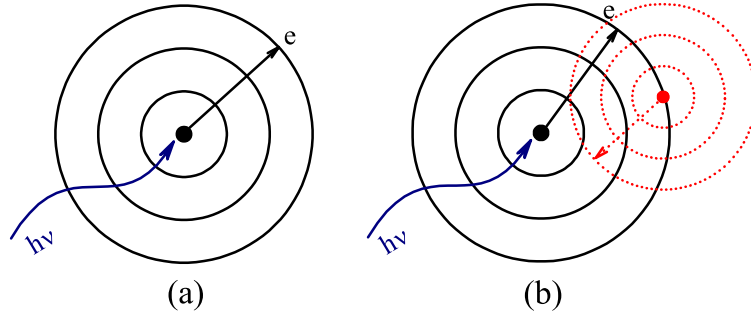


Figure 3.12: An atom absorbs X-ray photon and emits photoelectron which can be visualized as outgoing photoelectron wave (a). If there is an neighboring atom, the photoelectron wave may be backscattered producing an incoming wave, which interferes with the outgoing wave (b).

parameters, it is necessary to convert the energy E into the photoelectron wavevector k using Eq. 3.4. It is now well established that a single-electron single-scattering short-range theory is adequate for EXAFS interpretation. After the transformation, $\chi(k)$ can be described and modeled by EXAFS equation

$$\chi(k) = \sum_j N_j S_0^2(k) F_j(k) e^{-2\sigma_j^2 k^2} e^{-2r_j/\lambda_j(k)} \frac{\sin(2kr_j + \phi_{ij}(k))}{kr_j^2}. \quad (3.6)$$

Here $F_j(k)$ is the backscattering amplitude from each of the N_j neighboring atoms of the j th type at the distance r_j with the Debye-Waller factor of σ_j^2 , which accounts for thermal vibrations and static disorder. $\phi_{ij}(k)$ is the total phase shift experienced by the photoelectron. The term $e^{-2r_j/\lambda_j(k)}$ is due to inelastic scattering losses with $\lambda_j(k)$ being the electron mean free path. S_0^2 is the amplitude reduction factor due to many-body effects, such as shake up/off processes at the central atom (denoted by i). In this work backscattering amplitudes, total phase shifts and electron mean free paths are calculated using the FEFF8 code [127] and the coordination number, the Debye-Waller factor and the mean distance of neighbor atoms are fitted. Fig. 3.13 shows the backscattering amplitude function $F_j(k)$ for N, Fe, Cr and Ni. The backscattering properties of these metal atoms are very similar, thus it is not possible to separate their contribution to the spectra.

In order to obtain the radial distribution function a Fourier transform (FT) of the experimental EXAFS function $\chi(k) \cdot k^n \cdot W(k)$ is made. Here $W(k)$ is a ‘window’ function utilized to isolate a special range in the EXAFS spectrum. The analysis is performed by fitting the FT of the experimental EXAFS function $\tilde{\chi}(R)$ with a theoretical model based on the ab-initio code FEFF8. Note that $\tilde{\chi}(R)$ is a radial distribution function of R . R is a distance affected by a phase shift that rises from the FT of Eq. (3.6).

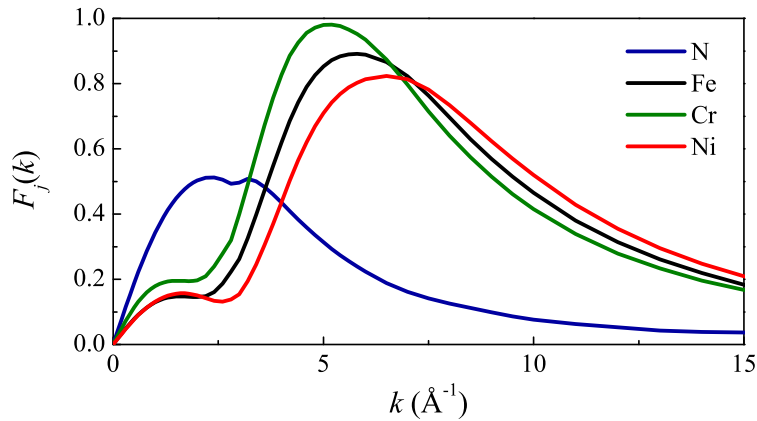


Figure 3.13: Backscattering amplitude function $F_j(k)$ for N, Fe, Cr and Ni.

The amount of information that can be obtained from fitting the FT of the experimental EXAFS depends on the Fourier Transform range (ΔR) and on the fitting space range in the k -space (Δk) [128]. Both these quantities are determined by the window function used in the fit. The total number of independent data points n_I that can be fitted simultaneously is given by $n_I = (2/\pi)\Delta k \cdot \Delta R + 2$ [128] and this is the maximum numbers of parameters that can be determined by a fit to the spectrum. The quality of the fit is calculated by using the reduced χ^2 function [128] (do not mix up with $\chi(k)$):

$$\chi^2 = \frac{n_I}{2N\sigma_N^2(n_I - P)} \sum_{i=1}^N |\chi^c(R_i) - \chi^e(R_i)|^2, \quad (3.7)$$

where the complex form of $\chi(R_i)$ is used and the sum is over the N point in the range of ΔR ; $\chi^c(R)$ and $\chi^e(R)$ are the calculated and experimental EXAFS spectra transformed in R -space (both real and imaginary parts). The number of parameters used in the fit is P . The quality of the fit can be judged by χ^2 . If a correct model is used and if noise is dominated by random fluctuation, then $\chi^2 \approx 1$. There are some cases in which random noise can be very small and a systematic error can dominate. So, a new parameter \mathfrak{R} , called quality factor is introduced to evaluate the quality of the fit between the data provided by a theoretical model and experimental data:

$$\mathfrak{R} = \frac{\sum_i |\chi^c(R_i) - \chi^e(R_i)|^2}{\sum_i (\chi^e(R_i))^2}. \quad (3.8)$$

\mathfrak{R} is a real number. It has to be as small as possible, in general $\mathfrak{R} = 0.01$ signifies that theory and data differ only by 1% [128].

Some theoretical limitations prevent EXAFS spectroscopy to determine elements that

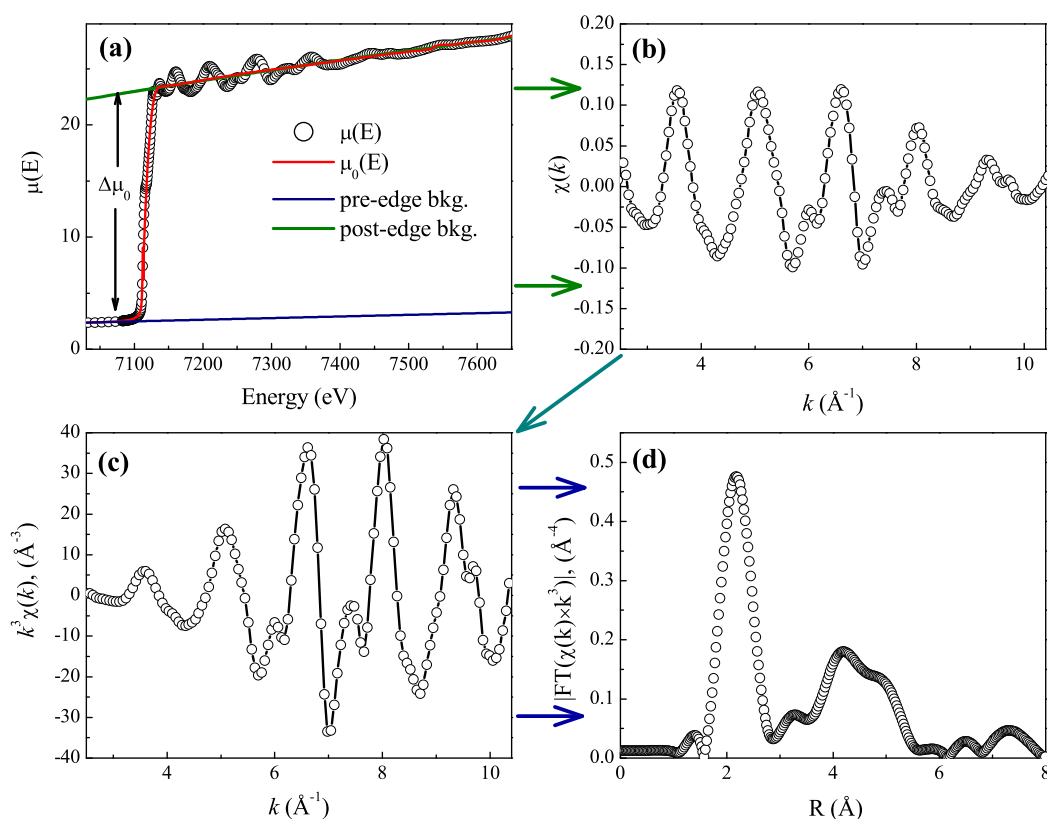


Figure 3.14: Iron X-ray absorption spectrum in ASS (a). Pre-edge and post-edge background functions are subtracted from the spectra to normalize to one absorption event. EXAFS oscillations (b) are isolated by subtracting a spline $\mu_0(E)$, which approximates atomic EXAFS. To compensate weak oscillations at high k range, EXAFS is multiplied by k^3 (c). After Fourier transform a pseudo radial distribution function is obtained (d).

belong to the environment, with a difference of atomic number smaller than two (e.g. Cr and Ni from Fe), since these elements have similar number of electrons and behave as equivalent backscatters. In this case it is not possible to separate them identifying individual contribution to the EXAFS signal.

3.4.2.3 Experimental and data processing

EXAFS and XANES data were collected in a fluorescence mode at the European Synchrotron Radiation Facility the Rossendorf Beamline (BM20) equipped with a double-crystal Si(111) monochromator with two collimating/focusing mirrors (Si and Pt-coating) for elimination of higher harmonics. The samples were mounted on tape. The acquisition time was 80 min per scan. For each sample 3–5 scans were averaged after energy calibrations performed by using Cr, Ni and Fe references.

The background subtraction and self-absorption correction was performed with the Athena program (Ver. 0.8.059) [129]. At this point the XANES spectrum is obtained. XANES was evaluated only qualitatively fitting reference spectra. For EXAFS a detailed quantitative analysis was performed. The absorption edge energy E_0 was determined by the second derivative $d^2\mu(E)/dE^2 = 0$ of the first main peak of the absorption spectra. Smooth pre-edge and post-edge background functions were subtracted to normalize the absorption spectra (Fig. 3.14(a)). To isolate EXAFS oscillations, a spline fitting, which approximates atomic EXAFS, was performed in the k range of $0.7 - 10.5 \text{ \AA}^{-1}$ with the parameter $R_{bkg} = 1$ (below this value the background algorithm removes Fourier components). The EXAFS spectra were corrected for self-absorption by using Tröger algorithm [130] assuming the samples being composed of 69% of Fe, 18% of Cr and 13% of Ni. At this point the EXAFS function $\chi(k)$, giving the modulation in the absorbance of the central atom as a function of the photoelectron wavenumber k , was obtained (Fig. 3.14(b)). k^3 weighting was used in order to avoid information loss at high k -values (Fig. 3.14(c)). The Fourier Transforms of $\chi(k)k^3$ was performed in the k -range of $2.5 - 10.4 \text{ \AA}^{-1}$ in order to obtain pseudo-radial distribution function (Fig. 3.14(d)). The pseudo radial distribution function gives the relative probability of finding the neighboring atoms with the given distance from the absorber. The refinement of the EXAFS data was performed in the WinXAS program (Ver. 3.11) [131].

3.4.2.4 Fitting procedure

Austenitic stainless steel has an *fcc* lattice. When nitrogen is introduced into ASS, it is assumed to occupy an octahedral interstitial position. As a result, the lattice expands. CrN and Fe₄N also have *fcc* lattice with nitrogen in octahedral positions. For Fe₄N ^{1/4} of octahedral positions are occupied [132].

Let M denote the absorber atom (Cr, Ni or Fe). The paths corresponding to the first M–N shell (if present) and the first four M–M distances were considered during the modeling. If a 3-atom multiple scattering path of the same r_j as the M–M path with a higher $F_j(k)$ value was found, this path was added on behalf of the M–M path. The scattering paths and their theoretical coordination numbers included in fits are shown in Fig. 3.15 and Table 3.3. It was assumed that the steel matrix has a *fcc* structure with the 3.6 \AA lattice parameter, and that each element is surrounded by Fe. As previously noted it is not possible to distinguish between Ni, Fe, and Cr, as they have very similar electron backscattering properties. For the sample nitrated at 400°C the nitrogen shell was introduced in octahedral positions, and the lattice parameter was assumed to be 3.8 \AA . For Cr, the nearest-neighbor environment composed of Cr, and of Fe starting from

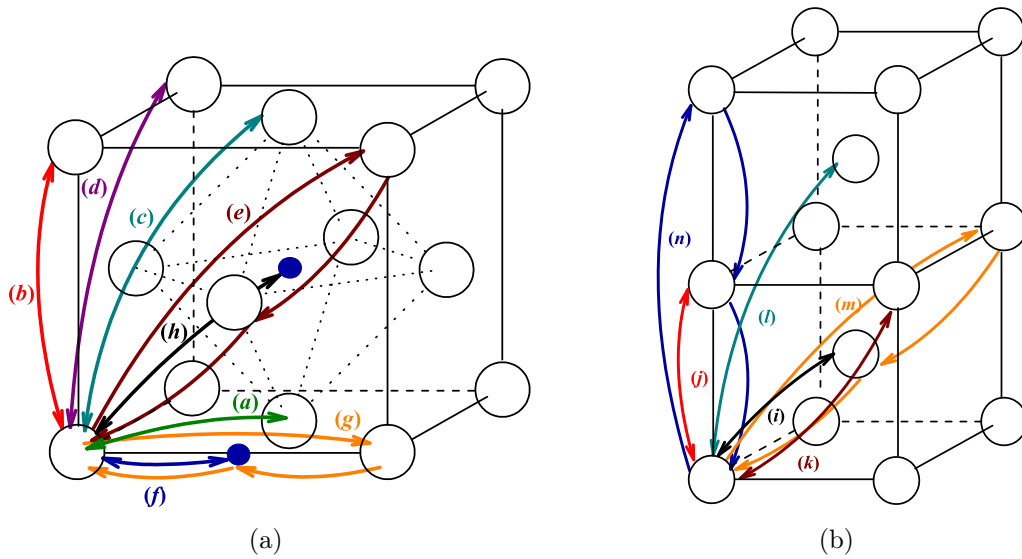


Figure 3.15: Scattering paths which were included in the EXAFS refinement for *fcc* (a) and *bcc* (b) lattices.

the distance of 5.08 Å was chosen, because this yields the lowest \mathfrak{R} quality factor. A *bcc* structure for Ni and Fe was used in the EXAFS refinement of the sample nitrated at 550°C. A two-phase model using the *fcc* and *bcc* structures in the 3:8 ratio was also tested for Ni and Fe EXAFS data. The obtained fits were substantially better than the single-phase fits, however, the addition of 4 shells introduced 12 additional parameters exceeding in total the free variable limit, thus resulting in an unreliable fit. Even after correlation of coordination numbers to the phase ratio a strong correlation between parameters was observed. Thus a single-*bcc*-phase model was used for Fe and Ni EXAFS refinement for 550°C nitriding. For Cr in the sample nitrated at 550°C the same model was used as for 400°C nitriding, only substituting Fe with Cr. For multiple scattering paths σ_j^2 was calculated as an average from single scattering paths. For all elements in the non-nitrated steel σ_j^2 were correlated for the first and second shells. The S_0^2 factor was calculated from the non-nitrated sample for each element assuming the coordination number $N_j = 12$ of the first M–M shell and was used for nitrated samples.

Table 3.3: Theoretical coordination numbers for the scattering paths used for the refinement.

<i>fcc</i>	(a)	(b)	(c)	(d)	(e)	(f)	(g)	(h)
	12	6	24	12	24	6	12	8
<i>bcc</i>	(i)	(j)	(k)	(l)	(m)	(n)		
	8	6	12	24	16	6		

3.5 Modeling of the nitrogen depth profiles

3.5.1 Trapping-detrapping model

In order to get deeper insights into the diffusion processes taking place during nitriding, the observed nitrogen depth profiles were fitted using the so-called trapping-detrapping (TD) model.

This model proposed by Parascandola et al. [108] takes into account nitrogen diffusion and trapping-detrapping. This has been shown to reproduce the main features of the N profiles and partial profiles of subsequently implanted ^{15}N and ^{14}N isotopes [108]. The model was further adapted for ion beam nitriding conditions in Ref. [50]. The model takes into account four processes: implantation, diffusion, sputtering and trapping-detrapping. Nitrogen can be in two states - trapped and freely diffusing, denoted here as $N_t(x, t)$ and $N_d(x, t)$, respectively. The nitrogen atoms are implanted into the surface with the flux j and the range distribution $f_R(x)$. Due to sputtering, the surface is receding with the velocity V_s .

The model assumes that only one type of trap exists, namely Cr atoms in the ASS matrix. The concentration of traps is assumed to be constant in time and depth. Each trap site is allowed to bind only one atom. It is further assumed that the detrapping energy is independent of the fraction of occupied traps, that local equilibrium exists between nitrogen on “free” sites and nitrogen on trap sites, and that trapping and detrapping are diffusion-controlled and follow first-order kinetics [108, 117]. The corresponding set of combined equations is

$$\begin{cases} \frac{\partial N_d(x, t)}{\partial t} = D \frac{\partial^2 N_d(x, t)}{\partial x^2} + j f_R(x) - V_s \frac{\partial N_d(x, t)}{\partial x} - S(x, t), \\ \frac{\partial N_t(x, t)}{\partial t} = S(x, t) - V_s \frac{\partial N_t(x, t)}{\partial x}. \end{cases} \quad (3.9)$$

Assuming only inward diffusion, the boundary conditions can be written as

$$\begin{cases} \frac{\partial N_d(0, t)}{\partial t} = \frac{D}{\lambda} \frac{\partial N_d(0, t)}{\partial x} + j f_R(0) - j \kappa N_d(0, t) - V_s \frac{\partial N_d(0, t)}{\partial x} - S(0, t), \\ \frac{\partial N_t(0, t)}{\partial t} = S(0, t) - j \kappa_t N_t(0, t) - V_s \frac{\partial N_t(0, t)}{\partial x}, \end{cases} \quad (3.10)$$

with the nitrogen atom jump length λ , the sputtering terms for “free” and trapped nitrogen $j \kappa N_d(0, t)$ and $j \kappa_t N_t(0, t)$, respectively, with appropriate constants κ and κ_t , and $S(x, t)$

as the trapping-detrapping term written as

$$S(x, t) = 4\pi R_t D \left\{ N_d(x, t) [H_t - N_t(x, t)] - \xi N_0 N_t(x, t) e^{\frac{-E_b}{k_b T}} \right\} \quad (3.11)$$

with the characteristic capture radius R_t , the concentration of trap sites H_t , the coordination number (the number of sites available for a nitrogen atom in solution around the trap) ξ , the host atomic density N_0 , and the binding energy to a trap E_b .

3.5.2 Fitting parameters

For simplicity, the capture radius was taken equal to the lattice constant of 3.8 Å corresponding to the host atomic density of $N_0 = 7.29 \times 10^{22} \text{ cm}^{-3}$. With Cr atoms being considered as the only trapping sites for nitrogen atoms, the Cr concentration of 18 at% corresponds to a trap concentration of $H_t = 1.31 \times 10^{22} \text{ cm}^{-3}$.

The system of equations (3.9) and (3.10) was solved numerically by using a finite difference scheme. The code uses a 3 nm mesh grid. Thus, it was assumed that all nitrogen is implanted into the first 3 nm thick layer as SRIM2010 simulations result in a mean nitrogen penetration depth of ~ 2.5 nm for 1 keV nitrogen ions. The value of the parameter λ was taken to be equal to the mesh grid value. Lowering λ or the mesh grid spacing does not change the results significantly.

The trap binding energy E_b depends on the value taken for the coordination number ξ . Calculations show that the value of the trap binding energy mostly influences the steepness of the leading edge while the kink between the quasilinear and exponential regions of the profile stays at the same position. For simplicity, ξ was taken equal to 1. The best fit was obtained with the trap binding energy E_b equal to 0.32 eV, which is very close to the value of 0.35 eV reported by Parascandola et al. [108]. The same E_b and ξ values were used for all fittings.

The nitrogen loss by sputtering is twofold: (1) sputtering of the matrix atoms is associated with the removal of incorporated nitrogen atoms and (2) sputtering of nitrogen out of near-surface interstitial positions. The sputtering rate for (1) was measured experimentally as described above. Concerning the process (2), the coefficients κ and κ_t depend on the ion energy distribution and the nitrogen sputtering yield. In general, the coefficient κ should be smaller than κ_t , as nitrogen in “free” state is less bonded to matrix atoms than trapped nitrogen. However, the binding energy is quite low and for the sake of simplicity it is assumed that $\kappa = \kappa_t$. The value of κ can be approximately calculated

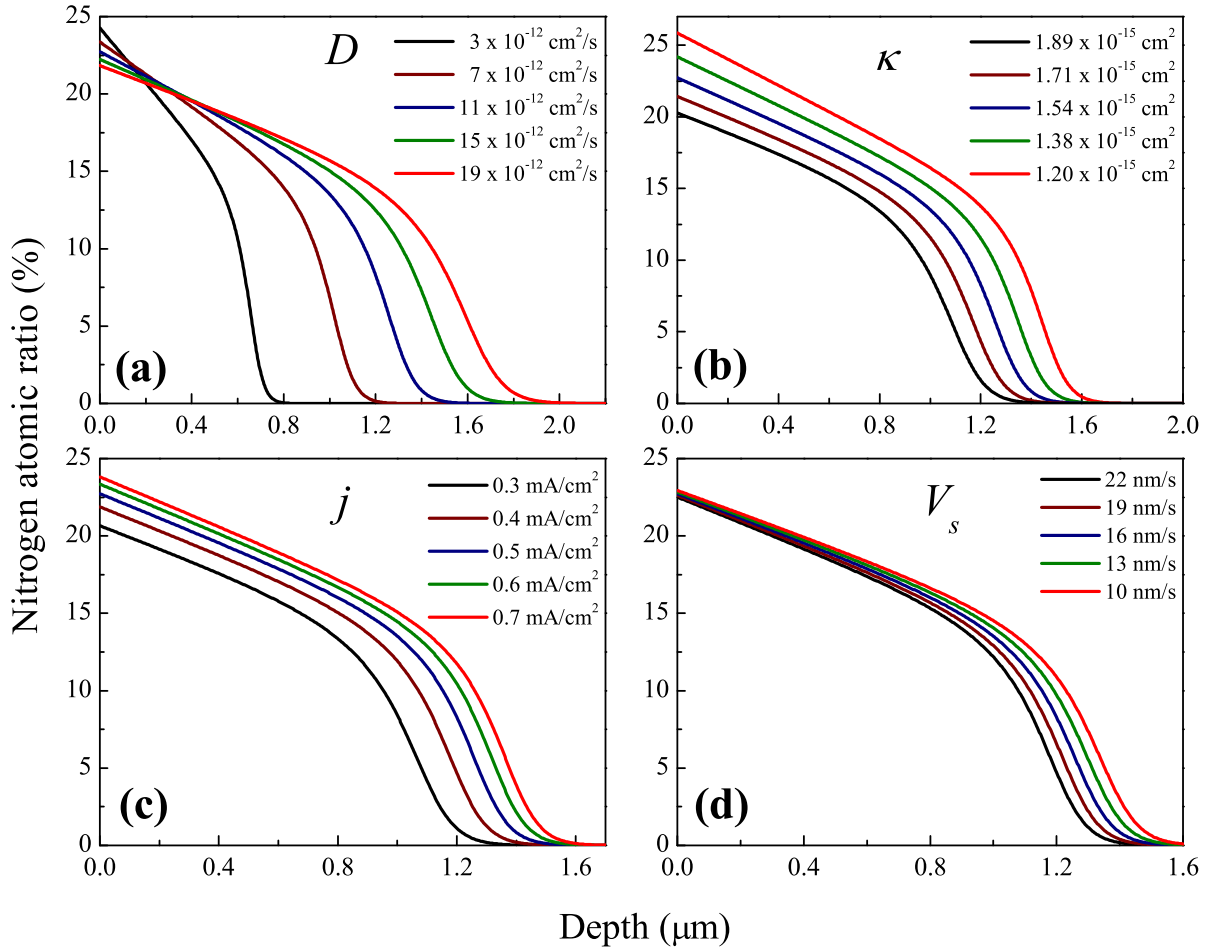


Figure 3.16: (a) Influence of the diffusion coefficient D , (b) nitrogen sputtering parameter κ , (c) nitrogen flux j and (d) surface recession rate V_s on the nitrogen depth profiles. One parameter, as indicated in the graphs, was varied. The constant parameters for the different graphs were $D = 11 \times 10^{-12} \text{ cm}^2/\text{s}$, $j = 0.5 \text{ mA}/\text{cm}^2$, $V = 16 \text{ nm}/\text{s}$, $\kappa = 1.54 \times 10^{-15} \text{ cm}^2$, and $t = 30 \text{ min}$.

from the experimental results by means of the following expression

$$\kappa = \frac{\Phi \cdot (1 - b) - \Phi_{ret} - \Phi_{sputt}}{\Phi \cdot C_N}, \quad (3.12)$$

where b is the backscattering coefficient, Φ is the ion fluence, Φ_{ret} and Φ_{sputt} are the amounts of nitrogen which are retained and sputtered according to the mechanism (1), respectively, and C_N is the nitrogen surface concentration. Eq. (3.12) is valid if C_N is constant. Calculations [50] and experiments [117] show that the surface concentration reaches a steady-state relatively fast (after ~ 5 min), thus validating the assumption of the constant surface concentration. The real surface concentration is lower than that

extrapolated from the linear part of the profile. However, the difference is expected to be small as the sputtering is partly balanced by the implantation. Such evolution of the surface concentration was also calculated by Parascandola with the TRIDYN code. The value of the backscattering coefficient was calculated using the SRIM2010 code to be $\sim 17\%$. The sputtered N amount Φ_{sputt} can be approximately calculated by multiplying the sputtered depth and C_N . The values of the coefficient κ for all orientations are shown in Table 5.1 (see below). This coefficient influences the surface concentration considerably.

It follows from the description above that the only free parameter is D , all the rest of them being defined either by the experiment or from literature data.

Fig. 3.16 shows how the diffusion coefficient, the parameter κ , the ion flux and the sputtering rate influence nitrogen depth profiles calculated according to Eqs. (3.9)-(3.11). Increasing the diffusion coefficient increases the nitrogen penetration depth as expected from Eq. (2.26). The surface concentration decreases slightly as implanted nitrogen is redistributed in the depth. The surface concentration and the penetration depth are lowered with the increasing κ . Higher sputtering rates shift the nitrogen profile towards the surface. The nitrogen surface concentration and the penetration depth increases concomitantly with flux. This is a natural flux dependence due to the scaling of the diffused amount with \sqrt{t} versus the scaling of the implanted amount with t . Also, the same surface recession rate was used in the calculations, i.e. it was not scaled to the fluence, thus, the flux effect is more pronounced.

3.5.3 Evaluation of the fit

The depth distributions originating from NRA are fitted by depth profiles obtained from the model described above. In a reasonable approximation, systematic errors and their dependence on the depth can be neglected. The experimental error of the individual data points is mainly given by the counting statistics.

The experimental depth distribution is given by N data points y_i . If the spacing of the depth scale is constant, the individual data from the depth distribution are related to the respective experimental counts per channel, n_i , by

$$y_i = K_i n_i \quad (3.13)$$

The conversion factor K_i contains kinematics, stopping powers and the scattering or reaction cross section, and thus depends on the depth. As the counts per channel obey

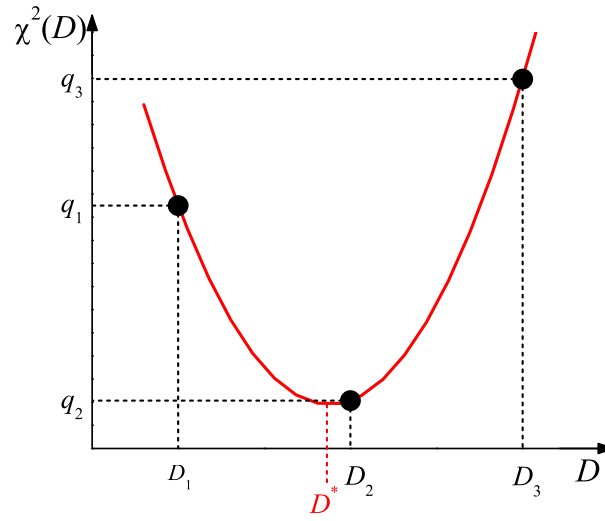


Figure 3.17: The fit is evaluated at three parameter D values by calculating the χ^2 function of square deviations. D^* is the best value of the fit parameter.

Poisson statistics, the statistical error of y_i becomes

$$\sigma_i = K_i \sqrt{n_i} \quad (3.14)$$

from which

$$\sigma_i = \frac{y_i}{\sqrt{n_i}}. \quad (3.15)$$

To the resulting set of N data points $(x_i, y_i \pm \sigma_i)$, a model curve $f(x, D)$ is fitted where the diffusion coefficient is the only parameter as described above. The best fit is obtained via the χ^2 method. D is varied in equidistant steps ΔD , until the χ^2 function of square deviations

$$\chi^2(D) = \sum_{i=1}^N \left(\frac{y_i - f(x_i, D)}{\sigma_i} \right)^2 \quad (3.16)$$

goes through a minimum involving three evaluations at the parameters $D_{1\dots 3}$ resulting in three values $q_{1\dots 3} = \chi^2(D_{1\dots 3})$ (see Fig. 3.17). The best value D^* of the fit parameter is then the minimum position of the parabola through the three points. The value with respect to p_3 is then given by

$$D^* = D_3 - \Delta D \left(\frac{1}{2} + \frac{1}{1 + \frac{q_1 - q_2}{q_3 - q_2}} \right) \quad (3.17)$$

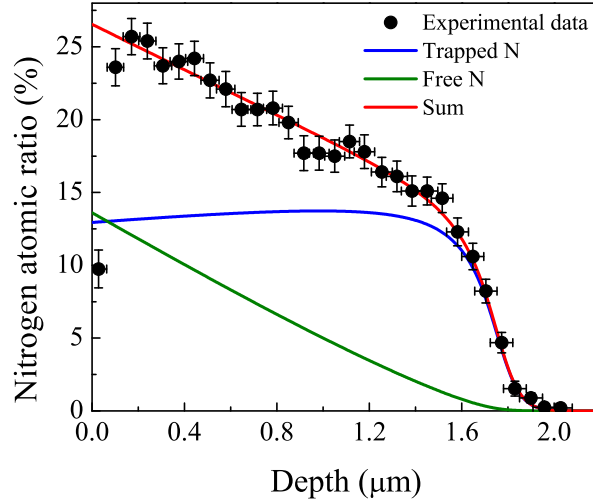


Figure 3.18: Comparison of the fit (red line) and the experimental (circles) N depth profile in a single crystal with the orientation (001). The 'free' and 'trapped' constituents of the calculated total N depth profile are shown as green and blue curves, respectively.

and the mean square error of the fit parameter can be approximated by

$$\sigma_D = \Delta D \sqrt{\frac{2}{n_{fr}(q_1 - 2q_2 + q_3)}} \quad (3.18)$$

where n_{fr} is the degree of freedom, which is in the case of only one parameter

$$n_{fr} = N - 1. \quad (3.19)$$

Fig. 3.18 shows a typical nitrogen depth profile together with experimental errors. The total nitrogen concentration is fitted according to the trapping-detrapping model. The model accurately reproduces the shape of nitrogen distribution. The nitrogen concentration decrease near the surface is due to the finite energy resolution of the NRA detector [125].

4 Structure and Composition

4.1 Introduction

Successful nitriding of ASS comes along with the structural modification of the nitrogen enriched layer. In spite of numerous investigations [5, 12, 13, 32, 35, 41, 55, 89, 90, 92, 100, 114, 133], the nature of the microstructural changes induced by large amounts of incorporated nitrogen is not well understood. Key questions still awaiting clear answers are:

- Does the nitrogen enriched layer consist of a single phase or, rather, a mixture of phases?
- May the (predominant) phase be interpreted as a nitrogen interstitial solid solution?

In this Chapter the structure of plasma nitrided ASS is investigated. A combination of local chemical environment probe (CEMS, XANES and EXAFS) spectroscopies and global probe (XRD, NRA, GDOES, scanning electron microscopy (SEM)) techniques are used. The global probe techniques are employed to determine nitrogen concentration, nitrided layer thickness and a phase structure in the nitrided layer. The local probe techniques provide information about the local chemical environment, formal valence, coordination environment, bond length, disorder (thermal and static). In order to avoid the signal from the underlying stainless steel during XANES/EXAFS measurements, thick nitrided layers are needed, thus, plasma nitriding is employed.

The experimental conditions are described in section 4.2. The phase structure is presented in section 4.3.1. In section 4.3.2 nitrogen depth profiles are presented. Local probe measurements by CEMS, XANES and EXAFS are shown in section 4.3.3. The results are discussed in section 4.4 and summarized in section 4.5.

4.2 Experimental

AISI 304L samples were plasma nitriding at 400°C for 30 h to get the S phase. At this temperature nitrogen is present in solid solution. The formation of nitride precipitates

proceeds relatively slowly. Only near the surface a small amount of CrN precipitates has been detected. Two samples were nitrided at this temperature. One sample was polished with colloidal silica for 5 min to remove the surface layer with CrN precipitates. Another sample was Ar⁺ sputtered with 1 keV energy and 0.5 mA/cm² flux for 17 min. Third sample was nitrided at 550°C for 30 h. At this temperature the metal atom diffusion is significant and CrN is forming. It was used as a reference for CrN phase obtained during ASS nitriding.

4.3 Results

4.3.1 Phase structure

The samples nitrided at 400°C contain small amounts of CrN (Fig. 4.1 (a)). It is known that CrN starts to precipitate from the surface [134,135]. About 0.4 μm has been removed by polishing and ~0.8 μm by sputtering. In both cases the CrN peaks completely disappear indicating that the surface layer containing CrN is completely removed. A γ peak for the sputtered sample originates from a non-nitrided (masked) region in the sample. This region was avoided in all further described measurements.

Fig. 4.1 (b) shows XRD patterns of the non-nitrided sample and the ones nitrided at 400°C and 550°C. The spectrum of the non-nitrided sample is typical for austenitic

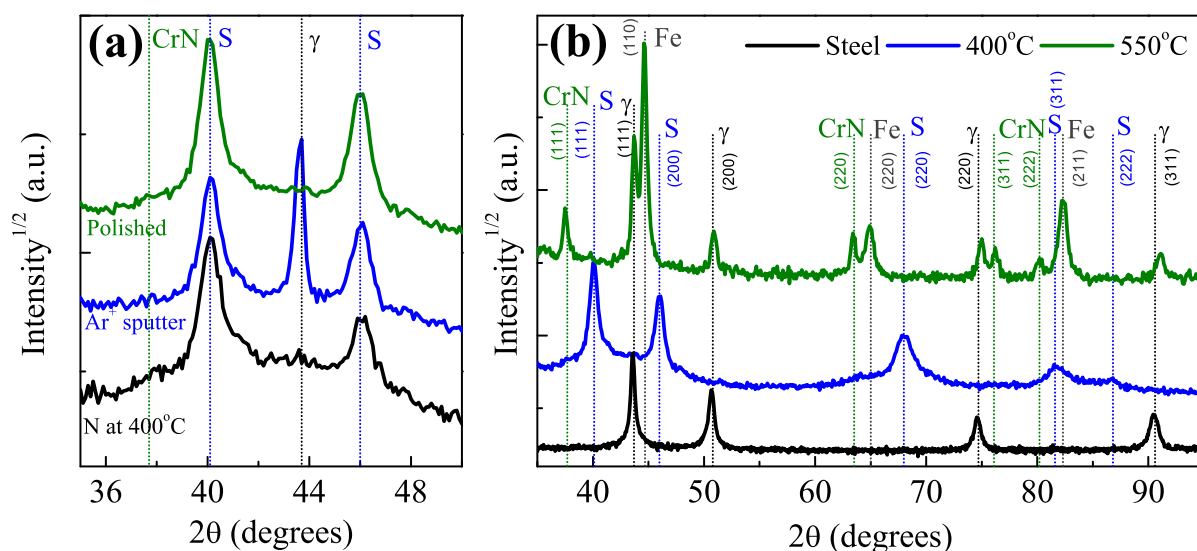


Figure 4.1: (a) X-ray diffraction patterns of the sample nitrided at 400°C and after removal of surface layer by polishing or Ar⁺ sputtering. (b) X-ray diffraction patterns of virgin, nitrided at 400°C and 550°C ASS.

stainless steel with the lattice parameter of 3.58 Å. After nitriding at 550°C, XRD shows a clear phase separation. Three phases can be identified: CrN, α -Fe and γ phase. The lattice parameters of 4.14, 2.87 and 3.58 Å are obtained for the CrN, α -Fe and γ phases, respectively. From the intensities of the α -Fe (110) and γ (111) reflections it is evident that the α -Fe phase is more abundant. Nitriding at 400°C leads to the formation of the S phase. The X-ray diffractogram shows the peaks which are shifted to lower angles from the peaks of the γ phase and are much broader. The shift and broadening of the peaks are associated with the S phase [7] produced by nitrogen supersaturation and associated stress caused by the nitrogen remaining in solid solution in the *fcc* lattice [35]. The peaks are asymmetric, which is associated with the nitrogen depth profile [34, 136]. The (200) peak is shifted more than the other XRD reflections. The more severe change in the lattice spacing of the (200) plane is explained in terms of a high number of stacking faults [13, 35–37] and higher residual stresses [36, 83, 114] associated with the (200) planes. In addition to high compressive stresses and plastic deformation, lattice bending [137], texturing [37, 90] and rotation as large as $\sim 5^\circ$ [53] have been reported in the literature. No other phases were detected in the sample nitrided at 400°C after polishing or sputtering. The lattice constant of 3.9 Å is obtained from all peaks, except for (200), which gives the lattice parameter of 3.94 Å.

4.3.2 Nitrogen depth profiles

Figs. 4.2(a) and (b) show N depth profiles of the samples nitrided at 400°C and 550°C, as determined by NRA and GDOES, respectively. The thickness of the nitrided layer is defined here as the point where nitrogen concentration is equal to half of the near-surface concentration. GDOES shows that nitrided layers in the samples nitrided at 400°C and 550°C are about 20 μm and 5 μm thick, respectively. The obtained profiles are averages over many grains with different orientations. Fig. 4.2(c) shows the morphology of the sample. The thickness of the nitrided layer varies strongly ranging from 8 to 5 μm . The average thickness is ~ 5.4 μm . The lower thickness compared to the sample nitrided at 400°C is probably due to much slower N diffusivity in CrN in comparison to α -Fe and ASS [138, 139], and very low nitrogen solubility in α -Fe [140]. The nitrogen concentration close to the surface for the sample nitrided at 550°C is ~ 14 at% constant over 4 μm . For the sample nitrided at 400°C the N surface concentration is ~ 27 at%. Assuming the steel composition to be Fe_{0.69}Cr_{0.18}Ni_{0.13}, renormalization gives the following compositions: 59 at% of Fe, 16 at% of Cr and 11 at% of Ni for the sample nitrided at 550°C, and 50 at% of Fe, 13 at% of Cr and 10 at% of Ni for the sample nitrided at 400°C. Cr has higher

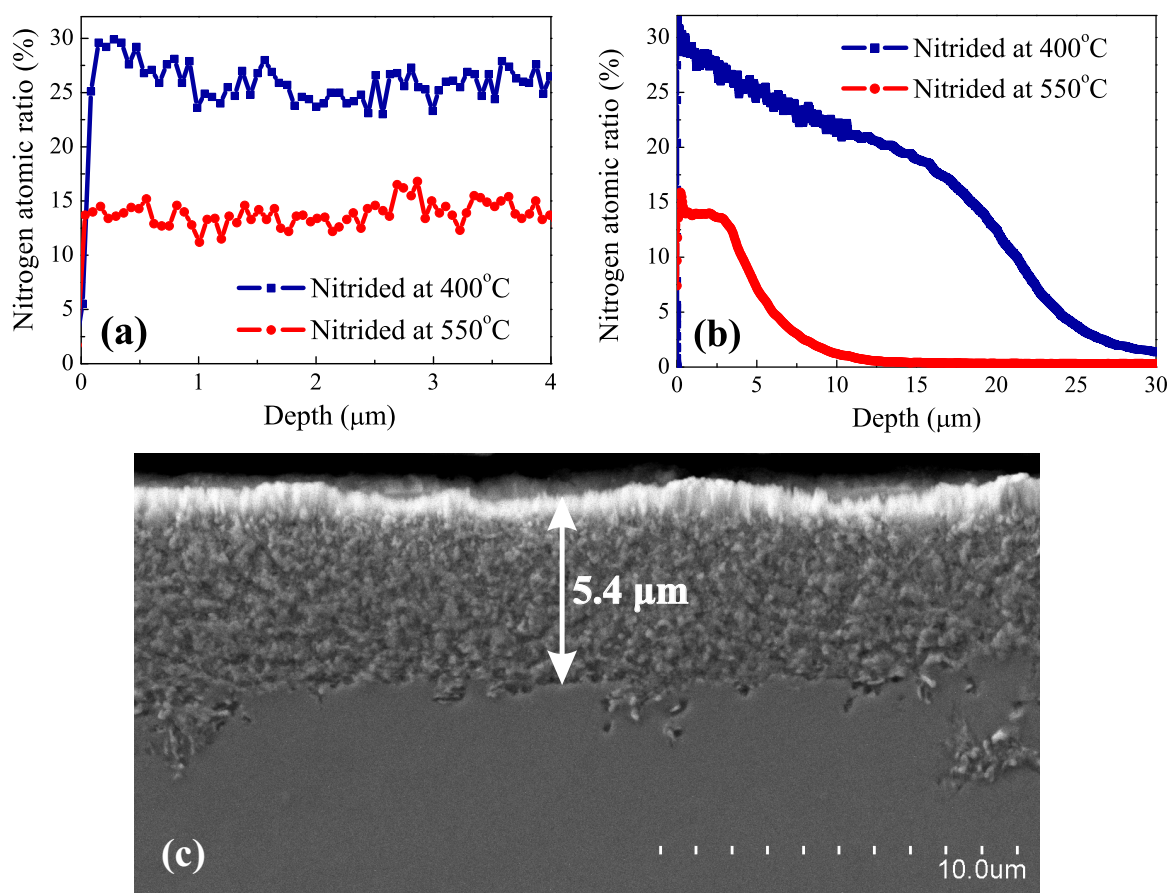


Figure 4.2: N depth distribution in the nitrided ASS: (a) NRA and (b) GDOES results of the samples nitrided at 400°C and 550°C. (c) Cross-section SEM micrograph showing the morphology of stainless steel nitrided at 550°C.

affinity to N than Fe and Ni, and is expected to trap nitrogen atoms [108]. Similar N and Cr atomic ratios in the plateau of the nitrided layer strongly suggests that almost all N is chemically bond to Cr after nitriding at 550°C. In the sample nitrided at 400°C ~13 at% of N is expected to be trapped by Cr and the remaining 14 at% to diffuse freely.

4.3.3 Local environment

4.3.3.1 Mössbauer results

The Mössbauer spectra recorded at room temperature are shown in Fig. 4.3 for the ASS reference and the samples nitrided at 400°C and 550°C. The CEMS-spectrum of the non-nitrided sample consists of a single peak. The peak is shifted by -0.11 mm/s in relation to α -Fe. The Mössbauer spectrum of the sample nitrided at 550°C consists of seven peaks. The central peak is again shifted by -0.11 mm/s. The spectrum shows the characteristic

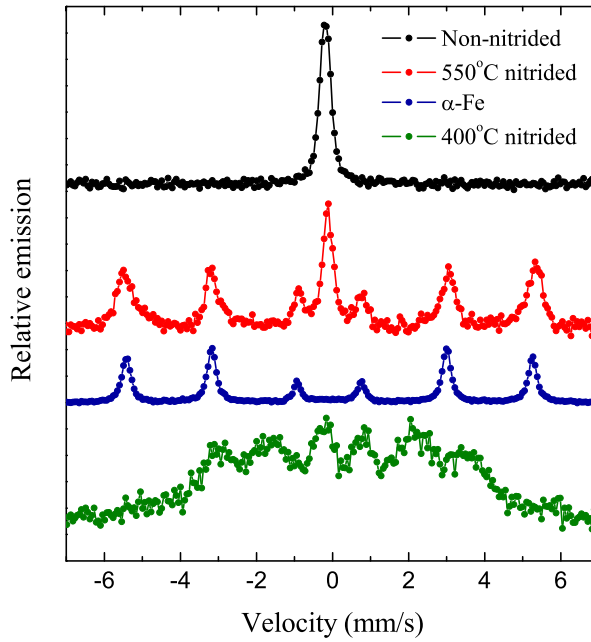


Figure 4.3: CEM-spectra of the non-nitrided sample and of the samples plasma nitrided at 550°C and 400°C. For comparison α -Fe CEM-spectra is included.

features of α -Fe. The central peak is approximately in the same position as the peak from the non-nitrided sample. Thus, Fe is present in two phases. The Mössbauer spectrum of the sample nitrided at 400°C consists of eight peaks. Two peaks around ± 5 mm/s are very weak. The spectrum is widely different from the ones of the reference samples.

A fit to the CEMS-spectra is shown in Fig. 4.4. For the samples nitrided at 400°C and 550°C, the high concentration of interstitial nitrogen atoms and the inhomogeneously distributed alloying elements (Ni, and Cr) render it impossible to characterize the surroundings of the resonating iron atoms by a unique internal magnetic field. Rather, a hyperfine field distribution has to be applied.

An isomer shift $\delta = -0.11$ mm/s and a small quadrupole splitting $\Delta = 0.14$ mm/s is obtained for the non-nitrided sample. The isomer shift is sensitive to the oxidation state of Fe, its value being typical for stainless steels (paramagnetic, γ -Fe-like symmetry) [91]. Thus, iron in the non-nitrided sample is metallic Fe^0 .

Non-spherical charge distribution results in quadrupole splitting of the energy state. However, in a radial symmetric charge distribution (cubic symmetry) no quadrupole splitting should appear. Here, the presence of a quadrupole splitting is the evidence for non-vanishing electric quadrupole moment. The reason for that might be some small lattice distortion, like tetragonal or monoclinic deformation, most probably induced by polishing during sample preparation.

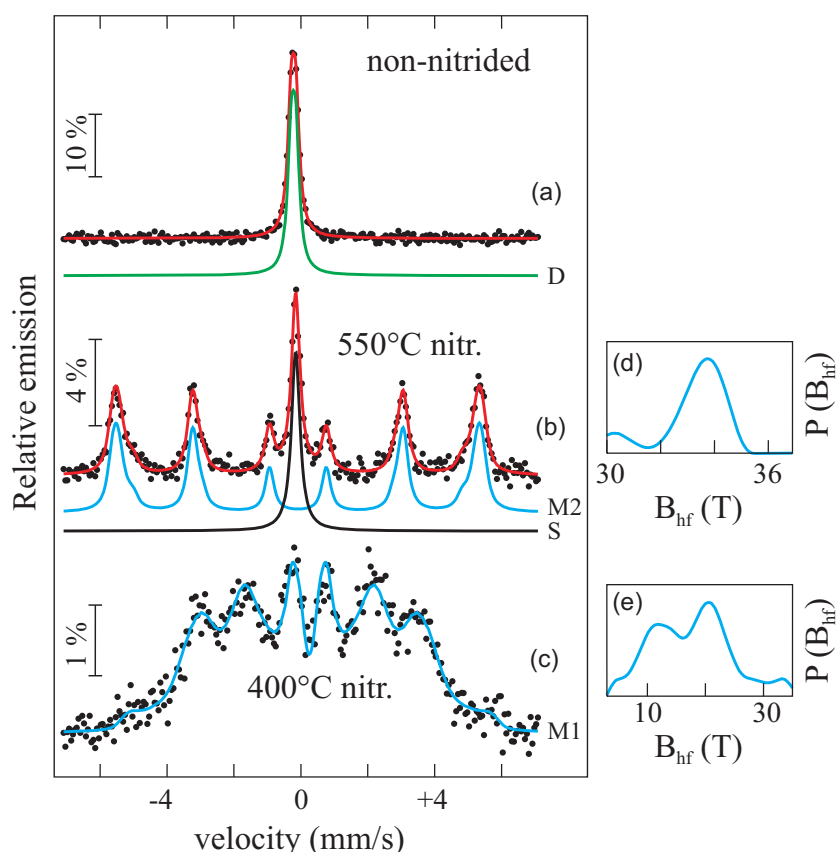


Figure 4.4: CEMS-spectra of the non-nitrided sample (a) and of the samples plasma nitrided at 550°C (b) and 400°C (c). The dots are experimental data and the lines are the fits. The scales of relative emission are shown individually. For the samples nitrided at 550°C and 400°C the hyperfine field distributions are shown in figures (d) and (e), respectively.

The CEMS-spectrum of the sample nitrided at 550°C was fitted by one singlet with $\delta = -0.04$ mm/s and a sextet with a magnetic hyperfine field distribution shown in Fig. 4.4(d) and $\delta = 0.02$ mm/s. The singlet corresponds to a paramagnetic Fe^0 . The sextet corresponds to a ferromagnetic Fe^0 . The isomer shift of the singlet differs from the isomer shift of the non-nitrided sample. However, it is still close to γ -Fe. The local maximum in the hyperfine fields distribution fits to α -Fe [141]. The distribution can be attributed to the statistical disorder/impurities or the size distribution within α -Fe. The relative area of the singlet is about 24 %.

The CEMS-spectrum of the sample nitrided at 400°C consists of a magnetic hyperfine split pattern. The shape of the pattern points to many possible surroundings of Fe. Therefore, the spectrum is fitted using the magnetic hyperfine field distribution, shown in Fig. 4.4(e), instead of discrete hyperfine fields. The isomer shift $\delta = 0.36$ mm/s and the range of hyperfine field distribution are similar to iron nitrides, like γ - Fe_4N [91].

4.3.3.2 XANES results

X-ray absorption measurements were done at the angle of incidence of 20° , 30° and 45° for Cr, Ni and Fe, respectively, to ensure that the information is collected from the same depth for all elements. At these configurations $\sim 63\%$ of X-rays are absorbed in the first $3.6\ \mu\text{m}$ and $\sim 86\%$ — in $7.2\ \mu\text{m}$. There is no difference in X-ray absorption spectra between sputtered and polished samples, thus, the results are shown for the sputtered sample.

ASS reference

Fig. 4.5 presents the XANES spectra of the Ni, Fe and Cr K-edges. In figures with XANES and EXAFS spectra each element in each sample has an individual color, i.e. iron in the non-nitrided sample has a black color and in the sample nitrided at 550°C is red. For the non-nitrided sample, Ni, Fe and Cr K-edges start at 8333, 7112 and 5989 eV, respectively. The shape of the K-edges for all elements look very similar (Fig. 4.5(d)). All three spectra have a pre-edge feature at 4 eV, and three typical maxima at 16, 24 and 47 eV above the absorption edge. Such XANES appearance is characteristic of the *fcc* structure [142]. Greaves et al. [142] showed that multiple scattering calculation including just one shell reproduce roughly the shape of the edge. At least three shells have to be included to get a good agreement with the experiment. The similarity between edges suggest that chemical environments and geometry are similar for Ni, Fe and Cr.

550°C reference

Fig. 4.5(f) shows XANES spectra from the sample nitrided at 550°C . The Cr XANES spectrum shows a well-defined edge feature (around 5 eV), the main peak (around 18.8 eV), and the second peak (around 32 eV). The pre-edge peak can be interpreted as the transition of the $1s$ electron of the absorber to bound states which consist of hybridized states of N $2p$, Cr $3d$ and $4sp$ orbitals [143,144]. The p-projected density of states is low close to the Fermi level due to the dominance of nitrogen $2p$ – chromium $3d$ states [145]. This results in weak edge peak intensity in comparison to that of non-nitrided stainless steel. The edge is shifted by 0.44 eV as compared to non-nitrided sample. The edge shift towards higher energies is related to the increase of the effective valence of absorbing atoms and which indicates a compound formation [146]. The position of the K-edge energy is similar to Cr^{3+} [144]. This corresponds to the formation of CrN. It should be noted that the Cr XANES spectrum from the sample nitrided at 550°C is almost identical to a CrN XANES spectrum reported in the literature [147].

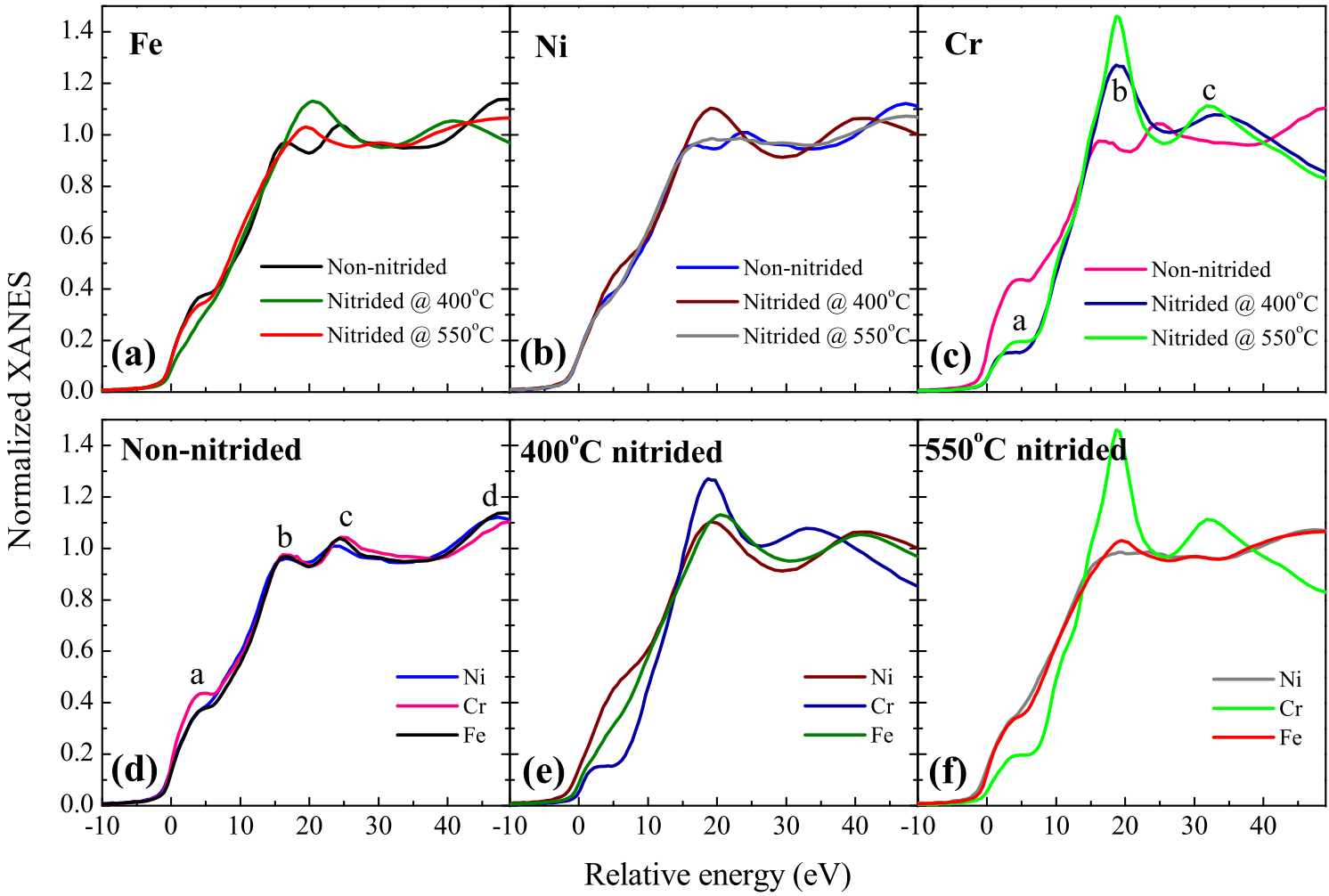


Figure 4.5: XANES spectra of Fe, Ni and Cr K-edges from non-nitrided and plasma nitrided samples. The panels (a)-(c) compare one element in three different samples. The panels (d)-(f) compare three elements in one sample.

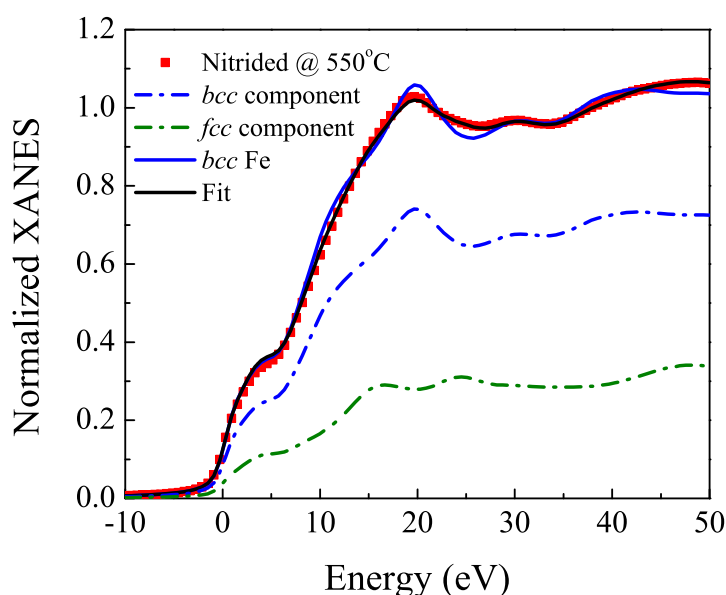


Figure 4.6: Fitting of the XANES Fe K-edge for the sample nitrated at 550°C. The Fe K-edge is simulated as a linear combination of 0.3 times the Fe K-edge spectrum of the reference sample (*fcc* component) and 0.7 times the Fe K-edge spectrum of the Fe reference foil (*bcc* component). The sample spectrum (dots) is compared to the fit result (black line) and *bcc* Fe (blue line).

Nitriding at 550°C results in significant changes of Fe environment (see Fig. 4.5(a)). The edge position is the same as for the non-nitrated sample. However, instead of the three peaks, above the absorption edge, there are only two peaks at 20 and 30 eV. The edge structure resembles closely that of *bcc* Fe, but is smoother (see Fig. 4.6). The deviation from *bcc* Fe is due to the presence of *fcc* iron. The phase fraction can be easily obtained by fitting a linear combination of the Fe K-edge spectrum of the reference sample (*fcc* component) and the Fe K-edge spectrum of an Fe foil (*bcc* component) [148]. The fitting results in 30 % of *fcc* iron.

The Ni spectrum is similar to the Fe one (see Fig. 4.5(f)). There is no absorption edge shift as compared to the non-nitrated sample. There is almost no absorption modulation above the absorption edge up to 35 eV. Above 35 eV there is a rise in the absorption with the maximum at 47 eV. When comparing the Ni XANES spectrum to those of FeNi alloys with different Ni contents reported in Ref. [149], it can be concluded that the Ni/Fe ratio is higher in *fcc* than in *bcc* phase.

S phase

In the sample nitrated at 400°C, the Cr result is very similar to the one for the sample nitrated at 550°C. The edge shift is 0.46 eV, being close to the value of 0.44 eV obtained

from the sample nitrated at 550°C. The peaks above the absorption edge are less intense than in the CrN reference sample. The intensity drops from 1.46 to 1.27 for the first peak and from 1.11 to 1.08 for the second peak. The positions of the peaks slightly shift to the higher energies (to 19.1 and 34.1 eV for the first and the second peaks, respectively). This can be attributed to a slightly smaller lattice parameter. A smoother shape can be attributed to a lower order of crystallinity. Despite these small differences, it is evident that already at 400°C Cr is in an environment similar to CrN.

The Ni and Fe spectra are similar, but are clearly different from the non-nitrated sample and the sample nitrated at 550°C. The absorption edge shows two maxima at 20.7 eV and 40.9 eV for Fe, and at 19.3 eV and 40.5 eV for Ni. A small phase shift between Ni and Fe is due to different atomic distances of absorbing atom from the scattering atoms. The intensity of Fe edge feature is lower than that of the non-nitrated stainless steel, while for Ni it is higher. The Fe spectrum is very similar to Fe₄N [150]. In Fe₄N, nitrogen 2*p* states are strongly hybridized with the $d(3z^2 - z^2)$ orbitals of the iron atom through a (*pdσ*)-type coupling with a weak contribution of 4*p* states [151]. The Fe K-edge is shifted by 0.07 eV in comparison to metallic Fe, while no absorption energy shift is observed for Ni. At higher energies, the intensity oscillations are due to multiple scattering effects. Thus, similar oscillations of Ni and Fe above the absorption edge indicate that Ni is strongly influenced by the co-existing Fe₄N phase. However, there is no absorption edge shift as observed for Fe. This suggests that Ni does not form a direct bond with N.

In summary, the Ni, Fe and Cr K-edges look very similar in the non-nitrated stainless steel. This suggests that chemical environment and geometry are the same for these elements. In the sample nitrated at 550°C, Cr forms CrN. Fe and Ni are found in *bcc* and *fcc* phases with 70 % of iron being in the *bcc* phase. Ni is found preferentially in the *fcc* phase. In the sample nitrated at 400°C, Cr is present in an environment similar to CrN, and Fe is in an environment similar to Fe₄N. Ni is in a metallic environment which is strongly influenced by Fe₄N, but does not form a direct bond with N.

4.3.3.3 EXAFS results

EXAFS oscillations

The EXAFS experimental data are displayed in Fig. 4.7. The EXAFS oscillations look very similar for all three elements in the non-nitrated sample. This suggests that the atomic coordination around Ni, Fe and Cr is similar. The differences in intensity between the elements is partly due to the insufficient self-absorption correction.

In the sample nitrated at 550°C, the Cr EXAFS oscillations are different from the ones in the non-nitrated sample. The Fe and Ni oscillations look similar and like the ones from the non-nitrated sample, but differ from Cr. The most significant differences can be observed in the lower k range.

The oscillations from the sample nitrated at 400°C exhibit much lower intensity in comparison to those of the reference samples. The damping increases with increasing k . This is an indication of a large static disorder. The oscillations of Cr show the lowest damping in comparison to the other elements. Cr oscillations correspond well to the oscillations from the reference sample nitrated at 550°C. The oscillations of Ni and Fe are shifted to lower k values compared to oscillations from the non-nitrated sample. This is an indication of increased interatomic distances. The shift is slightly higher for Fe than for Ni.

FT of EXAFS

The FT data of the Ni, Fe and Cr K-edges are compared in Fig. 4.8. The FT features of Ni, Fe and Cr from non-nitrated sample are characteristic of the *fcc*-structure [152,153] (Fig. 4.8(a)). For all the elements the $|\text{FT}(\chi \cdot k^3)|$ are almost identical. There are four strong amplitude peaks between 1.5 and 6 Å which correspond to distances $R \sim 2.2, 3.2, 4.2$ and 5 Å, respectively. The last two peaks strongly overlap. The peak at ~ 5 Å is strongly influenced by the multiple scattering. The peak around 1.5 Å in the Cr $|\text{FT}(\chi \cdot k^3)|$ is an artifact, as it tends to disappear when the high k range is omitted in the FT.

The $|\text{FT}(\chi \cdot k^3)|$ of the three elements from the sample nitrated at 550°C are compared in Fig. 4.8(c). The Cr $|\text{FT}(\chi \cdot k^3)|$ show five strong amplitude peaks between 1 and 6 Å whose distances R are $\sim 1.5, 2.5, 3.6, 4.7$ and 5.5 Å, respectively. The $|\text{FT}(\chi \cdot k^3)|$ of Cr looks similar to the $|\text{FT}(\chi \cdot k^3)|$ of CrN reported in the literature [144].

The $|\text{FT}(\chi \cdot k^3)|$ of Ni and Fe from the sample nitrated at 550°C show similar features. The $|\text{FT}(\chi \cdot k^3)|$ of Fe shows two strong and two weaker peaks between 1.5 and 5 Å. The distances R of the peaks are $\sim 2.2, 3.2, 3.7$ and 4.4 Å. The Fe FT data show features which are characteristic of the *bcc*-Fe-sites environment [154]. The EXAFS $|\text{FT}(\chi \cdot k^3)|$ of Ni is similar to Fe, but the peak at about 3.7 Å is missing or overlapping. The peak at ~ 4.4 Å is much broader. The FT of Ni also resembles the FT from the non-nitrated sample. This indicates that substantial amounts of Ni are present in both *fcc* and *bcc* phases.

The $|\text{FT}(\chi \cdot k^3)|$ of three elements from the sample nitrated at 400°C are compared in Fig. 4.8(b). The $|\text{FT}(\chi \cdot k^3)|$ of Cr is very similar to the $|\text{FT}(\chi \cdot k^3)|$ from the sample ni-

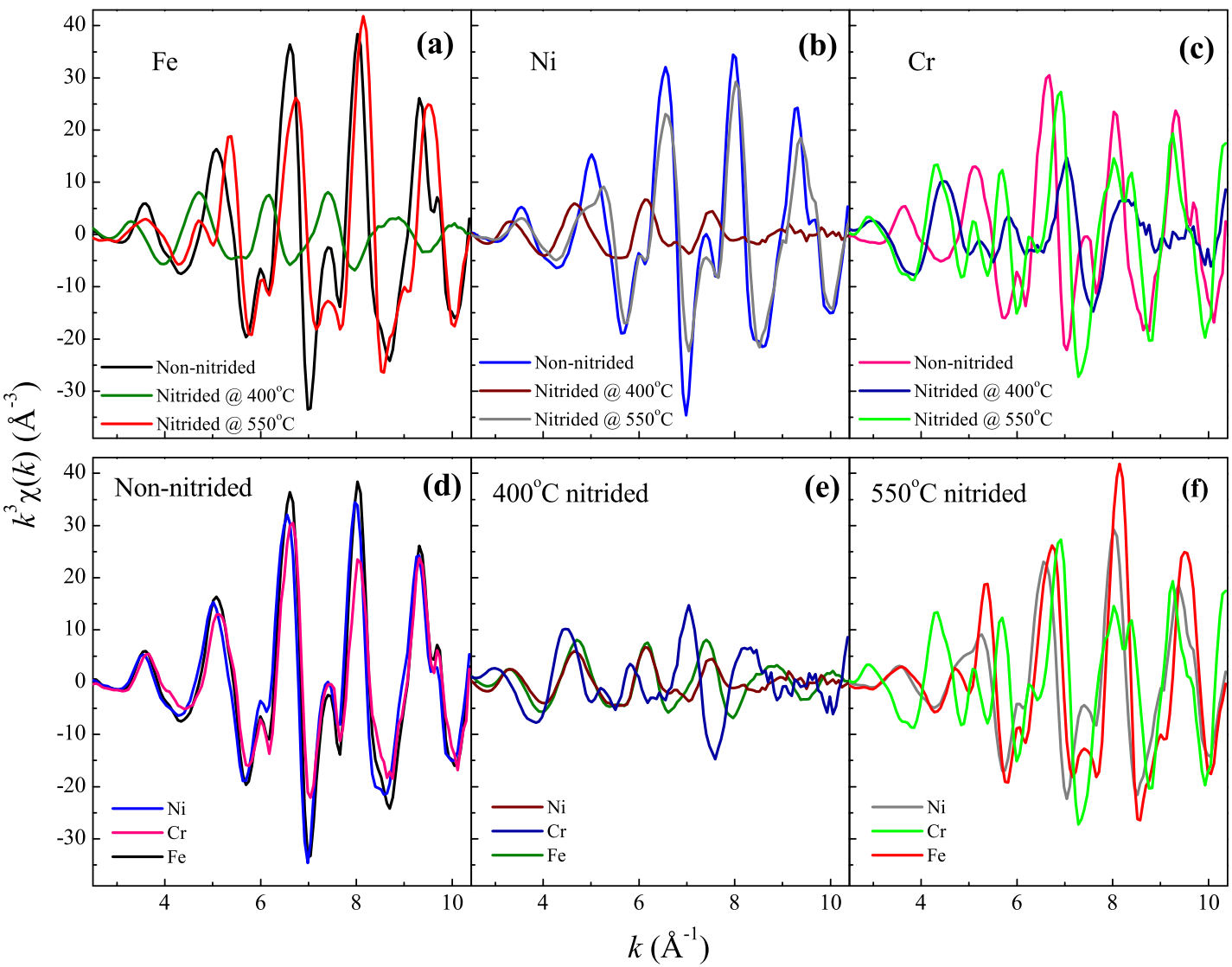


Figure 4.7: k^3 weighted EXAFS oscillations of Fe, Ni and Cr K-edges from non-nitrided sample and of the samples plasma nitrided at 550°C and 400°C. The panels (a)-(c) compare one element in three different samples. The panels (d)-(f) compare EXAFS oscillations of three different elements in three different samples.

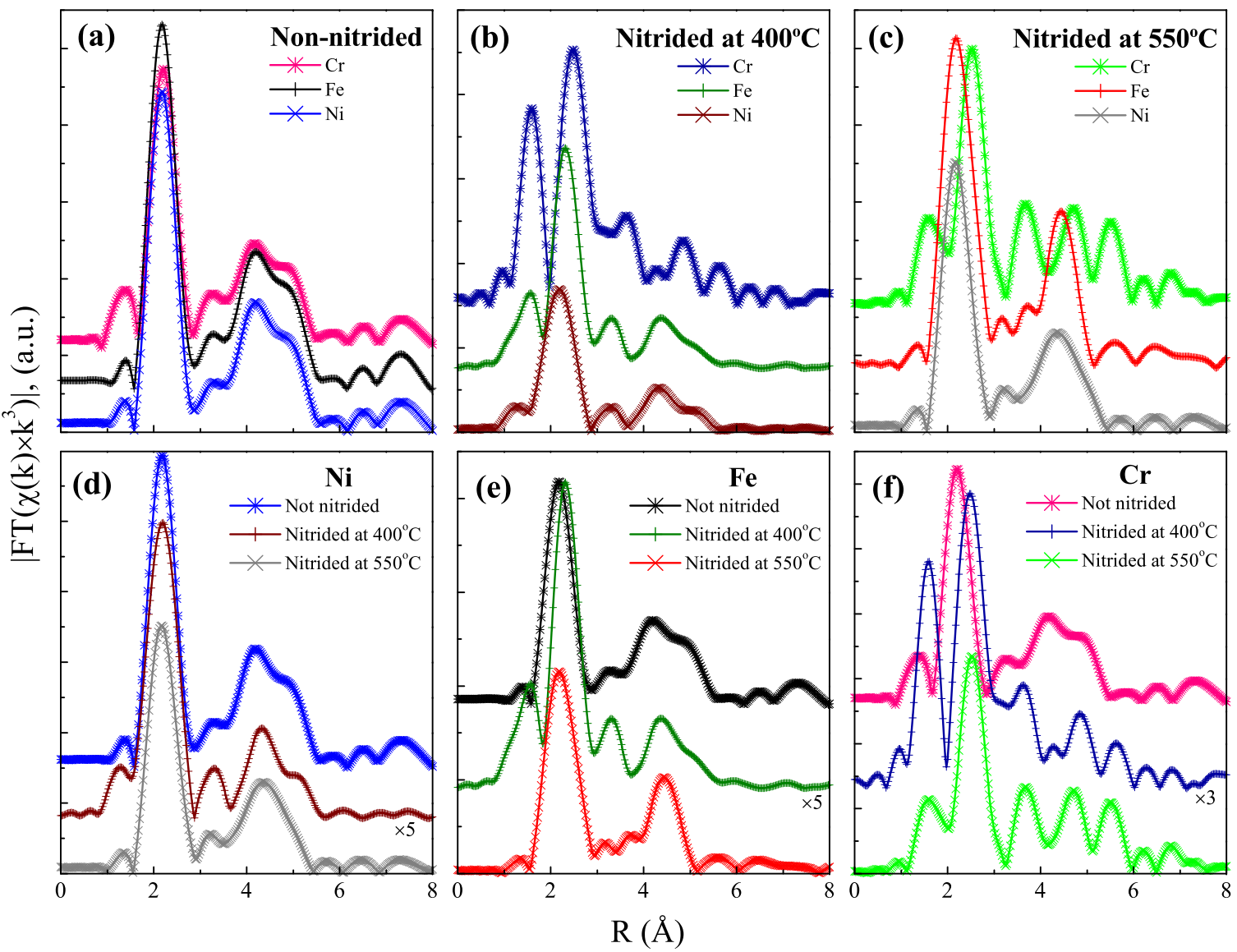


Figure 4.8: EXAFS $|\text{FT}(\chi \cdot k^3)|$ of Fe, Ni and Cr K-edges for non-nitrided and nitrided samples. The panels (a)-(c) compare EXAFS oscillations of three different elements for each sample. The panels (e)-(f) compare one element in three different samples.

trided at 550°C. Two additional peaks appear at the distances $R \sim 3.2$ and 4.2 \AA . The first one is due to a single scattering from N at the distance of 3.66 \AA . The second one possibly results from N at the distance of 4.60 \AA , or from a multiple scattering. The appearance of additional peaks for Cr is probably associated with a higher N concentration. Ni and Fe show four peaks. The last peak consists of two overlapping peaks. The peak positions are at $\sim 1.5, 2.3, 3.3$ and 4.4 \AA for Fe, and at $\sim 1.3, 2.2, 3.3$ and 4.3 \AA for Ni. The first peak comes from a single scattering from N in the first coordination shell. The intensities of the EXAFS FT for all three elements are much lower compared to the non-nitrided sample. The intensity of the peaks at higher distances also drop much faster, especially for Ni and Fe. This indicates a higher degree of disorder introduced by incorporated N.

EXAFS refinement

ASS reference

Ni, Fe and Cr EXAFS $|\text{FT}(\chi \cdot k^3)|$ and their fits are shown in Fig. 4.9. The results from the EXAFS refinement of the non-nitrided sample are summarized in Table 4.1. The amplitude reduction factors S_0^2 were obtained from the non-nitrided sample EXAFS data fitting by fixing the N_j value for the first shell to 12. These S_0^2 values were then used for the other samples. S_0^2 values depend on the element. This variation is probably partially due to the insufficient self absorption correction using the Tröger model [130]. The distances r_j , the energy shifts ΔE_0 and the Debye-Waller (DW) factors are similar for the three elements. Slightly higher values are obtained for Cr. The lattice parameter refines to 3.57 \AA . The DW factors are lower for the first two shells than for the more distant ones. This change is probably due to interstitials and due to the complex composition of steel [155]. These results indicate that Ni, Fe and Cr have similar environment and are dispersed homogeneously in the austenitic stainless steel.

550°C reference

The results from the EXAFS refinement of the sample nitrided at 550°C are presented in Table 4.2. The quality of the fit to the Cr EXAFS data suggests that the majority of Cr atoms is present in an environment identical to CrN. The lattice constant refines to 4.14 \AA as compared to the literature value of 4.1480 \AA [156]. The refined values of σ_j^2 for the first four shells are smaller than in the non-nitrided sample, which indicates a good crystallinity of the CrN phase. The r_j of the outermost shell is expanded by $\sim 1 \%$ compared to the nominal value of CrN, while the first four shells are contracted by $\sim 0.02\text{--}1 \%$. This indicates that a (small) fraction of the Cr atoms is found in chemical

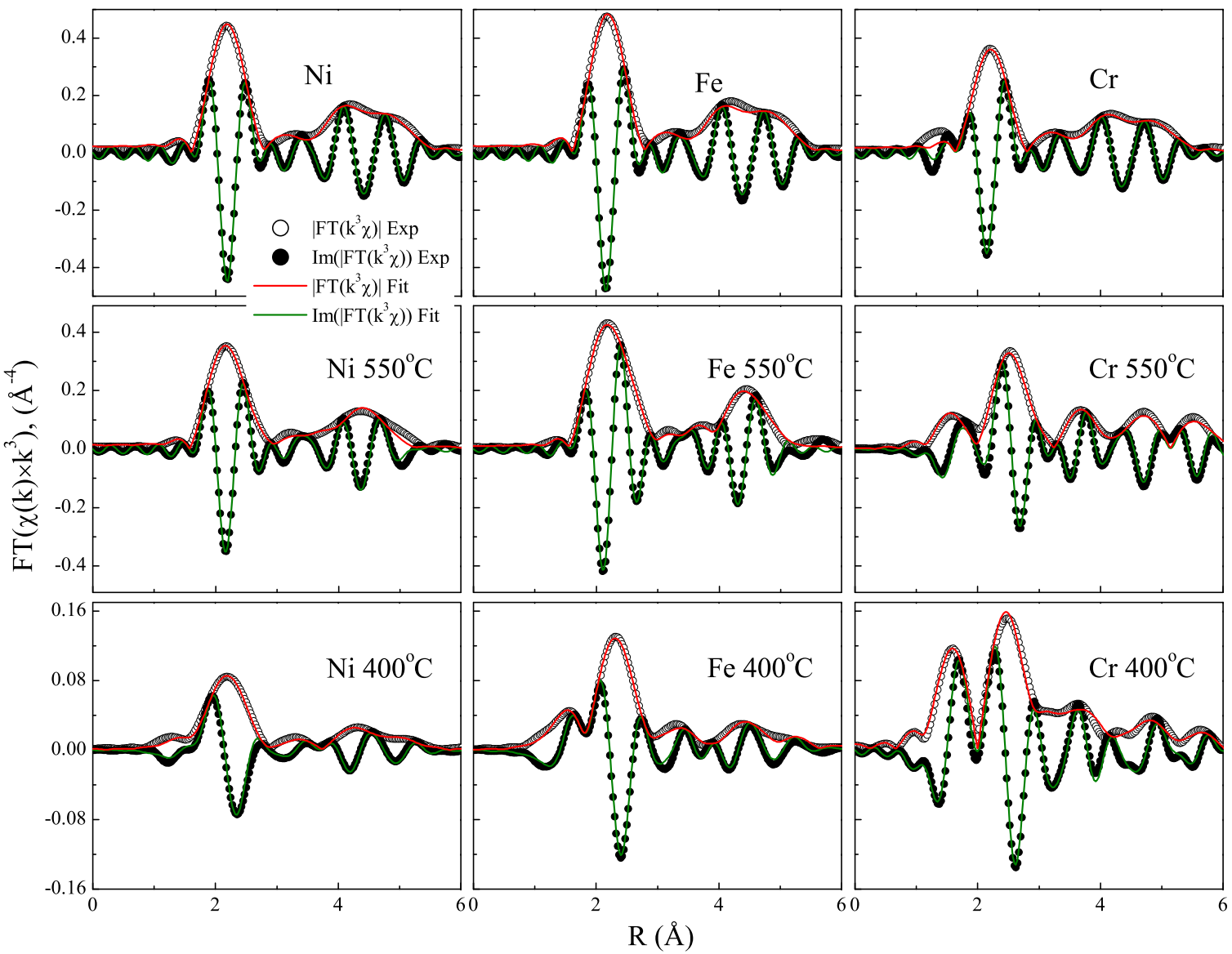


Figure 4.9: Ni, Fe and Cr EXAFS Fourier transforms and their fits for virgin and nitrified samples. Empty dot curves are FT amplitudes, filled dots are imaginary parts of FT, red lines are fits of FT amplitudes and green lines are fits of FT imaginary parts.

Table 4.1: Ni, Fe and Cr EXAFS refinement data of the non-nitrided sample: coordination numbers (N_j), distances (r_j), Debye-Waller factors (σ_j^2), energy scale offset (ΔE_0), amplitude reduction factors (S_0^2) and residual (\mathfrak{R}).

Path	N_j	r_j (Å)	σ_j^2 (Å ²)	ΔE_0 (eV)	S_0^2	\mathfrak{R} (%)
<i>Nickel</i>						
Ni-Fe ^(a)	12	2.52	0.0059	9.1	0.865	5.2
Ni-Fe ^(b)	3.8	3.57	0.0059			
Ni-Fe ^(c)	24	4.42	0.0076			
Ni-Fe ^(d)	12	5.17	0.0057			
Ni-Fe-Fe ^(e)	23.7	5.17	0.0082			
<i>Iron</i>						
Fe-Fe ^(a)	12	2.53	0.0059	9.3	0.913	6.6
Fe-Fe ^(b)	4.1	3.57	0.0059			
Fe-Fe ^(c)	24	4.42	0.0083			
Fe-Fe ^(d)	12	5.16	0.0122			
Fe-Fe-Fe ^(e)	24	5.16	0.0091			
<i>Chromium</i>						
Cr-Fe ^(a)	12	2.55	0.0063	10.6	0.714	5.1
Cr-Fe ^(b)	5.7	3.58	0.0063			
Cr-Fe ^(c)	24	4.43	0.0078			
Cr-Fe ^(d)	3.1	5.19	0.0081			
Cr-Fe-Fe ^(e)	18.1	5.19	0.0072			

surroundings that are different from CrN, possibly within the expanded austenite or in the interface adjacent regions of the CrN grains.

As described in section 3.4.2.4, Fe and Ni EXAFS from the sample nitrided at 550°C was fitted only with a *bcc* component. The addition of the *fcc* component increases the fit quality considerably, but results in a strong correlation between the parameters. The lattice constant of Fe refines to 2.84 Å, which is slightly lower than the value of 2.8664 Å for *bcc* Fe [157]. This is due to the lower density of *bcc* ferrite compared to austenite, and the associated strain. The lower σ_j^2 values compared to the non-nitrided sample indicate a good crystallinity. The lattice constant of Ni refines to 2.88 Å. The higher value, compared to Fe, is most probably obtained due to the *fcc* phase, which was not included in the fit. The obtained coordination numbers are lower than for Fe, especially for more distant shells.

From the N_j value of the first shell, the nitrogen concentration can be calculated. The steel composition is assumed to be Fe0.69Cr0.18Ni0.13. There can be 6 nitrogen atoms around chromium at maximum. Dividing the value of $N_j = 5.9$ by 6, multiplying by the Cr concentration and renormalizing, we obtain ~ 15 at% of nitrogen.

Table 4.2: Ni, Fe and Cr EXAFS refinement data of the sample nitrified at 550°C: coordination numbers (N_j), distances (r_j), Debye-Waller factors (σ_j^2), energy scale offset (ΔE_0), amplitude reduction factors (S_0^2) and residual (\mathfrak{R}).

Path	N_j	r_j (Å)	σ_j^2 (Å ²)	ΔE_0 (eV)	S_0^2	\mathfrak{R} (%)
<i>Nickel bcc</i>						
Ni-Fe ⁽ⁱ⁾	7.6	2.49	0.0045	6.5	0.865	8.2
Ni-Fe ^(j)	1.4	2.88	0.0042			
Ni-Fe ^(k)	9.4	3.97	0.0087			
Ni-Fe ^(l)	16.7	4.78	0.0043			
Ni-Fe-Fe ^(m)	2.8	5.11	0.0044			
Ni-Fe-Fe ⁽ⁿ⁾	1.7	5.59	0.0042			
<i>Iron bcc</i>						
Fe-Fe ⁽ⁱ⁾	8	2.46	0.0051	3.0	0.913	5.4
Fe-Fe ^(j)	5.0	2.84	0.0039			
Fe-Fe ^(k)	12	3.99	0.0099			
Fe-Fe ^(l)	20.1	4.76	0.0101			
Fe-Fe-Fe ^(m)	15.5	4.98	0.0076			
<i>Chromium</i>						
Cr-N ^(f)	5.9	2.05	0.0022	10.6	0.714	9.4
Cr-Cr ^(a)	11.5	2.91	0.0031			
Cr-Cr-N ^(g)	7.9	4.14	0.0036			
Cr-Cr ^(c)	24	5.06	0.0051			
Cr-Cr-Cr ^(e)	24	5.93	0.0079			

S phase

The EXAFS refinement results from the sample nitrified at 400°C are presented in Table 4.3. For Cr, a slightly different fitting model than that for Fe and Ni is adapted to get a better fit as described in section 3.4.2.4. The scattering path (*h*) (see Fig. 3.15) is included to account for the peak at 3.2 Å. The scattering path (*b*), which accounts for the peak at 4.2 Å, is not included in the model, as the coordination number tends to 0 during the refinement. The amount of N around Cr is almost the same as in the CrN reference. Smaller N_j for the scattering path (*a*) and much higher DW factors, than in the sample nitrified at 550°C, indicate a much higher disorder. The lattice parameter is lowered to 4.08 Å, which is by 1.4 % lower than for the CrN reference. Smaller r_j values and a higher phase shift, compared to the CrN reference sample, indicate a compressive strain. Nevertheless, the similar nitrogen amount, N_j , and r_j values suggest that Cr forms already at 400°C a phase that is similar of CrN. The differences between the values are probably due to the small size of the inclusions.

Table 4.3: Ni, Fe and Cr EXAFS refinement data of the sample nitrated at 400°C: coordination numbers (N_j), distances (r_j), Debye-Waller factors (σ_j^2), energy scale offset (ΔE_0), amplitude reduction factors (S_0^2) and residual (\mathfrak{R}).

Path	N_j	r_j (Å)	σ_j^2 (Å ²)	ΔE_0 (eV)	S_0^2	\mathfrak{R} (%)
<i>Nickel</i>						
Ni-N ^(f)	0.3	1.83	0.0043	10.3	0.865	11.2
Ni-Fe ^(a)	12	2.60	0.0213			
Ni-Fe-N ^(g)	0.7	3.82	0.0132			
Ni-Fe ^(b)	3.6	4.00	0.0221			
Ni-Fe ^(c)	8.6	4.65	0.0128			
Ni-Fe-Fe ^(e)	9.5	5.42	0.0171			
<i>Iron</i>						
Fe-N ^(f)	1.8	1.93	0.0063	16.8	0.913	9.0
Fe-Fe ^(a)	10.7	2.71	0.0158			
Fe-Fe-N ^(g)	2.2	3.89	0.0111			
Fe-Fe ^(c)	16.3	4.73	0.0182			
Fe-Fe-Fe ^(e)	7.1	5.51	0.0170			
<i>Chromium</i>						
Cr-N ^(f)	5.7	2.01	0.0039	15.1	0.714	9.1
Cr-Cr ^(a)	9.7	2.88	0.0093			
Cr-N ^(h)	7.4	3.66	0.0039			
Cr-Cr-N ^(g)	3.9	4.08	0.0058			
Cr-Fe ^(c)	24	5.03	0.0181			
Cr-Fe-Cr ^(e)	24	5.90	0.0233			

The N_j value from the first Fe-N shell is 1.8. This is close to the theoretical value of 1.5 for the γ' -Fe₄N phase (the coordination number is recalculated discarding the ordering). The lattice parameter obtained from the fit is 3.89 Å which is close to the lattice parameter of the γ' -Fe₄N phase, the latter being equal to 3.799 Å [158]. The larger value can be attributed to the higher amount of N and the associated lattice expansion. The scattering paths, which do not include nitrogen, result in N_j values much lower than in the non-nitrated sample, especially for more distant shells. The σ_j^2 are much larger than in the non-nitrated sample. Only for the first shell the DW factor is lower, which is due to the covalent bonding of iron and nitrogen. This means that the lattice around Fe is highly distorted. When a high degree of disorder is present ($\sigma^2 \approx 0.01$ Å²), the integral under the coordination shell peak is not conserved anymore [159]. This is related to the fact that $|\text{FT}(\chi \cdot k^3)|$ is not truly the radial distribution function, even if its major peaks represent the shells of neighboring atoms [159]. The origin of this is the finite range of k values (2.5-10.4 Å⁻¹ in the present work). The region of $k \leq 2.5$ Å⁻¹ of EXAFS oscillations is

usually cut off, as it is intermixed with the density-of-states features near the absorption edge. The region $k > 10.4 \text{ \AA}^{-1}$ had to be discarded because of a low intensity-to-noise ratio. For materials with large static disorder a pair distribution function becomes broad and sometimes asymmetric. Broad tails of a pair distribution function contribute to EXAFS only at low k values, which mainly influence the right side of the peaks. As these contributions are cut off from EXAFS spectra, this results in an apparent decrease in a coordination number. Also, it yields that r_j is not an average distance, but a distance of the closest approach [160]. Nevertheless, the fit quality suggests that Fe most likely forms a phase similar to γ' -Fe₄N.

Despite the similarities between Ni and Fe EXAFS FTs, Ni and Fe show one major difference: there is almost no nitrogen around Ni atoms. The coordination number for the first shell (Ni-N) is 0.3, while for Fe-N it is 1.8. The r_j values are lower than those of Fe and Cr. The difference in the r_j values between Ni and Fe is higher for the first shell. The lattice parameter calculated from the scattering path (*a*) assuming *fcc* structure yields the value of 3.68 Å, which is ~5 % lower than that of Fe. The lattice parameter calculated from the scattering path (*e*) yields the value of 3.83 Å, which is only ~1.5 % lower. The lattice parameter of *fcc* Ni is 3.52 Å. The DW factors are approximately the same as for Fe, except for the scattering path (*a*). The value of this scattering path is higher than that of Fe and also higher than the DW factor of the most distant shell. That indicates a higher disorder in the immediate surrounding of Ni than for a longer range.

The total N concentration calculated from EXAFS refinement data is 28 at%. About 12.5 at% of N is found around Cr, 15 at% around Fe and 0.5 at% around Ni.

In summary, the Ni, Fe and Cr Fourier transforms and refined parameter values are very similar for the non-nitrided stainless steel. This confirms that these elements are distributed homogeneously. In the sample nitrided at 550°C, Cr is found to be in the environment of CrN. Iron and nickel form α and γ phases. The Ni/Fe ratio is higher in the γ phase than in the α phase. A high degree of crystallinity of all phases is confirmed by low DW factor values. After nitriding at 400°C, Cr is in an environment very similar to CrN, and Fe is in an environment similar to γ' -Fe₄N. Ni exhibits a similar environment as Fe, but there is almost no nitrogen around it. Three different lattice parameters were obtained from the Cr, Fe and Ni EXAFS fits, which are 4.08, 3.89 and 3.68 Å, respectively.

4.4 Discussion

All the analysis results (global and local) demonstrate that plasma nitriding at 400°C induces significant changes in austenitic stainless steel. The X-ray diffraction pattern shows a set of broad peaks that appear to the lower 2θ angles side of each austenite peak. The peak positions correspond to the expanded lattice parameter of the γ phase due to the incorporation of N, as reported in the literature [8,34,36]. About 27 at% of nitrogen is detected in the first 4 μm by NRA. The EXAFS refinement yields 28 at%. In the literature, the highest reported amount of nitrogen in austenitic stainless steel is ~ 38 at% [93]. This is beyond the solubility that can be expected, taking into account the possible nitrides that can develop [93] (of which CrN will dominate) and the equilibrium lattice solubility of nitrogen in austenite, which is ~ 4 at% [66]. This high nitrogen concentration was achieved by complete nitriding of ASS flakes [93]. In the present study, nitrogen was always able to diffuse towards the bulk, thus such high concentrations have not been reached.

The XANES and EXAFS results suggest that Cr is in a state similar to CrN. The lattice parameter of *fcc* CrN is 4.14 Å, and the EXAFS refinement yields 4.08 Å. This phase could not be identified by XRD. However, the increased background around 43° in the XRD pattern might correspond to CrN (200) line. An additional broad line is also observed around 64° , which corresponds to the CrN (220) line. The fact that Cr forms a phase similar to CrN, but cannot be detected by XRD, suggests that it forms very small Cr-enriched regions in the matrix [38].

CEMS, XANES and EXAFS show iron to be in the phase similar to γ' -Fe₄N. The lattice parameter obtained from EXAFS analysis is 3.89 Å. It corresponds to the lattice expansion by 2.6 % compared to γ' -Fe₄N lattice parameter of 3.799 Å. The observed higher values can be expected due to higher N concentration. The lattice parameter of the S phase is 3.9 Å and 3.94 Å, as obtained from the (111) and (200) XRD peak positions, respectively. The measured values by XRD represent an average lattice parameter. Taking into account the steel composition (Fe_{0.69}Cr_{0.18}Ni_{0.13}), the average, calculated from Fe, Cr and Ni lattice parameters obtained by EXAFS, yields the lattice parameter of 3.9 Å. Thus, the lattice parameter obtained from the EXAFS analysis agrees very well with the value obtained by XRD. The coordination number from the first Fe-N shell refines to 1.8, while for γ' -Fe₄N it is 1.5 if nitrogen ordering is not taken into account. $N_j = 1.8$ corresponds to 15 at% in the sample. From NRA results, 14 at% of N can be associated with Fe-N bonds assuming stoichiometric CrN and the absence of Ni-N bonds. 12.5 at% would be needed to form γ' -Fe₄N phase.

XANES shows that Ni is strongly affected by the Fe₄N-like phase, but almost no N is

detected around Ni. The lattice parameter deduced from Ni EXAFS is 3.68 Å, which is 4 % lower compared to Fe, but 5 % higher as compared to pure Ni. The DW factor indicates the deviation of ± 0.15 Å. Despite the large DW factors, the difference between the Fe and Ni lattice parameters is still quite significant. This difference suggests that Ni forms Ni-rich regions. In the gas nitrated ASS foil, almost the same amount of N around Ni, Fe and Cr has been detected by the EXAFS investigation [39,40]. This is most probably associated with much higher amounts of nitrogen introduced by gas nitriding which is about 35 at%.

All the differences between metal atoms indicate that the S phase is a non-homogeneous material, where Cr and Ni form domains in the Fe₄N-like matrix. The distribution of these domains is probably homogeneous with the nitrogen occupying interstitial (octahedral) sites. However, its concentration is fluctuating. Around Cr there is 3 times more N than around Fe, and almost no N around Ni. Thus, the S phase is composed of very small zones being rich in Cr with high N fraction and rich in Ni with low N fraction, incorporated in a Fe₄N-like matrix. Such variation in the local N concentration induces lattice strain gradients and, consequently, local stresses which are consistent with the observed broad XRD peaks and large DW values.

Austenite with a high nitrogen content is metastable/unstable with respect to CrN, ferrite, or austenite and tends to decompose. The S phase decomposes upon thermal annealing to CrN and the α and γ phases [12,35]. Effectively, for the process times applied for nitriding, the development of CrN from the expanded austenite is hindered at the temperatures below 450°C. This was verified by the X-ray diffraction analysis and by thermal analysis of nitrogen equilibrated thin foil [161]. However, for very long nitriding times (~ 30 h) CrN forms in the near surface region. Presumably, this slow kinetics can be attributed to a limited mobility of substitutional alloying elements at low temperatures, as compared to the mobility of interstitial elements.

From thermodynamical point of view the situation is sketched in Fig. 4.10. At low N concentrations, where d^2F/dC^2 is positive, N stays as a solid solution (α' -phase). It is metastable with respect to CrN (β -phase), however, the system has to overcome a nucleation barrier. When the N concentration is increased, the instability arises in the part of the curve where the curvature, d^2F/dC^2 , is negative. Within this spinodal region an alloy of composition a can split into b and c and so reduce its free energy. Such regions of solute-enriched α'' , sharing the same crystal lattice as α' , are known as Guinier-Preston (GP) zones [72]. The formation of the β -phase still requires the system to overcome a nucleation barrier. In this case, the solute enhanced region α'' , although metastable with respect to β , will still form when the rate of its formation is faster than the kinetics of

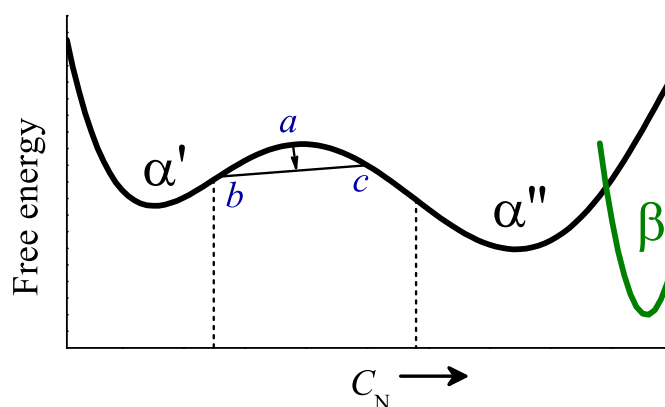


Figure 4.10: Schematic representation of a free-energy-composition curve for heterogeneous alloys. The curvature, d^2F/dC^2 , is negative in the part between the dashed lines and positive elsewhere.

the nucleation and growth of the more stable β -phase.

The formation of the S phase depends on the interplay between the supersaturation and decomposition kinetics. If the decomposition rate (metal atom diffusion) is significantly faster than the saturation rate (nitrogen supply), the decomposition can start in the N content ranges with $d^2F/dC^2 > 0$ — nucleation and growth of CrN crystallites will take place. On the contrary, if the saturation rate is significantly faster than the decomposition rate, the nitrogen concentration will locally rise without any considerable changes in the matrix and the system is expected to reach the spinodal region. In this case spontaneous decomposition will occur.

As Cr has highest affinity to N, it will attract the N in its immediate surrounding. Moreover, the diffusion of Cr in ASS is faster than Fe and Ni [162]. It has been reported that CrN results as the first precipitate upon thermal annealing, and that the surrounding γ phase loses nitrogen in favor of CrN [30]. If the saturation rate is large, the decomposition would occur in the γ' -Fe₄N surrounding, i.e. $\gamma(\text{Cr,Fe, Ni, N}) \rightarrow \text{CrN} + \gamma'\text{-Fe}_4\text{N} + \text{Ni}$ will take place. It is known in the literature that for γ' -Fe₄N the elastic constants are such that $2C_{44} - C_{11} + C_{12} < 0$ (where C_{ij} are single-crystal elastic constants) [132], thus the composition waves should extend along the four $\{111\}$ planes [163]. If large N amounts are needed for the system to become unstable, the CrN-like domains would form along the $\{111\}$ planes. In the sample with the (111) orientation the domains would form perpendicular to the surface and in the (001) oriented sample they would make the angle of 55° with the surface. For lower saturation rates, the following reaction will occur first $\gamma(\text{Cr,Fe, Ni, N}) \rightarrow \text{CrN} + \gamma(\text{Fe, Ni})$. In an *fcc* metal $2C_{44} - C_{11} + C_{12} > 0$, which is also the case for ASS, spinodal decomposition should then yield the composition waves primarily

along the $\{100\}$ planes [163]. Then, the coherent domains would form perpendicular to the surface and at the angle of 55° in the (001) and (111) oriented sample, respectively. A further increase in the local N concentration will saturate the surrounding $\gamma(\text{Fe,Ni})$ phase and induce further decomposition, $\gamma(\text{Fe, Ni, N}) \rightarrow \gamma'\text{-Fe}_4\text{N} + \text{Ni}$. The increase in the nitrogen content in the Fe-rich matrix changes its soft elastic directions from $\langle 001 \rangle$ to $\langle 111 \rangle$. As the CrN zones are already along the $\{100\}$ planes, this must yield large local stresses and structural distortions.

The diffusion of metal atoms depends on the temperature and can be influenced by radiation defects, local nitrogen concentration, stress, . . . At 400°C the diffusion of metals atoms appears to be relatively slow, as no nucleation of CrN could be observed, except in a thin superficial layer. Also, other strong nitride forming elements such as Mn or Mo might participate in nitride formation. The separation starts from the surface where nitrogen concentration reaches a critical value first. As nitriding is continued, the phase separation travels with the nitrogen concentration front. Small diffusivity of the metal atoms hinders the phase separation, thus only small domains can be formed. Nevertheless, long nitriding times (longer than 30 h) are sufficient for an incoherent CrN formation in the top layer less than $0.4 \mu\text{m}$ in thickness, as it was observed in the present study. Here nitrogen concentration is the highest, thus providing the largest driving force for the longest time, compared to deeper layers. At 550°C the diffusivity of metal is much higher, resulting in the CrN precipitate formation already detectable by XRD.

Nitrogen concentration depends on the interplay between the supply and diffusion rates. For a given supply rate, higher diffusivity yields lower nitrogen concentrations for higher temperatures. The nitrogen supply rate at the surface strongly depends on the nitriding techniques due to different processes they are based on. During gas nitriding, nitrogen molecules have to split on the surface before diffusing into the bulk. Gas nitriding is a para-equilibrium process, and a dissociation rate of nitrogen molecules depends on the difference between the nitrogen concentration equilibrium between the solid and the gas phase and the actual nitrogen concentration. As a consequence, to saturate the system up to a spinodal point probably takes longer as compared to the plasma as well as the ion beam nitriding, which are non-equilibrium processes. During the plasma and ion beam nitriding active species (ions, atoms, radicals) are produced in the nitriding environment, rather than at the metal surface. During the ion beam nitriding, ions are directly implanted a few nm below the surface, while during the plasma nitriding physisorption of active species takes place. This mechanism of physisorption-induced chemical reactions differs from the chemical modification by ion implantation by the fact that the initial nitride formation takes place at the surface followed by the diffusion of nitrogen to the bulk

in contrast to the ion implantation, where the nitride formation takes place through the superficial layer affected by the ion implantation [164–166]. During the ion beam nitriding sputtering becomes important at ion energies in excess of the sputtering threshold. Thus, the S phase formed in some subsurface layer exists for a finite time, depending on the sputtering rate. Finally, when a steady-state is reached, the layer grows and is removed at the same rate. Thus any nitrated region has only a final life-time before being removed due to sputtering.

It has been reported that plasma nitriding of ASS at 450°C results in very fine CrN precipitates in the size range of a few nanometers [90,101]. In addition, the areas with a lamellar structure have been detected [12]. Recently it has been suggested that Cr forms coherently diffracting nitride platelets, or so-called mixed substitutional–interstitial atom clusters [38] after gas nitriding at 445°C. However, the results of the Ref. [38] are in question as the samples were inhomogeneous due to the partial decomposition of the nitrated material and development of CrN. The authors repeated the experiment with a shorter nitriding time to avoid the CrN precipitation and still observed changes in the microstructure, but discarded both ideas and described the structure as more diffuse with some degree of ordering [39,40]. In Refs. [39,40] the nitriding for 18 h presumably resulted in the concentration wave with a lower amplitude as compared to nitriding for 24 h where ~59 % of Cr is found in the CrN phase [38]. The results of the present study indicate that already at 400°C the decomposition of nitrated ASS is most likely spinodal and results in the formation of Cr and Ni domains in the Fe matrix. The development of such domains in the S phase would be consistent with three different environments, the broad peaks in XRD and the large DW factors obtained from the EXAFS fits. The spinodal decomposition mechanism would be consistent with the diffuse structure deduced from EXAFS observations reported in the literature [39,40]. For spinodal decomposition, the interfaces between the domains can be sharp or with a gradually varied composition. The domains with sharp interfaces will have a fixed lattice constant, while the lattice constant of the domains with gradually varied composition will change with concentration. The broad XRD peaks and large DW factors suggest that the domains have varied composition or that there are lattice strain gradients between sharp boundaries. According to Cahn and Hilliard [68], the specific interfacial free energy will be smaller for more diffuse interfaces. However, this decrease in energy can only be achieved by introducing more material at the interface of nonequilibrium composition, thus, at the expense of the increasing free energy of the mixture. Consequently, for a local equilibrium the composition variation will be such that the sum of gradient energy and free energy terms is at the minimum. With the current set of data it is not possible to deduce at which nitrogen concentration during

plasma nitriding conditions the decomposition takes place. A large structural disorder observed in the S phase suggests that the CrN domain formation starts in the metallic matrix. However, further experimental and theoretical studies would be needed to reveal the outset of stainless steel decomposition (CrN in metallic environment or Fe₄N-like environment).

At 550°C the diffusivity of metal, as well as nitrogen atoms, is much higher. The EXAFS results demonstrate that N is only bonded with Cr, while the rest of the matrix is metallic. This corresponds quantitatively to the homogeneous nitrogen concentration of ~14 at% over the nitrided layer, as deduced by NRA, and to the formation of CrN in the whole layer. The formation mechanism (nucleation and growth or spinodal decomposition) cannot be deduced as both the spinodal decomposition in the final stages or nucleation and growth of CrN will result in CrN crystallites which are experimentally observed (XRD diffraction, small DW factors).

It follows from the discussion above that for the formation of the S phase there is a certain processing window. The formation and growth of the S phase mainly depends on the interplay of the supersaturation and decomposition rates. Below 300°C the implanted nitrogen develops a ballistic depth profile [84], as the diffusion of interstitial nitrogen is hindered. Above 450°C, the decomposition rate becomes significant, and CrN starts to form [12] which is detrimental for the nitrided ASS performance. As CrN starts to form from the surface, the layer containing CrN can be removed after nitriding, thus benefiting from faster N diffusion and consequently, shorter nitriding times. However, it must be noted that metal matrix remains metallic and thus, different from that obtained at lower temperatures. In the case of ion beam nitriding, the surface is constantly sputtered during nitriding. Even if CrN forms in the surface layer, the optimum results can be obtained if the decomposition rate is balanced by the sputtering rate.

4.5 Summary

The structure and composition of the plasma nitrided austenitic stainless steel have been investigated by combining global and local probe techniques. Nitriding at 400°C for 30 h leads to the formation of the S phase and small amounts of CrN in a thin surface layer. The structure of the S phase was compared to the virgin ASS and the reference sample nitrided at 550°C. In the later case, Cr forms the CrN phase.

It has been found that in the S phase Fe, Cr and Ni have different local chemical environments. The comparison with the reference sample shows that Cr has a CrN-like environment, Fe is similarly arranged to γ' -Fe₄N, and Ni has a metallic environment.

Different coordination numbers of Cr-N, Fe-N and Ni-N have been obtained with three different lattice parameters for Fe, Cr and Ni and large disorder. Further, no nitride precipitates could be detected by XRD. Therefore, we interpret the S phase as being heterogeneous, where Cr and Ni form coherent domains in the Fe₄N-like matrix. The orientation of these domains (along {100} planes, like in *fcc* ASS or along {111}, like in Fe₄N) and the possibility to control it by changing the nitriding conditions (saturation and decomposition rates) remains to be identified.

5 N diffusion anisotropy in ASS

Nitrogen diffusion in ASS comes along with a number of puzzling dependencies, as described in section 2.5.3. Several models have been proposed to explain nitrogen diffusion in ASS. Irrespective of their ability to reproduce the shape or even fit the nitrogen depth profiles, the models described in section 2.5.3 cannot explain the dependence of the diffusivity on the crystalline orientation, the ion energy and the ion current density.

Also these models assume that nitrogen diffusion occurs in a single phase, while the results of the previous Chapter suggest that the S phase is not homogeneous — Cr and Ni form domains in the Fe₄N-like matrix. Therefore, a comprehensive nitriding model must consider the inhomogeneous structure of the material. The presence of domains, which form along certain directions in cubic crystals, can short-circuit diffusion paths and also diffusion anisotropy. As N diffusion in Cr is ~ 4 orders of magnitude lower than in ASS, such zones would act like barriers for diffusing N. It was discussed that zones could form along $\{001\}$ or $\{111\}$ planes. Depending on the preferred orientation of CrN zones, nitrogen diffusivity would be faster either in (001) or (111) oriented grains, respectively.

In the following Chapter the effect of the nitriding process parameters on the N diffusion is investigated to reveal the diffusion mechanisms in the light of the findings of the preceding Chapter. For this purpose, single crystalline ASS samples were extensively employed. Different crystal orientations, implantation temperatures, energies and fluxes were used. In sections 5.2 and 5.3 the dependence of the N diffusivity on the orientation and temperature is investigated. Section 5.4 presents the results on the influence of ion energy and flux on the N diffusivity. The results are discussed in section 5.5 and summarized in section 5.6.

5.1 Experimental

ASS AISI 316L single crystals with (001), (110) and (111) orientations were ion-beam nitrided at otherwise identical conditions. An AISI 316L polycrystalline sample was used for a comparison. Standard parameters for ion energy and current density were 1 keV and 0.5 mA cm⁻², respectively, the later corresponding to an ion flux of 4.84×10^{15} atom cm⁻²

s^{-1} . The nitriding temperature was varied between 370 and 430°C. The nitriding time was 60 min, corresponding to a fluence of $1.74 \times 10^{19} \text{ cm}^{-2}$. To investigate the diffusion without ion bombardment, three single crystals with different orientations nitrided at 400°C were subsequently annealed *ex situ* at 400°C for 30 min.

In order to study the N diffusion dependence on the ion energy and current density, the samples were ion beam nitrided at energies of 0.5, 1 and 1.2 keV, and ion current densities of 0.3, 0.5 and 0.7 mA cm^{-2} , which corresponds to 2.90×10^{15} , 4.84×10^{15} and $6.77 \times 10^{15} \text{ atom cm}^{-2} \text{ s}^{-1}$, respectively. The nitriding was carried out at five temperatures in the range of 370 – 430°C. The nitriding time was 100, 60 and 43 min for ion current densities of 0.3, 0.5 and 0.7 mA cm^{-2} , respectively, corresponding to a constant fluence of $1.74 \times 10^{19} \text{ cm}^{-2}$.

The structure of the modified surface layer on the nitrided (1 keV, 0.5 mA cm^{-2} , 1 h, 400°C) and subsequently annealed (0.5 h, 400°C) polycrystalline samples was characterized by XRD. Bragg-Brentano and fixed incidence (1°) geometries were used. The nitrogen depth profiles were determined by NRA and ERDA. The trapping-detrapping model has been used to extract the diffusion coefficients.

5.2 N diffusion dependence on the crystal orientation

5.2.1 Phase structure

Fig. 5.1 shows X-ray diffraction patterns from virgin, as-nitrided (1 keV, 0.5 mA cm^{-2} , 400°C) and thermally annealed polycrystalline samples. A strong (111) texture can be seen from the diffractogram of the virgin sample. Broad diffraction peaks labeled by S, which correspond to the nitrogen expanded austenite, can be seen together with the austenite reflections γ from the underlying austenite. After annealing, the S phase diffraction peaks narrow and shift slightly towards higher angles. This may be attributed to the flattening of the nitrogen concentration profiles and a correspondingly decreasing nitrogen atomic ratio due to inward diffusion [167], residual stress relaxation [168], or defect annealing [169]. It should be emphasized that any formation of chromium nitrides has not been detected. In fact, the XRD diffractograms are very similar to the ones shown in Fig. 4.1(b). Thus, it is concluded that a similar microstructure, as described in the previous Chapter, forms. The lattice parameter derived from interplanar spacing d_{111} is 3.6 Å for the unexpanded lattice and 3.81 Å for the nitrogen expanded lattice. After annealing the lattice parameter is 3.77 Å.

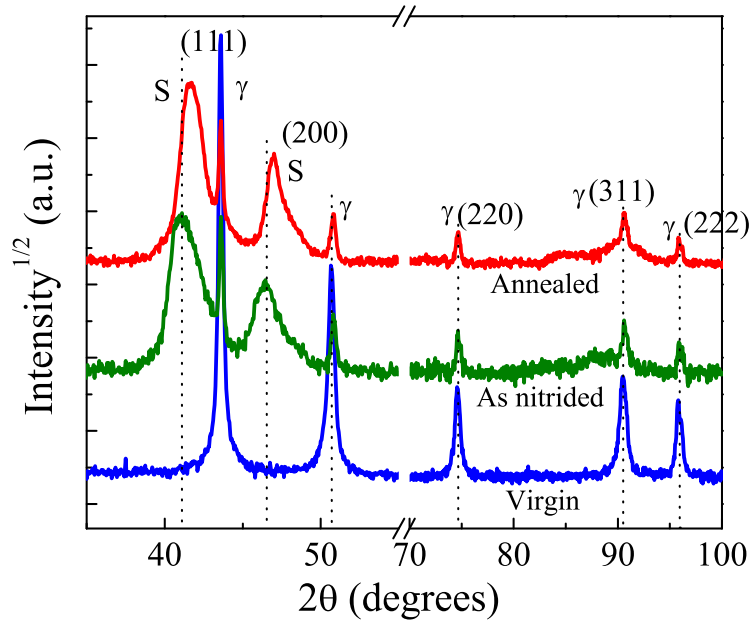


Figure 5.1: X-ray diffraction patterns of virgin, nitrided, and subsequently annealed polycrystalline samples obtained using Bragg-Brentano geometry [96].

5.2.2 Lattice rotation

During nitriding a lattice rotation takes place [52, 170]. Recently, a systematic investigation on the lattice rotation after nitriding up to 8 h was published [170]. It is shown that the rotation can be larger than 10° . The orientation of the single crystals before and after nitriding was obtained from the electron backscattered diffraction measurements in a way described in Ref. [170]. The probed depth is $\sim 0.1 \mu\text{m}$ and the uncertainty of the orientation is $\sim 0.7^\circ$ before nitriding. The uncertainty of the orientation measurement after the ion beam nitriding due to the surface roughness is larger but does not exceed 2° . Fig. 5.2 presents the rotation direction of three single crystals after nitriding for 1 h at 400°C with 1 keV and 0.5 mA/cm^2 . The rotation angle is highest for the single crystal with the (110) orientation and is equal to 6° . It rotates towards the $\langle 111 \rangle$ pole. The single crystal with the (111) orientation also rotates to this pole by 5° . The (001) oriented single crystal rotates only by 2° . The rotations follow the tendency published in Ref. [170], except for the sample with the (001) orientation. The grains with the orientations close to the $\langle 001 \rangle$ pole were reported to rotate to this pole [170]. However, the rotation is small and in the range of the measurement error, thus, the direction might be incorrect. The lattice rotation decreases concomitantly with the nitrogen concentration [52]. This means that the average lattice rotation is lower than the measured value at the surface. Thus, the effect of the lattice rotation to the nitrogen penetration depth is small and can be

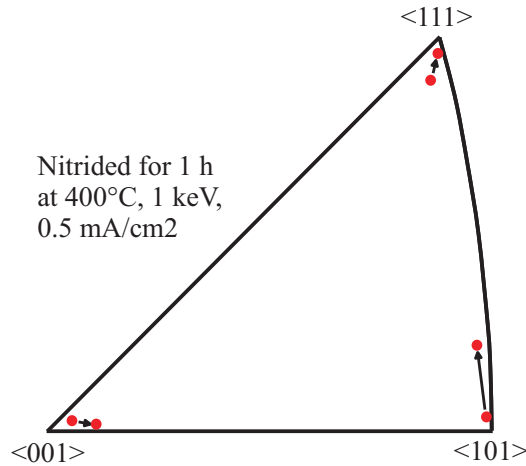


Figure 5.2: Inverse Pole figure showing the evolution of the orientation of single crystals before and after nitriding for 1 h at 400°C with 1 keV and 0.5 mA/cm². The arrows indicate rotation direction.

neglected in the nitrogen transport investigation described below.

5.2.3 Nitrogen depth profiles

The N depth profiles of the (001), (110) and (111) oriented single crystals and the polycrystalline sample, obtained after nitriding at 400°C for 60 min, are presented in Fig. 5.3(a). The profiles are fully reproducible, as the same depth profiles were obtained after nitriding of three different samples at identical conditions for each orientation.

All N depth profiles exhibit a non-conventional diffusion shape as described in section 2.5.3. The nitrided depth X_N is defined here as the length of the quasi-linear part, which corresponds to a layer that contains about 90% of the total amount of retained nitrogen. The scattering in the quasi-linear part is of the statistical nature.

There are significant differences in the nitrogen penetration depths for the different crystal orientations, with a maximum of 1.5 μm , an intermediate result of 0.95 μm , and a minimum of 0.7 μm for (001), (110) and (111), respectively. This sequence is consistent with the previous results on AISI 304L [171], AISI 316L [89] and Inconel 690 [51]. The observed differences in penetration depths cannot be explained by the differences in sputtering [96]. The variation of the respective N surface concentration is about 27, 24, and 23 at% for the (001), (011), (111) orientations, respectively. It should be mentioned that NRA is not a surface sensitive technique, so the near-surface concentration can only be extrapolated from the quasi-linear part of the profiles (see also Fig. 5.5). However, ERDA measurements indeed show that N concentration slope in the first few hundred nanometers is linear (Fig. 5.3(b)-(d)). The N surface concentration is about 32, 29, and

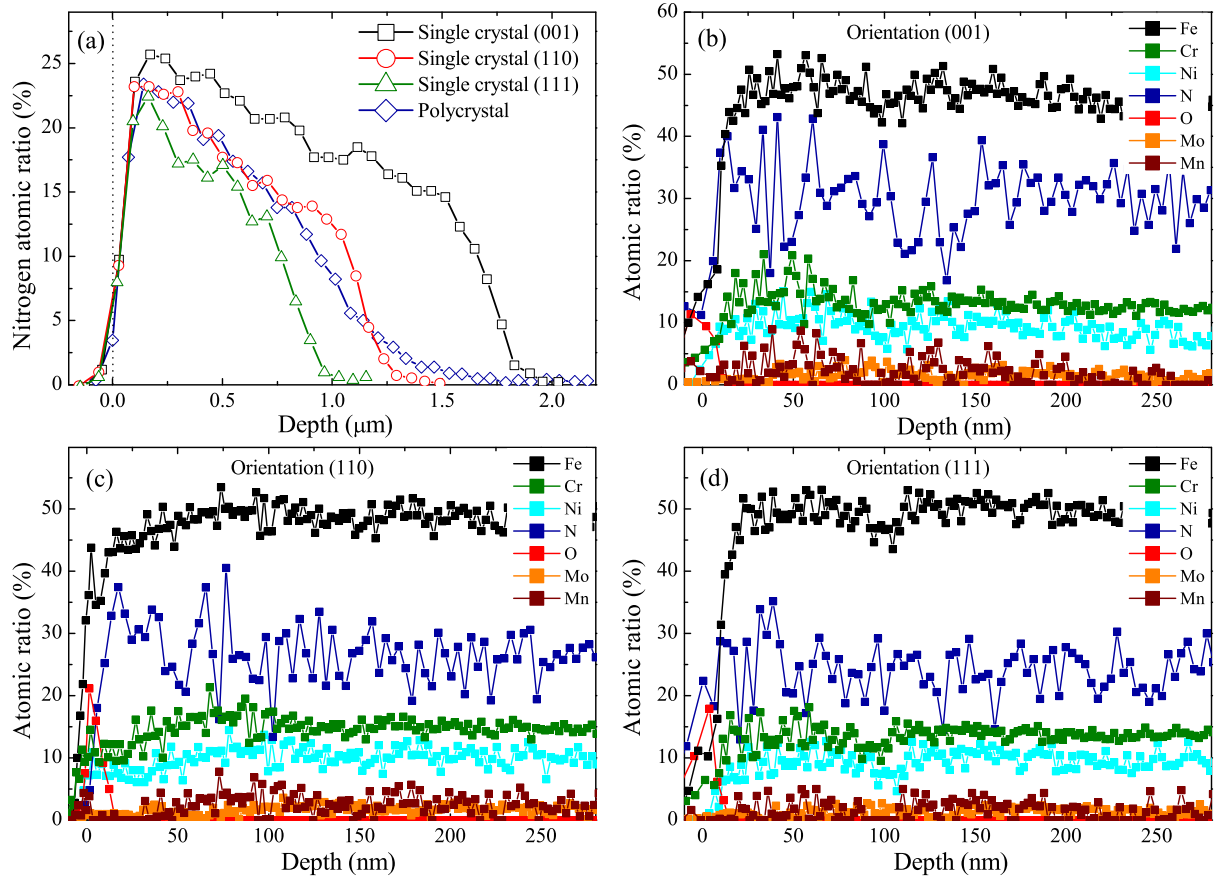


Figure 5.3: (a) NRA nitrogen distribution profiles of nitrated single crystals with orientations (001), (110), and (111), and of a polycrystalline sample [96]. ERDA depth profiles of nitrated single crystals with (b) (001), (c) (110), and (d) (111) orientations.

26 at% for the (001), (011), (111) orientations, respectively. The values agree well with the NRA results.

As indicated in Fig. 5.1, the polycrystalline sample exhibits a pronounced (111) texture. The nitrogen concentration in the quasi-linear part of the polycrystalline samples is close to the one of the (111) sample, but the leading edge is less sharp compared to the single crystals (see Fig. 5.3(a)). This can be attributed to a superposition of the depth profiles in differently oriented grains of the polycrystal [51, 55] with the strongest contribution arising from (111) grains due to the texture.

Fig. 5.4 compares the N depth profiles of as-nitrated and thermally annealed single crystals and a polycrystalline sample. After thermal annealing, the nitrogen loss was calculated by integrating the N concentration depth profiles resulting in less than 2%, which is within the measurement error. Thus, an oxide layer, formed after exposure to air, apparently prevents nitrogen out-diffusion. However, the nitrogen profiles flatten

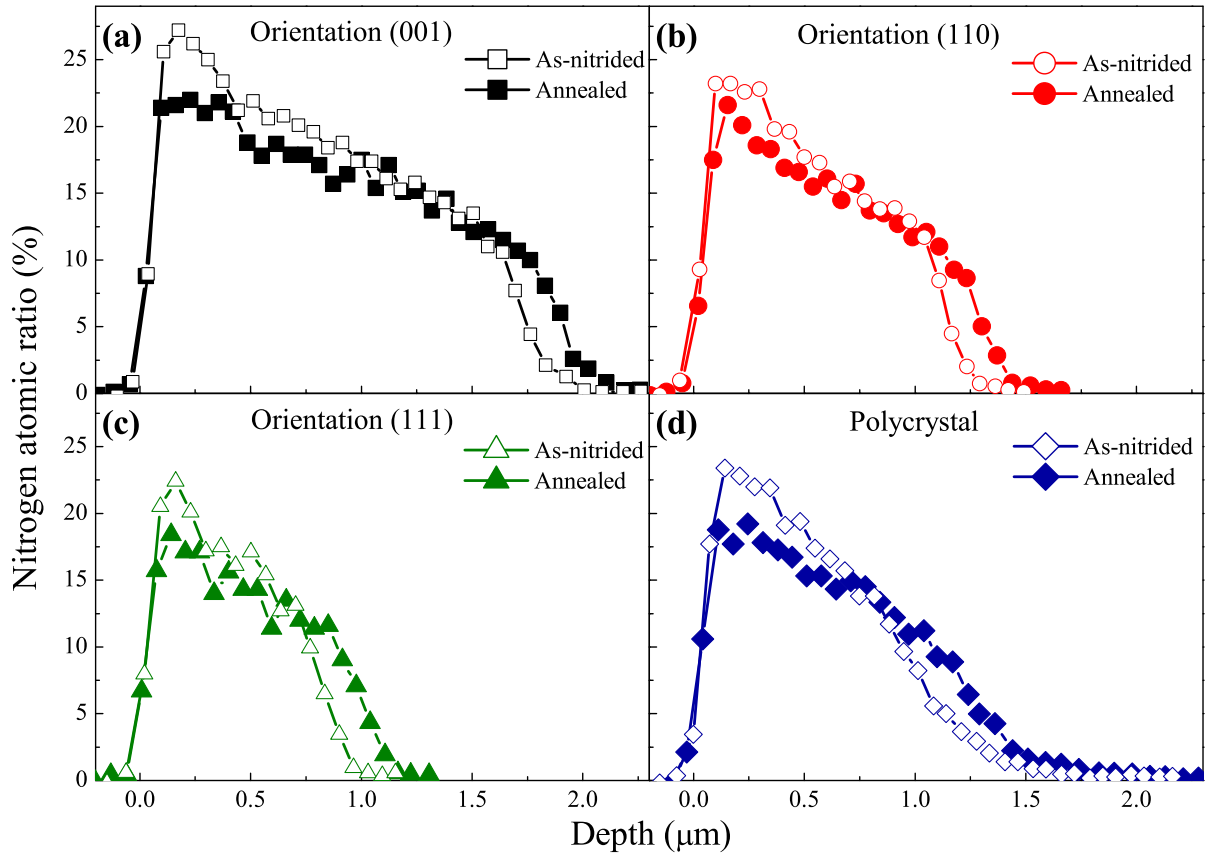


Figure 5.4: Comparison of NRA nitrogen distribution profiles of nitrided single crystals with orientations (a) (001), (b) (011), (c) and (111), and (d) of a polycrystalline sample with nitrogen distribution profiles after subsequent thermal annealing.

during thermal annealing with the near surface concentration slightly decreasing and the nitrogen penetration depth increasing. The difference in penetration depth in the leading edge between the as-nitrided and annealed samples appears to be similar. This indicates that the diffusivity during thermal annealing is similar for all orientations.

5.2.4 Fitting of the experimental profiles

Despite the fact that the S phase cannot be considered as a single phase, Cr and Ni precipitates are very small and likely distributed homogeneously. Thus, the trapping-detrapping model can still be applied. However, as the model does not take into account the microstructure, the diffusion coefficient should be regarded as an effective one.

The calculated and experimental profiles are compared in Fig. 5.5. The D values extracted from the fits are given in Table 5.1. A very good agreement is obtained between the calculated and experimental depth profiles. The average of the D values is in agree-

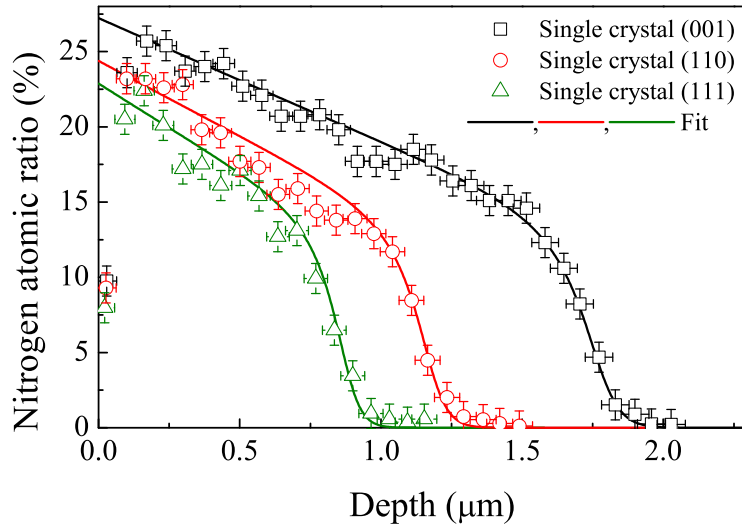


Figure 5.5: NRA nitrogen distribution profiles of nitrated single crystals with (001), (110), and (111) orientations [96]. The lines are from calculations according to Eqs. (3.9)-(3.11).

ment with the results obtained for polycrystalline AISI 304L steel [50]. The calculations show that the diffusion coefficient varies by a factor of two between (001) and (111) orientations.

The calculated and experimental nitrogen depth profiles of annealed samples are shown in Fig. 5.6(a). In contrast to the fits for the as-nitrated samples, the diffusion coefficients during annealing are independent of the orientation and significantly lower. The dotted lines represent calculations using the diffusion coefficient deduced from the nitriding stage (Fig. 5.6(b)). This demonstrates that the nitrogen diffusion during nitriding is

Table 5.1: Sputtering rates (V_s), coefficients κ (see Eq. (3.12)), and diffusion coefficients (D), obtained from the fitting, for as-nitrated and annealed samples. The errors are evaluated by χ^2 method described in Section 3.5.3.

Sample orientation	V_s ($\times 10^{-8}$ cm/s)	κ ($\times 10^{-15}$ cm ²)	D ($\times 10^{-12}$ cm ² /s)
As-nitrated			
(001)	1.4	1.3	7.9 ± 0.007
(110)	1.7	1.5	4.8 ± 0.012
(111)	1.8	1.7	3.8 ± 0.009
Isothermally annealed			
(001)	—	—	1.8 ± 0.015
(110)	—	—	1.5 ± 0.011
(111)	—	—	1.5 ± 0.013

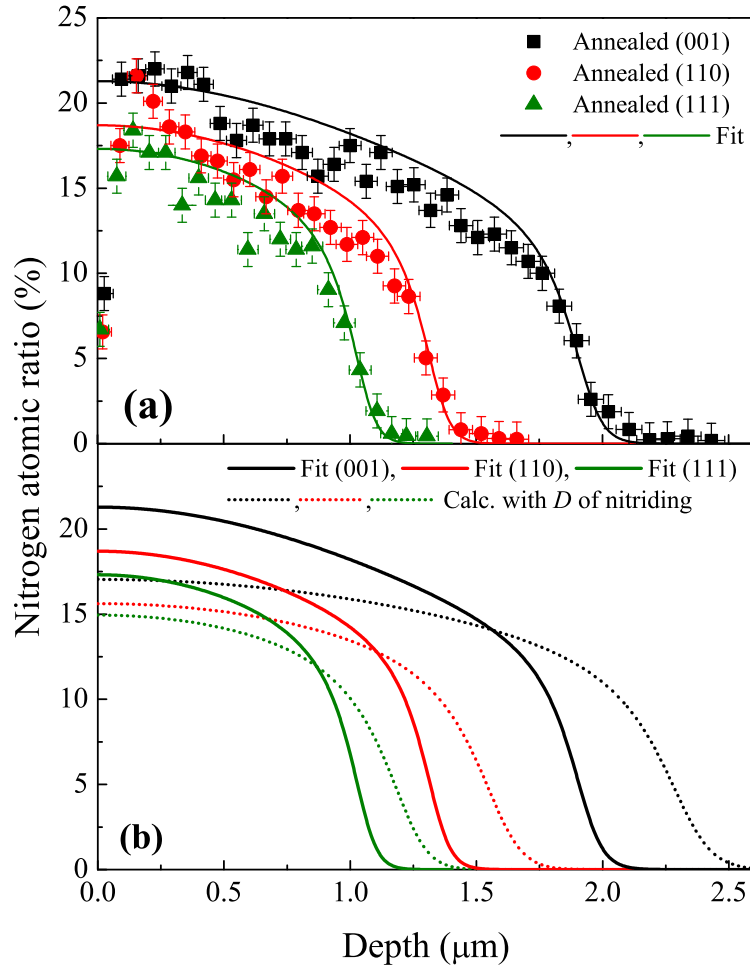


Figure 5.6: (a) NRA nitrogen distribution profiles of annealed single crystals with (001), (110), and (111) orientations and fits according to Eqs. (3.9)-(3.11). (b) is a comparison with the profiles which would be expected using the diffusion coefficient obtained from the nitriding stage (dotted lines).

significantly enhanced over thermal diffusion and it is anisotropic during nitriding while being isotropic during thermal annealing.

In summary, N depth profiles exhibit a non-conventional diffusion shape, which consists of the quasi-linear part and the leading edge. The leading edge is very sharp compared to polycrystalline samples, and is consistent with the trapping-detrapping model. The nitrogen penetration depth strongly depends on the orientation of the single crystal, and is largest, intermediate and lowest at (001), (110) and (111) orientation, respectively. The diffusion coefficient is higher by a factor of 2 for the (001) orientation in relation to the (111) orientation. The diffusivity during post-nitriding thermal annealing is significantly lower than that during ion beam nitriding and is independent on the crystalline orienta-

tion. The diffusion coefficient decreases by a factor of 4.3, 3.3 and 2.5 for the orientations (001), (110) and (111), respectively.

5.3 Nitrogen diffusion: Dependence on the temperature

Experimental and calculated N depth profiles from (001), (110) and (111) oriented single crystals nitrided at different temperatures are presented in Fig. 5.7. As expected, the increase in temperature results in the increase of the nitrogen penetration depth without significant changes in the near-surface concentration. The N diffusion shows an orientation dependence in the whole temperature range in the order $D_{(001)} > D_{(110)} > D_{(111)}$.

The Arrhenius plot is presented in Fig. 5.7(d). The results were fitted with a line. The offset and the slope of Arrhenius plots have been used to extract E and D_0 which are collected in Table 5.2. E is essentially the same for the (110) and (111) orientations, and higher for the (001) orientation. On the other hand, D_0 depends strongly on the orientation. Moreover, D_0 increases by two orders of magnitude between the (111) and (001) orientations. For comparison, D values of the (001) orientations are fitted with the E value from the (111) orientation. The fit deviates at both ends from data points significantly. Even in this case the D_0 value is two times larger than for the (111) orientation. Such surprisingly large differences indicate that the observed N diffusion anisotropy effects cannot be associated with the differences in activation energy.

D_0 is associated with the entropy change ΔS as expressed in Eq. (2.7). The obtained ΔS values are presented in Table 5.2. The used lattice parameters, obtained by glancing angle (1° of incidence) X-ray diffraction measurement of polycrystalline sample nitrided at 400°C , are 3.94 \AA for (001) and 3.90 \AA for the (011) and (111) orientations. The estimated X-ray penetration depth is $\sim 0.2 \text{ \mu m}$.

Huntington et al. [172] showed that the entropy contribution comes from three spatial regions: the atoms in the immediate neighborhood of the defect, the region over which the defect sets up an elastic stress field and, finally, the surface condition and its influence. The entropy change due to the surface condition always has the opposite sign to that in the neighborhood of the defect and generally makes only a small contribution. Owing to the local nature of the diffusion process, only the first two contributions will be considered here. Then the total entropy change can be expressed as a sum of a vibrational ΔS_v and

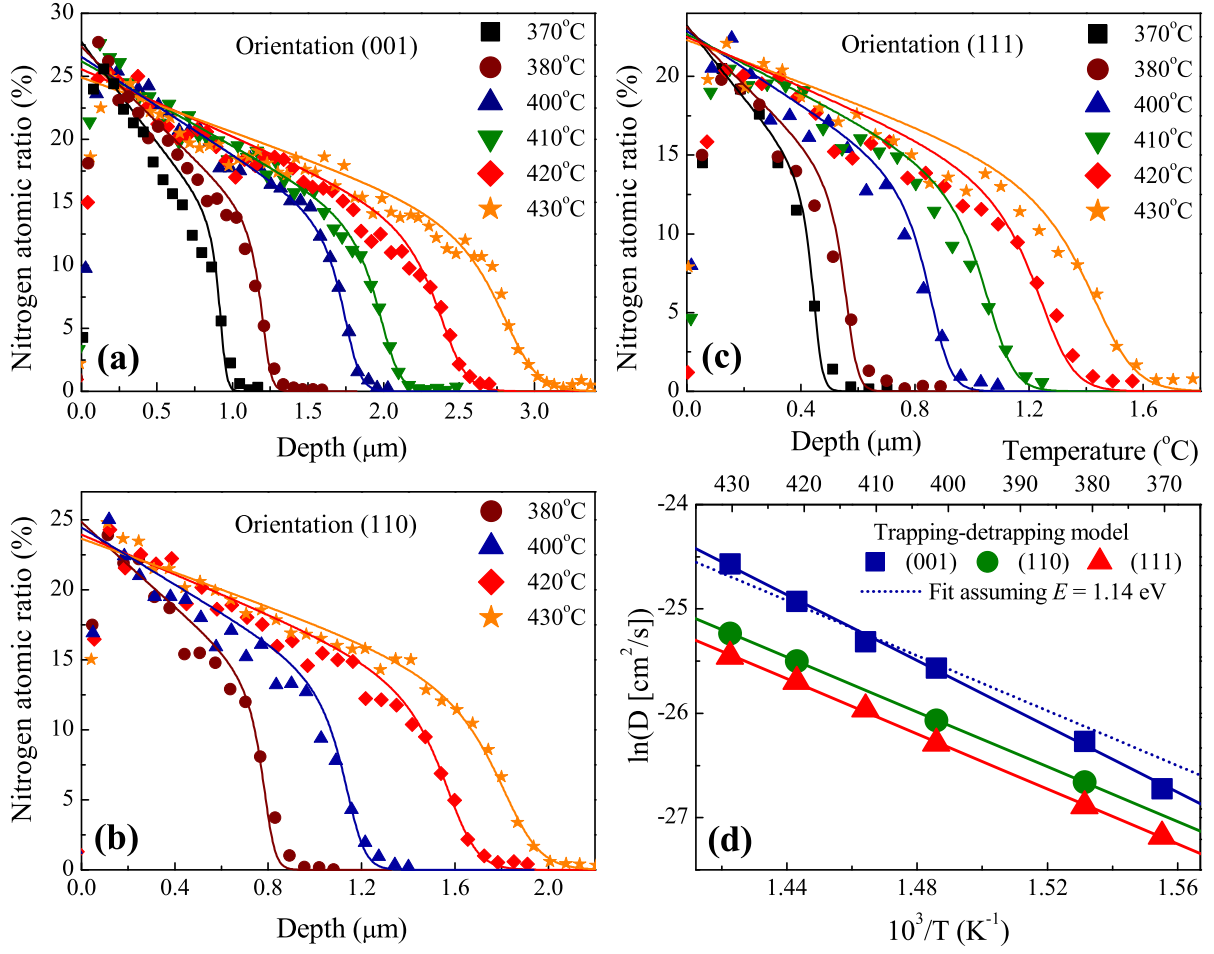


Figure 5.7: NRA nitrogen distribution profiles of nitrated single crystals with (a) (001), (b) (110) and (c) (111) orientation at different temperatures. The lines are from calculations according to Eqs. (3.9)-(3.11). The Arrhenius plot (d) for the (001), (110) and (111) orientations. The errors of the diffusion coefficients are smaller than dots. For comparison D values of the (001) orientation are fitted with the same E value as for the (111) orientation.

an elastic stress ΔS_s terms as [172, 173]

$$\Delta S = \Delta S_\nu + \Delta S_s = -nk \sum_i \ln \left(\frac{\nu'_i}{\nu_i} \right) - \lambda \Delta H_0 \frac{d(\mu/\mu_0)}{dT}, \quad (5.1)$$

where ν_i are the original frequencies for the lattice, ν'_i are the final frequencies with defects, n is the number of atoms forming the barrier, λ represents a fraction since only a portion of the work goes into straining the lattice, ΔH_0 is the activation enthalpy, μ is the shear modulus, and the suffix 0 refers to the absolute zero temperature. As interstitial

atoms cause local crowding and the frequencies rise, ΔS_ν gives a negative contribution to the total entropy change [65]. Since $d(\mu/\mu_0)/dT$ is negative for ASS, ΔS_s is positive.

A nitrogen atom jumping from one octahedral position to another one can take a direct path, or it can move via a tetrahedral position. It was reported in the literature [174,175] and discussed in section 5.5 that the path via a tetrahedral position is more favorable. For the path via a tetrahedral position $n = 6$ if only the barrier atoms are affected. The value of ν'_i/ν_i is taken equal to 2.3 as it yields reasonable $d(\mu/\mu_0)/dT$ values for (110) and (111) orientations. The factor λ can be assumed to be equal to 0.5 [173]. ΔH_0 is of the order of the activation enthalpy for diffusion, $\Delta H_0 \approx E$. The calculated $\Delta S_\nu/k$, $\Delta S_s/k$ and $d(\mu/\mu_0)/dT$ are presented in Table 5.2. For non-nitrided ASS, the literature shows $d(\mu/\mu_0)/dT \approx -0.00048$, -0.00037 and -0.00039 K^{-1} for (001), (011) and (111) orientations, respectively [176]. The calculated $d(\mu/\mu_0)/dT$ values with $E = 1.14 \text{ eV}$ are similar to the values of non-nitrided ASS for all orientations, however, the value calculated with $E = 1.36 \text{ eV}$ is more than two times lower for the (001) orientation. This suggests that in the (001) orientation the environment for N diffusion is different as compared to the other orientations.

In summary, the obtained D_0 values vary by two orders of magnitude in the order $D_{0,(001)} > D_{0,(011)} > D_{0,(111)}$, while E is almost the same for the (111) and (110) orientations and higher for the (100) orientation. The calculated ΔS values also depend on the orientation. The attempt to express ΔS as a sum of the vibrational ΔS_ν and the elastic stress ΔS_s terms results in a large discrepancy for the (001) orientation. This is probably

Table 5.2: Diffusion activation energies (E), pre-exponential coefficients (D_0), total entropy changes ($\Delta S/k$), entropy changes in the immediate neighborhood of the defect ($\Delta S_\nu/k$) and entropy changes due to elastic stress ($\Delta S_s/k$), divided by Boltzmann constant, and variation of shear modulus with temperature ($d(\mu/\mu_0)/dT$) for the (001), (011) and (111) orientations. The uncertainties correspond to the linear fits of the experimental data.

Orientation	E (eV)	D_0 (cm^2/s)	$\frac{\Delta S}{k}$	$\frac{\Delta S_\nu}{k}$	$\frac{\Delta S_s}{k}$	$\frac{d(\mu/\mu_0)}{dT}$ (K^{-1})
<i>Trapping-detraping model</i>						
(001)	1.36 ± 0.003	$(1.2 \pm 0.1) \times 10^{-1}$	2.0	-5	7.0	-8.9×10^{-4}
(001)*	1.14	2.4×10^{-3}	-1.8	-5	3.2	-4.8×10^{-4}
(110)	1.13 ± 0.004	$(1.4 \pm 0.2) \times 10^{-3}$	-2.4	-5	2.6	-4.0×10^{-4}
(111)	1.14 ± 0.005	$(1.2 \pm 0.2) \times 10^{-3}$	-2.5	-5	2.5	-3.8×10^{-4}

*Fit with the same E as for the (111) orientation

because of a different N diffusion environment in this orientation compared to the other orientations.

5.4 Influence of ion flux and energy on N diffusion

The experimental and calculated N depth profiles of single crystals with (001) and (111) orientations nitrided at 400°C with three different ion current but the same fluence densities are presented in Fig. 5.8. The steady-state near surface nitrogen concentration does not depend on the flux, at ~ 28 at% and ~ 22 at% for (001) and (111) orientations, respectively. The observed independence of the surface concentration on the flux is within the uncertainty of NRA (2 at%) at the surface. The retained nitrogen amount and the thickness of the nitrided layer are highest for the lowest ion current density for both orientations (see Tables 5.3 and 5.4). Note that for the lowest current density the longest nitriding time was used. Fig. 5.9 shows N depth profiles of single crystals with (001) orientation nitrided at 370, 400 and 430°C with 1 keV and ion current densities of 0.3 and 0.7 mA cm⁻². The same N penetration depth dependence is also observed for the nitriding temperatures of 370 and 430°C.

The profiles were fitted by trapping-detrapping model and the results for the (001) orientation are shown in Table 5.3. For the (111) orientation the results are summarized in Table 5.4. The obtained diffusion coefficient depends on the flux. For the (001) orientation

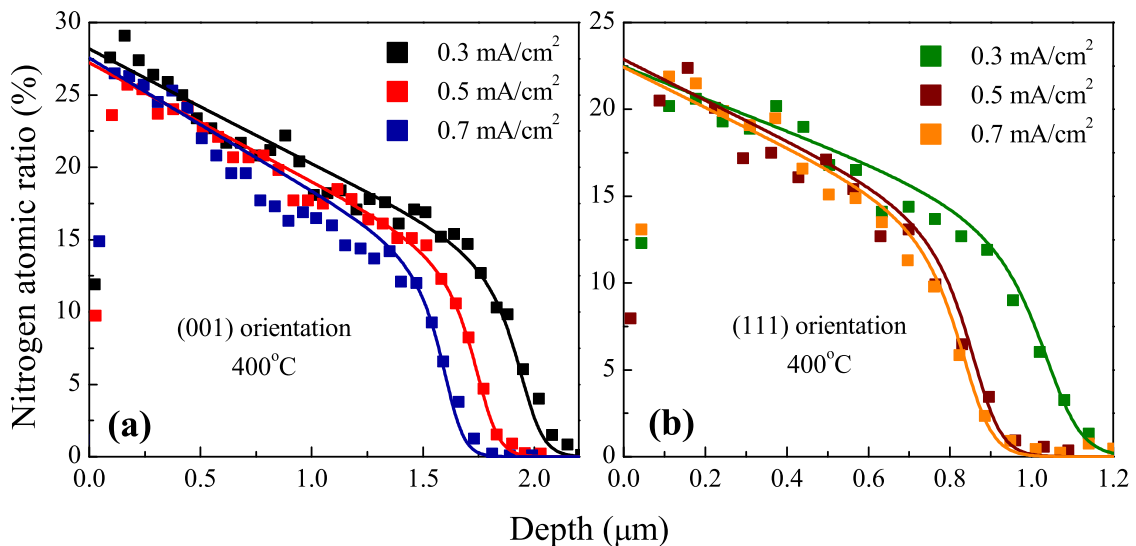


Figure 5.8: NRA nitrogen distribution profiles of the single crystals with (a) (001) and (b) (111) orientations nitrided at 400°C with 1 keV and three ion current densities. The lines are calculations from according to Eqs. (3.9)-(3.11).

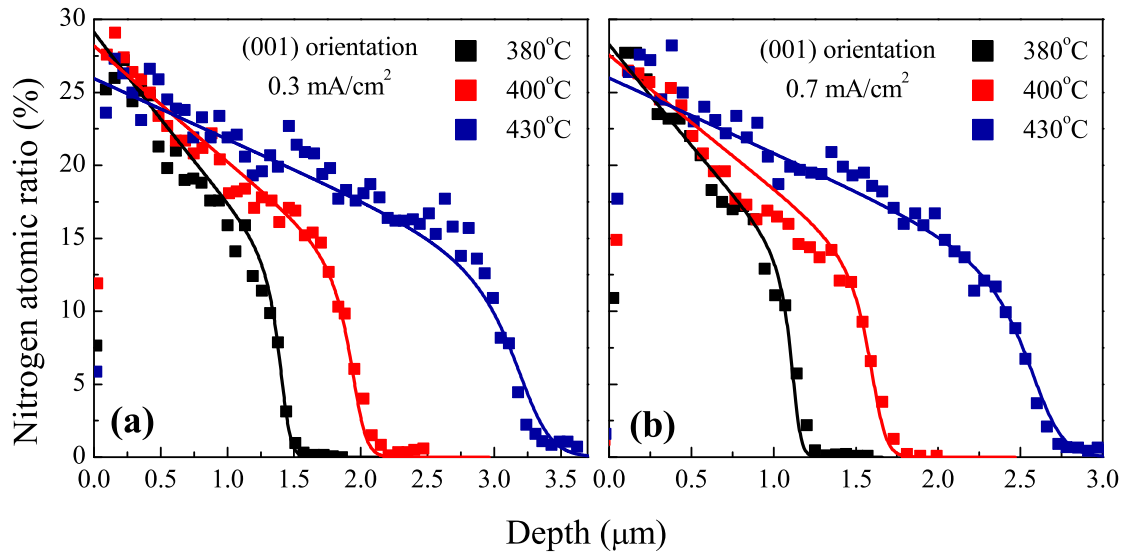


Figure 5.9: NRA nitrogen distribution profiles after nitriding single crystals with (001) orientation at 370, 400 and 430°C with 1 keV and ion current density of 0.3 mA cm^{-2} (a) and 0.7 mA cm^{-2} (b).

the diffusion coefficient is higher by a factor of $\sim 1.5 \pm 0.1$ for the highest ion current density used in relation with the lowest in the whole temperature range. For the (111) orientation the ratio is ~ 1.7 .

The experimental and calculated N depth profiles of single crystals with the (001) and

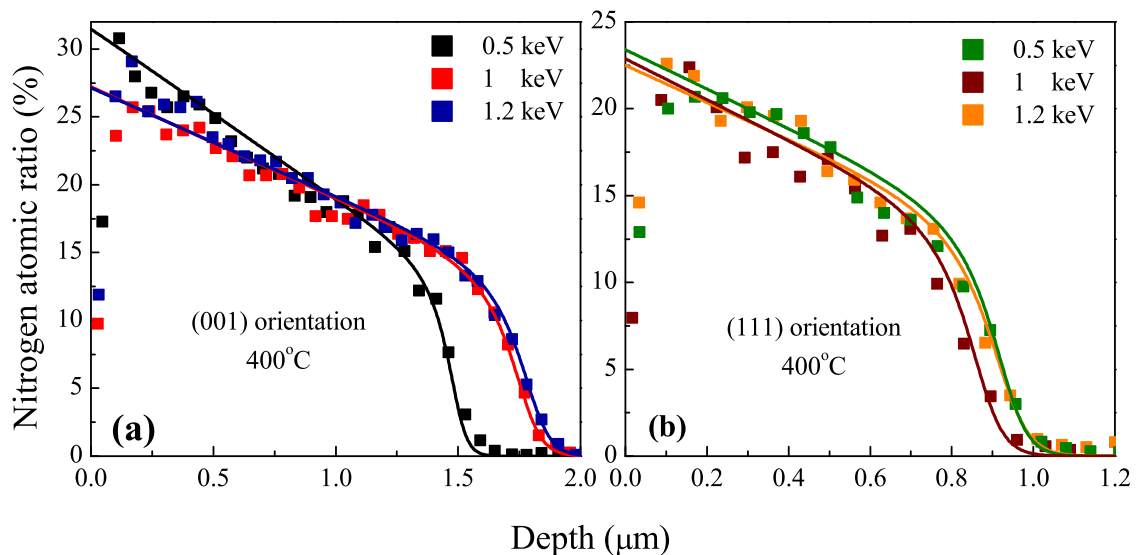


Figure 5.10: NRA nitrogen distribution profiles of the single crystals with (a) (001) and (b) (111) orientations nitrided at 400°C with 0.5 mA cm^{-2} and three ion energies.

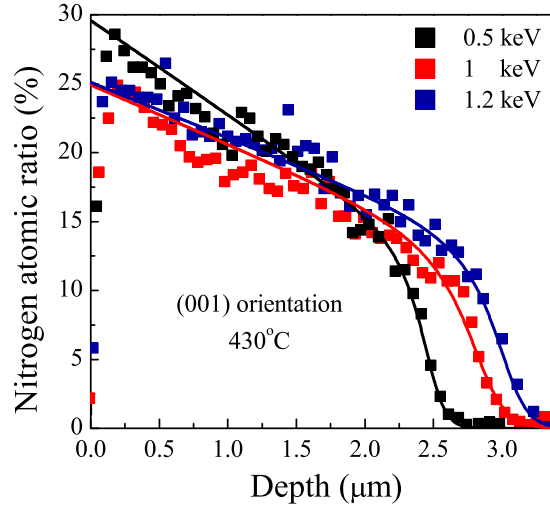


Figure 5.11: NRA nitrogen distribution profiles of the single crystals with (001) orientation nitrided at 430°C with 0.5 mA cm^{-2} and three ion energies.

(111) orientations nitrided at 400°C with three different ion energies are presented in Fig. 5.10. The near surface concentration is approximately equal to 27 at% after nitriding with 1 and 1.2 keV, and ~ 31 at% after nitriding with 0.5 keV, for the (001) orientation. For the (111) orientation the near surface concentration is the same for all implantation energies at ~ 23 at% within the uncertainty of NRA. The retained nitrogen amount is highest for the highest implantation energy for both orientations (see Tables 5.3 and 5.4).

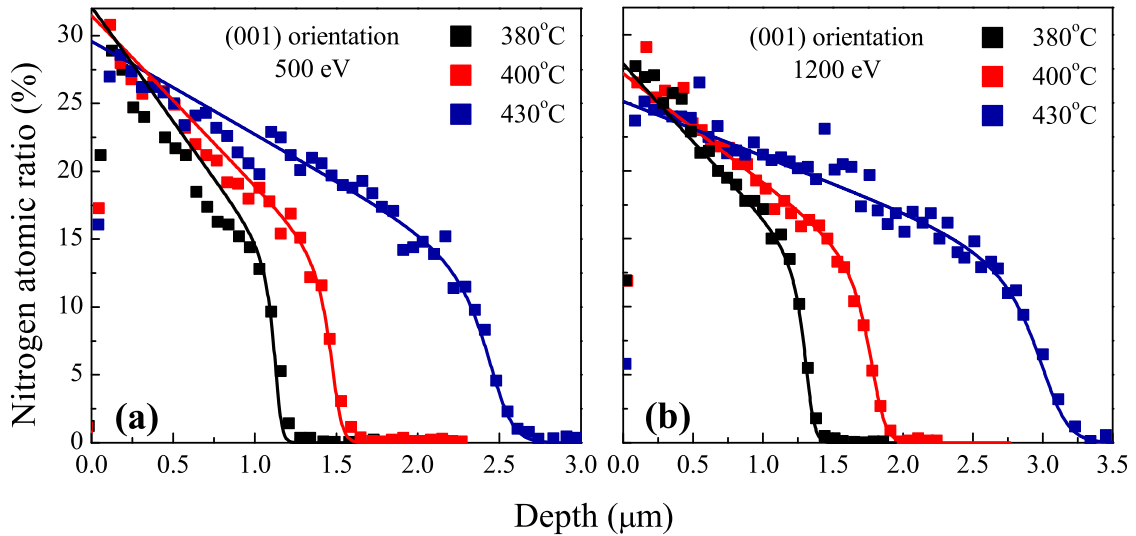


Figure 5.12: NRA nitrogen distribution profiles after nitriding single crystals with (001) orientation at 370, 400 and 430°C with 0.5 mA cm^{-2} and ion energies of 500 eV (a) and 1200 eV (b).

Table 5.3: Sputtering rates (V_s), coefficients κ , retained nitrogen amounts (Φ_{ret}/Φ) after nitriding at 400°C, and diffusion coefficients (D) for three fluxes and energies of the samples with (001) orientation.

Experimental conditions	V_s ($\times 10^{-8}$ cm/s)	κ ($\times 10^{-15}$ cm ²)	Φ_{ret}/Φ (%)	D ($\times 10^{-12}$ cm ² /s)		
				380°C	400°C	430°C
Constant ion energy of 1 keV						
0.3 mA/cm ²	1.0	1.1	20.7	2.9	5.6	16.1
0.5 mA/cm ²	1.7	1.3	17.1	3.9	7.9	21.4
0.7 mA/cm ²	1.8	1.3	15.6	4.5	8.8	23.3
Constant flux of 0.5 mA/cm ²						
0.5 keV	0.4	1.1	16.4	1.9	3.3	10.1
1.0 keV	1.7	1.3	17.1	3.9	7.9	21.4
1.2 keV	2.3	1.7	18.6	4.5	9.0	25.0

The thickness of the nitrided layer is lowest after nitriding with 0.5 keV for the (001) orientation and increases with the implantation energy. Nitriding with 1 and 1.2 keV at 400°C results in almost the same nitrided layer thickness. At 430°C the nitrogen diffusion is faster and the implantation energy effect is more pronounced. As shown in Fig. 5.11, the nitrided layer thickness is higher for 1.2 keV than for 1 keV. For the (111) orientation, the nitrogen penetration depth is the same for all three nitriding energies. However, as the sputtering rate increases with the energy (see Table 5.3), a higher or equal nitrogen penetration depth indicates faster diffusion at higher implantation energies. This is also confirmed by the fitting. The results for the (001) orientation are shown in Table 5.3. For the (111) orientation the results are summarized in Table 5.4. For the (001) orientation

Table 5.4: Sputtering rates (V_s), coefficients κ , retained nitrogen amounts (Φ_{ret}/Φ), and diffusion coefficients (D) for three fluxes and energies of the samples with (111) orientation.

Experimental conditions	V_s ($\times 10^{-8}$ cm/s)	κ ($\times 10^{-15}$ cm ²)	Φ_{ret}/Φ (%)	D ($\times 10^{-12}$ cm ² /s)	
Constant ion energy of 1 keV					
0.3 mA/cm ²	1.3	1.7	8.4	3.5	
0.5 mA/cm ²	1.8	1.7	7.1	3.8	
0.7 mA/cm ²	3.0	1.7	6.7	6.0	
Constant flux of 0.5 mA/cm ²					
0.5 keV	1.3	1.7	7.7	3.0	
1.0 keV	1.8	1.7	7.1	3.8	
1.2 keV	2.3	1.7	7.9	5.0	

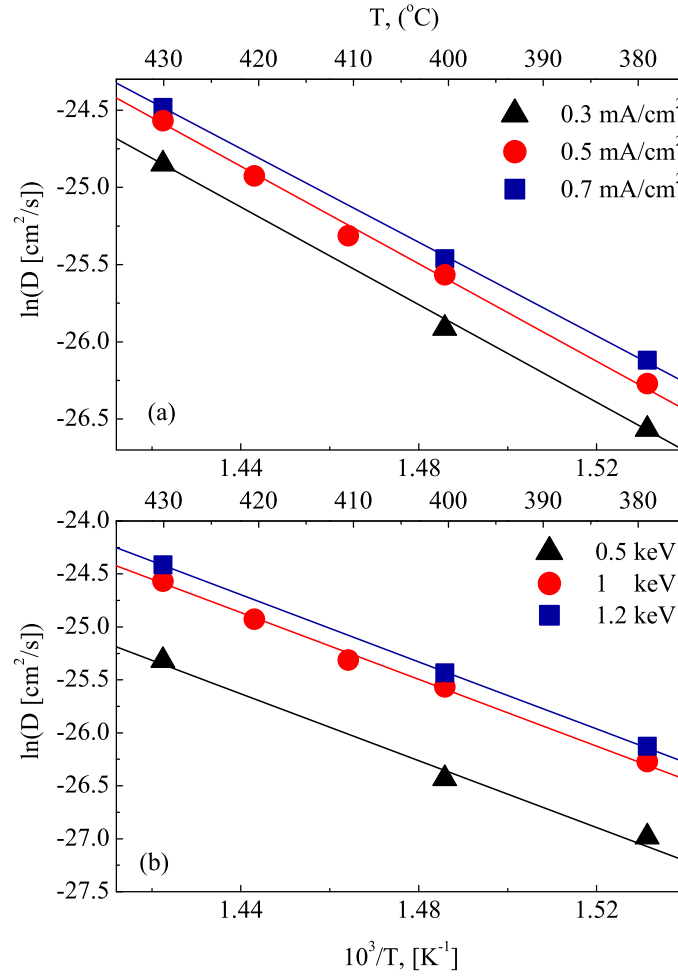


Figure 5.13: The Arrhenius plots for three (a) ion current densities and (b) energies for the (001) orientation. The errors of the diffusion coefficients are smaller than the dots.

the diffusion coefficient is higher by a factor of 2.4, 2.7 and 2.5 for the highest *vs* the lowest implantation energy for nitriding temperatures 370, 400 and 430 $^\circ\text{C}$, respectively. For the (111) orientation this ratio is ~ 1.7 .

The Arrhenius plot (Fig. 5.13) was used to extract a diffusion pre-exponent factor D_0 and an activation energy E . The extracted E and D_0 are given in Table 5.5. The same activation energy is obtained for the ion current densities of 0.3 and 0.5 mA/cm^2 . D_0 is slightly lower for the ion current density of 0.3 mA/cm^2 as compared to 0.5 mA/cm^2 . However, a relatively large error makes this difference insignificant. A lower activation energy and the lowest D_0 value are obtained for the ion current density of 0.7 mA/cm^2 . It should be noted that the diffusion coefficient at a given temperature is higher for a higher ion current density. This result is explained by the prevalence of the exponential term as a reduced activation energy is obtained for the ion current density of 0.7 mA/cm^2 . For

Table 5.5: Diffusion activation energies (E), pre-exponential coefficients (D_0) for three fluxes and energies for the (001) orientation. The uncertainties correspond to the linear fits of the experimental data.

Experimental conditions	E (eV)	D_0 (cm ² /s)
Constant ion energy of 1 keV		
0.3 mA/cm ²	1.36 ± 0.005	$(9.3 \pm 1.5) \times 10^{-2}$
0.5 mA/cm ²	1.36 ± 0.003	$(1.2 \pm 0.1) \times 10^{-1}$
0.7 mA/cm ²	1.31 ± 0.003	$(5.4 \pm 0.5) \times 10^{-2}$
Constant flux of 0.5 mA/cm ²		
0.5 keV	1.36 ± 0.003	$(5.5 \pm 0.6) \times 10^{-2}$
1.0 keV	1.36 ± 0.003	$(1.2 \pm 0.1) \times 10^{-1}$
1.2 keV	1.37 ± 0.002	$(1.5 \pm 0.1) \times 10^{-1}$

different N implantation energies almost the same activation energies are obtained while D_0 increases linearly with the implantation energy.

In summary, the nitrogen diffusivity increases with the increasing ion current density and ion energy. The calculated diffusion coefficient for each temperature is larger for the flux of 0.7 mA/cm² as compared to 0.3 mA/cm² by a factor of ~ 1.5 and ~ 1.7 for the (001) and (111) orientations, respectively. The difference in the diffusion coefficient between 1.2 and 0.5 keV for each temperature is ~ 2.5 and ~ 1.6 for the (001) and (111) orientations, respectively. Nitriding of the sample with the (001) orientation at different temperatures shows that the diffusion activation energy is almost independent on the implantation energy or current density. The diffusion pre-exponential factor increases by ~ 2.7 , when ion energy increases from 0.5 to 1.2 keV. No clear D_0 tendency on the ion current density could be observed. Except if it is accepted that E is almost constant so that D_0 increases.

5.5 Discussion

The results of section 5.2 show two major phenomena: nitrogen enhanced diffusion and induced anisotropy during nitriding. The first one is related to the observation that the nitrogen diffusion coefficient is significantly higher during nitriding than during thermal annealing. The second one is related to the observation that nitrogen diffusion is dependent on the orientation of the single crystals only during ion beam nitriding but not during subsequent annealing. As it was mentioned above, the difference in penetration depths cannot be explained by variation of the sputtering rate, as the difference in the sputtering

depth between the (001) and (111) orientations is only $0.16 \mu\text{m}$, while the difference in the corresponding penetration depths is $0.8 \mu\text{m}$. However, different sputtering rates result in different surface concentrations. The difference is ~ 2 at% between the (111) and (110) samples, and of similar magnitude between the (110) and (001) samples. Considering the possibility of concentration dependent diffusion coefficient, a higher surface concentration might lead to a higher overall diffusivity, thus resulting in deeper penetration depths. However, the diffusivity is independent on the orientation during annealing regardless of the difference in surface concentrations. The nitrogen concentration is practically the same for all three ion current densities (Fig. 5.8). It is even higher after nitriding with 0.5 keV , as compared to the other two (Fig. 5.10). Also in this work, a very good agreement between experimental and calculated results is obtained without any concentration dependence of the diffusivity. Apparently, the irradiation enhancement of the diffusion induced by energetic ions is far more pronounced than the concentration effects which are known from gas nitriding. This is consistent with the possibility to achieve a significantly larger variation of the surface concentration during gas nitriding [33], whereas ion nitriding always results in a comparatively high surface concentration through the balance between implantation and sputtering [117].

Further, an anisotropic dependence of the strain on the stress was proposed to explain anisotropic lattice expansion [114] and thickness variation of the nitrided layer [51]. It was suggested that the anisotropic charge density redistribution under strain could cause a variation of the diffusion coefficient along different lattice directions [114]. As the nitrided layer is fixed to the bulk of the single crystal, it can expand only in normal direction. Due to the increased distance of the lattice planes, which are parallel to the surface, the diffusion barrier through these planes should become slightly lower, as the influence of the nearest neighbors in normal direction becomes reduced. However, this stress model can not explain the flux effect [50], as there is no evident mechanism by which an increased flux could result in an increased stress. Nevertheless, the flux could act indirectly via an influence on the nitrogen concentration, as the stress will increase at increasing nitrogen concentration. This, however, can be excluded, as we clearly show that the results are not consistent with a concentration-dependent diffusion model. On the other hand, the variation of the nitrogen concentration might create a stress gradient, which is expected to enhance the inward diffusion [177]. However, the observed concentration profiles at the leading edge, where the stress gradient is expected to be the largest, look rather similar, so that any stress gradient would also be similar. Nevertheless, the magnitude of the stress gradient in single crystalline samples might depend on the orientation. Czerwiec [113] have analyzed the influence of stress gradient in the nitrided layer on nitrogen diffusion

and showed that the stress gradient indeed affects diffusion in Inconel 690 (Ni based alloy), but stated that only a part of diffusion anisotropy can be explained by the stress gradient. In iron based austenitic stainless steels the situation is even more complicated due to the inversion of elastic constants with the increasing nitrogen concentration [132]. Thus, more sophisticated approaches and additional experimental data are necessary to elucidate any stress-gradient enhanced interstitial diffusion.

A model for rapid nitrogen diffusion was proposed by Gemma et al. [178], based on an analogy with the principle of a laser. The nitrogen concentration at the surface of the alloy is elevated from the ground state of the alloy's matrix to a nitrogen supersaturated state by "pumping" off a large amount of nitrogen from the nitriding media. At the same time CrN Guinier–Preston zones are formed locally and randomly in this phase. The locally high chemical potential will drop to a lower level by precipitating the GP zone and accompanying liberation of heat would thermally excite the surrounding lattice. The presence of the high nitrogen concentration will result in redissolution of the GP zones. Thus, the nitrogen subsequently arriving from the surface will maintain the high chemical potential. Under these conditions, the precipitation and redissolution of the GP zones will take place cyclically in the phase during nitriding. However, the results of this work on plasma nitriding (Chapter 4) show that CrN GP zones tend to grow and there is no redissolution, as substantial amounts of CrN, as-detected by XRD, form in the surface layer.

Abrasonis et al. [111] have recently proposed an explanation for this enhanced diffusion based on a quasi-particle-enhanced mobility. According to this explanation, stable and mobile intrinsic localized (vibrational) modes (ILMs) might be created by energetic ions and propagate along atomic chains, which could accelerate the diffusion of interstitial N atoms. Ions with higher energy are supposed to create more ILMs as well as higher current densities should also result in higher ILM production. Furthermore, recently it was proven experimentally that ILMs do exist in conventional three-dimensional crystals in thermal equilibrium: in elemental α -U metal above ~ 450 K and in a simple ionic crystal, NaI, above ~ 555 K [179]. This model is consistent with the enhancement of the diffusion coefficient during nitriding and the diffusion coefficient dependence on the ion energy and current density. Nevertheless, it remains speculative unless further experimental or theoretical substantiation could be provided that ILMs can be generated by energetic ions and they do exist in nitrated ASS.

In the previous Chapter it was concluded that Cr and Ni forms coherent domains. As N diffusion in CrN is four orders of magnitude lower than in γ' -Fe₄N [138, 139], such zones would act like walls. The nitrogen trapping and detrapping could still occur on the CrN

zone boundaries. The formation of CrN-like domains would leave regions depleted of Cr. As the N diffusivity in γ' -Fe₄N is an order of magnitude higher than in ASS [139], such regions without Cr would serve as fast diffusion paths. Further, such zones may create local stress gradients. Thus, nitrogen diffusion in the vicinity of CrN-like domains could be even faster than in the Fe₄N matrix. It was discussed that spinodal decomposition gives concentration waves along the axis with the lowest Young modulus Y_{hkl} value. Austenitic steel exhibits a maximum of Y_{hkl} in the $\langle 111 \rangle$ directions ($Y_{\langle 111 \rangle} = 303$ GPa) and a minimum in the $\langle 100 \rangle$ directions ($Y_{\langle 100 \rangle} = 100$ GPa) [132]. This contrasts with γ' -Fe₄N, which shows a completely reverse anisotropy of elastic behavior: the maximum of Y_{hkl} occurs in the $\langle 100 \rangle$ directions ($Y_{\langle 100 \rangle} = 226$ GPa), and the minimum of Y_{hkl} occurs in the $\langle 111 \rangle$ directions ($Y_{\langle 111 \rangle} = 128$ GPa) [132]. If spinodal decomposition starts when ASS is saturated with nitrogen, then decomposition would occur in the γ' -Fe₄N like matrix and concentration waves would develop along $\langle 111 \rangle$ direction. If lower amounts of nitrogen would be sufficient for decomposition, then concentration waves would develop along $\langle 001 \rangle$. However, the increasing nitrogen concentration results in a reverse anisotropy of elastic behavior, and again the favorable direction would be $\langle 111 \rangle$. It is not clear if this change leads to a reorientation of the existing domains or only additional strain. Nevertheless, as nitrogen is likely to diffuse along domains, in the (111) oriented sample the diffusion path should be longer to achieve the same nitrided layer thickness. Thus, CrN-like domains should occur on $\{001\}$ planes. This would imply that spinodal decomposition starts at lower nitrogen concentrations. In the (001) oriented sample domains would form perpendicular to the surface and in (111) oriented sample domains would make an angle of 55°. In the (001) sample nitrided at 400°C the nitrided layer is 1.5 μm deep, in the (110) sample it is 0.95 μm , and in the (111) sample — 0.7 μm . The correction for sputtering gives 2 μm , 1.55 μm and 1.35 μm for (001), (110) and (111) oriented samples, respectively. Assuming that diffusion is affected only by the domain orientation in the sample, the angle between the normal to the surface and the domains yields 1.41 μm and 1.15 μm nitrided layer for the (110) and (111) oriented samples, respectively. These values are lower than the ones obtained experimentally as the domains are assumed to be continuous in the estimations. This disagreement can be explained by the final size of GP zones which are most probably very small. Thus, the formation of CrN-like domains on $\{001\}$ planes is consistent with the nitrogen penetration depth anisotropy. A recent atom probe tomography investigation of Fe–5 wt%Cr alloy nitrided in an ammonia atmosphere at 590°C indeed show a development of CrN platelets parallel to all the $\{001\}$ planes of the matrix [180]. They have a mean diameter of 6.5 nm and a thickness of several Å. Nitrogen clustering and fragments of nitrides are already observed in the nitriding front,

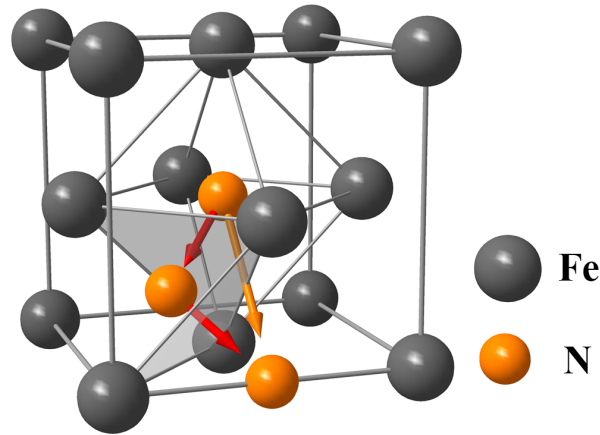


Figure 5.14: Possible nitrogen diffusion jumps — directly from one octahedral position to the other (orange arrow), or via tetrahedral position (red arrows).

where nitrogen concentration is much lower than in the layer already passed by the front. This shows that low nitrogen concentration is sufficient for destabilization of the alloy. Fe-5 wt%Cr alloy has a *bcc* structure, however, like in ASS the elastic modulus is least in the $\langle 001 \rangle$ directions. Thus, it is very likely that in ASS spinodal decomposition also starts with low nitrogen concentration and CrN zones develop parallel to the $\{001\}$ planes.

This is also consistent with the results of the annealing experiment. During annealing nitrogen concentration decreases as it diffuses towards the bulk. However, there is no additional nitrogen supply, and the chemical potential for decomposition decreases. Slower decomposition leads to an effective nitrogen trapping at the leading edge and results in a slower nitrogen diffusivity. As mentioned above, with the increasing nitrogen concentration ASS undergoes a reverse of the elastic anisotropy behavior which, interacting with CrN zones, possibly sets additional stress. This stress can relax during annealing, which likely slows the nitrogen diffusion. Also with the decreasing nitrogen concentration the elastic constants change towards *fcc* Fe further relaxing stress. This is in agreement with the observed narrowing of the XRD peaks and supports the formation of CrN zones in *fcc* Fe environment. In addition, point defects, like vacancies created during ion irradiation, may recombine during annealing and decrease the nitrogen diffusivity. However, the effect of vacancies is small [111].

The results of section 5.3 show that the change of the diffusion activation energy E (from 1.36 to 1.13 eV) is about 10% while D_0 changes by two orders of magnitude. The most important contribution to E comes from the energy required to strain the lattice. The nitrogen atom can jump from one octahedral site to the other directly by pushing two atoms apart, or nitrogen can take an indirect path via a tetrahedral position (Fig. 5.14).

Taking the lattice constant $a = 3.6 \text{ \AA}$, gives the interatomic distance between barrier atoms $b = 2.546 \text{ \AA}$. For the nitrogen atom with an atomic radius of 0.75 \AA , the two barrier atoms ($r_{\text{Fe}} = 1.17 \text{ \AA}$) need to be displaced by 0.65 \AA . This means that the Fe-Fe interatomic distances have to be stretched out by about 51%. The strain energy w per unit volume per nitrogen atom required to strain the Fe-Fe bond within the elementary volume of the two barrier atoms is approximately given by $w = 1/2Y\epsilon^2$ (Y is the Young modulus and ϵ is the strain). By assuming values of Y and ϵ equal to 198 GPa for ASS [132] and 0.51, respectively, w is estimated to be $25.7 \times 10^9 \text{ J m}^{-3} \text{ atom}^{-1}$. The elementary volume of “hard spheres” is $1.34 \times 10^{-29} \text{ m}^3$. Therefore, the strain energy is estimated to be 2.15 eV. The nitrogen atom moving through the tetrahedral position has to overcome a three atom barrier. However, here the Fe atoms have to be displaced by about 31%, therefore, the strain energy is about 1.16 eV, which agrees very well with the obtained diffusion activation energy. Thus, it is favorable for N to take the diffusion path via the tetrahedral position. This diffusion path was also obtained from DFT calculations for C and N diffusion in steel [174, 175].

The present study clearly shows that D_0 depends strongly on the orientation (see Fig. 5.5 and Table 5.2): it increases by two orders of magnitude when changing the single crystal orientation from (111) to (001). Fitting experimental points in Arrhenius plot with the same E as for (111) orientation gives $D_0 = 2.4 \times 10^{-3} \text{ cm}^2/\text{s}$. This would result in a fairly bad fit, and still the value is about two times higher than that of (111) orientation. Also it should be stressed that the same E value for the (001) orientation is obtained irrespectively of the employed ion energy or current density. The analysis of entropy change gives no satisfactory explanation. According to Zener’s model for the diffusion of interstitials, Gibbs free energy of migration represents the work to deform the lattice elastically during the course of an atomic jump [173]. For the jump via the tetrahedral position the barrier atoms move in $\langle 221 \rangle$ directions. If the diffusion path is the same for all orientations, then ΔS_s should also be the same. The fact that ΔS_s is more than two times higher for the (001) orientation compared to the (111) orientation suggests that in the (001) oriented sample the local environment or the diffusion mechanism differs significantly. When nitrogen jumps into the vicinity of CrN-like domain, which acts like a diffusion barrier, nitrogen successive jumps becomes more correlated as the jump through the domain requires a higher activation energy, while the diffusion barrier along the domain is possibly lower than in the surrounding matrix. Further, around a CrN-like domain the N concentration is higher and N atoms could form interstitial clusters. The movement of atoms in a cluster is even more correlated to the previous jumps. Thus, the correlation factor in Eq. (2.7) would be higher than one. Typical correlation factor values

for such clusters are around 4. This however, is still not enough to explain the difference in D_0 values between (001) and (111) orientations. In the cluster a jump of one atom can trigger the whole chain of atoms to jump forward. In this case the parameter a in Eq. (2.7) is no longer a lattice parameter but a length of the jumping atom chain. As a is squared in the D_0 expression, $4a$ already results in the change of order of magnitude in D_0 . The activation energy becomes higher for such a jump, however, the decrease of the exponential term is over-compensated by an increase of D_0 . In the (001) oriented sample the easy axis is oriented perpendicular to the surface and favors formation of CrN-like domains. Thus, in the (001) oriented sample domains could be larger or/and the density could be higher than in the (111) oriented sample. Also, high nitrogen concentrations result in the initiation and growth of internal stresses. These stresses generate dislocations that have their own non-symmetric stress fields. The region around dislocation may attract interstitials and, as a result, Cottrell atmospheres may be created [181]. Thus, dislocations could also promote the formation of interstitial clusters. The obtained D_0 and E values suggest that in the (111) oriented sample nitrogen is mostly diffusing like in an ordinary solid solution, while in the (001) oriented sample the effect of defects such as CrN-like domains or dislocations is much more pronounced.

The results of section 5.4 show that the nitrogen diffusivity increases concomitantly with the ion energy and flux. The same dependence has been reported in several studies on the influence of ion energy [2,3,8,24,25,45–47] and current density [3,25,37,48–50]. However, in some of them the nitriding was performed using plasma implantation techniques, where ion energy and current density might be coupled. In others, the nitrided depth was estimated by indirect methods. Moreover, all these studies used polycrystalline materials. Thus, a quantitative comparison of the results is difficult. Nevertheless, an experiment, which is most similar to the present ones, was reported in Ref. [50]. The samples were implanted with 1.2 keV N ions. Diffusion pre-exponential factors equal to 2.0, 3.1 and 5.4×10^{-4} cm²/s were reported for the ion current densities of 0.5, 0.67 and 0.83 mA/cm², respectively. The diffusion activation energy was taken as 1.1 eV. These values are closest to the values of the (111) orientation. From the present results, assuming the same diffusion activation energy of 1.1 eV, the diffusion pre-exponential factor would be equal to 6.6×10^{-4} cm²/s for (111) orientation and nitriding with 0.5 mA/cm² and 1 keV at 400°C. This is more than three times higher than in Ref. [50]. For the ion current density of 0.7 mA/cm², $D_0 = 1.0 \times 10^{-3}$ cm²/s, which is about two times higher. The discrepancy is rather acceptable as different types of ASS have been used (304L instead of 316L of this study), polycrystalline samples instead of single crystals, and the fact that the temperature was changing during the experiment in Ref. [50].

Radiation induced defects [182] have been suggested to explain the fast nitrogen diffusion. However, it was shown that nitrogen diffusion is faster than that of the induced defects [125]. Also it has been argued that the concentration of vacancies created by ion irradiation is far too low to achieve significant diffusion increase [111]. Nevertheless, even if the amount of vacancies is too small to move nitrogen, it may be high enough to displace significant amounts of matrix atoms and enhance spinodal decomposition [183]. According to SRIM2010 calculations, 9, 18.6 and 22.5 vacancies/ion are produced by 0.5, 1 and 1.2 keV nitrogen ions, respectively. Thus higher implantation energies would result in higher vacancy concentration and, consequently, in faster decomposition. Similarly, the higher ion current densities would also produce more vacancies. Also the probability to form bivacancies increases with the flux, and bivacancies are known to diffuse even faster than vacancies in *fcc* materials [184]. However, the influence of vacancies is probably limited to the depth of some hundreds of nm. Thus, without further experiments or theoretical calculations it is rather difficult to speculate about the effect of vacancies on the nitrogen diffusion.

5.6 Summary

The nitrogen diffusivity in ASS single crystals with the (001), (110) and (111) orientations has been investigated during ion beam nitriding and thermal annealing. The nitrogen penetration depth strongly depends on the orientation of the single crystal, and is largest, intermediate and lowest for the (001), (110) and (111) orientation, respectively. The diffusion coefficient is higher by a factor of 2 for the (001) orientation in relation to the (111) orientation. The diffusivity during post-nitriding thermal annealing is significantly lower than that during ion beam nitriding and is independent on the crystalline orientation. The pre-exponential factor D_0 , obtained using trapping-detrapping model, varies by two orders of magnitude in the order $D_{0,(001)} > D_{0,(011)} > D_{0,(111)}$, while the activation energy E is almost the same for the (111) and (110) orientations and higher for the (001) orientation. For the (110) and (111) orientations, the E values are consistent with those calculated by employing a simple elastic theory and imply an indirect nitrogen diffusion path between octahedral interstitial positions via a tetrahedral position. The higher E value for the (001) orientation possibly indicates different diffusion mechanism. The nitrogen diffusivity increases with increasing ion current density and ion energy. For the (001) orientation the diffusion activation energy almost does not depend on the ion energy and current density, while the pre-exponential factor increases by ~ 2.7 , when ion energy increases from 0.5 to 1.2 keV. No clear D_0 tendency on the ion current density

could be observed.

The formation of CrN-like domains is proposed to explain the nitrogen diffusion anisotropy. CrN-like domains form a barrier for diffusing nitrogen and the arrangement along $\{001\}$ is in agreement with the observed diffusion anisotropy. The elastic anisotropy of ASS favors formation of domains in the (001) orientated crystal; zones could be larger and/or the density higher. Also, nitrogen concentration around Cr is higher than in the surrounding matrix and interstitial clusters might form. Thus likely in the (111) oriented sample nitrogen is mostly diffusing like in an ordinary solid solution, while in the (001) oriented sample the effect of CrN-like domains is much more pronounced.

6 Conclusions and Outlook

The purpose of this work was to improve the understanding of the microstructure of the S phase and of the influence of the microstructure on the nitrogen transport during the ion beam nitriding.

The structural nature of the nitrogen enriched layer (S phase) has been investigated in the plasma nitrided ASS. It has been found that:

- ☐ Fe, Cr and Ni have different local chemical environments.
- ☐ Cr is similar to CrN, Fe is similar to γ -Fe₄N, and Ni has a metallic environment.
- ☐ Domains, rich in Cr and Ni, are coherent with the matrix.
- ☐ The data also provides a strong evidence that the decomposition of the nitrogen saturated ASS is of spinodal type.

Therefore, the S phase is interpreted as heterogeneous, where Cr and Ni form coherent domains in the Fe₄N-like matrix. The stability of the N supersaturated solid solution depends on the N concentration and temperature. For temperatures above 500°C nucleation and growth mechanism is most likely dominant, while for lower temperatures and high N concentrations decomposition of ASS is more of a spinodal nature. The degree of decomposition in the case of a spinodal decomposition depends on the N concentration, temperature and time, and is different at various depths in the nitrided layer, being the strongest in the top surface layer.

In order to gain experimental data on nitrogen diffusion, ion beam nitriding of ASS single crystals with the (001), (110) and (111) orientations has been employed extensively. Nitrogen diffusion dependences on the crystal orientation, nitriding temperature, ion energy and flux can be summarized as follows:

- ☐ $D_{(001)} > D_{(011)} > D_{(111)}$
- ☐ $E_{(001)} \gtrsim E_{(011)} \approx E_{(111)}$
- ☐ $100 \times D_{0,(001)} \approx D_{0,(011)} \gtrsim D_{0,(111)}$
- ☐ The diffusivity during post-nitriding thermal annealing is significantly lower than that during ion beam nitriding and is independent of the crystalline orientation.

- ⊃ The nitrogen diffusivity increases with the increasing ion current density and ion energy.
- ⊃ E almost does not depend on the ion energy and current density for the (001) orientation.

The following nitrogen diffusion mechanism is proposed from the comparison of data from two experimental parts. Cr and Ni domains could be forming along the {001} or {111} planes. The first case is in agreement with the observed diffusion anisotropy. Ni and Cr domains are expected to influence nitrogen diffusion providing fast diffusion path along the domains or by blocking the direct diffusion paths. Around the CrN-like zones N probably occupies every interstitial position and, as a result, interstitial clusters could be forming. The movement of a cluster is much more correlated than of a single interstitial. Also, a jump of one interstitial in the cluster sometimes triggers a jump of the whole interstitial chain. These two factors could explain an increase of D_0 by orders of magnitude. It is expected that the elastic anisotropy of ASS favors the zone formation parallel to the (001) orientation; the zones could be larger and/or the density higher. Thus, likely in the (111) oriented sample, nitrogen is mostly diffusing like in an ordinary solid solution, while in the (001) oriented sample the effect of Cr and Ni domains is much more pronounced.

The results of this work suggest that it might be possible to control the properties by controlling the balance supersaturation/decomposition. If low nitrogen concentrations are needed to reach the spinodal point, the decomposition would proceed in the *fcc* Fe environment and saturation with N after the decomposition would result in the inversion of the elastic constants and in large stresses. However, if the supersaturation can be achieved before the beginning of the decomposition then the separation would occur in the Fe₄N-like environment without the inversion of the elastic constants and associated stresses. The stress could be added by lowering the nitrogen concentration during annealing as this would change the elastic constants back towards *fcc* Fe.

The orientation, morphology and concentration of domains rich in Cr and Ni remain to be identified. Three-dimensional field ion microscopy and atomic probe tomography have such analytical capabilities to answer this question as shown by Jessner et al. [180] on a nitrided Fe-5 wt%Cr alloy and by Takahashi et al. [185] on copper and chromium nitrides in steel. As well, an X-ray anomalous scattering can be used. X-ray energy can be tuned to the absorption edge of one element effectively probing distribution of that element. The mixed spectroscopic-scattering technique has a much better statistics and a possibility to perform *in-situ* experiments. The fact that nitrogen is diffusing in

a heterogeneous environment suggests that 3D or at least 2D modeling should be used. Alternatively, phase field models could be applied.

The findings about the structure can be associated with the properties of the S phase: increased hardness, corrosion resistance and induced magnetism. The surface hardening due to nitriding processes can be due to [186]: (1) precipitate dispersion–hardening: hard insoluble precipitates are incorporated into the matrix; (2) solid solution: interstitials in a solid solution which create Cottrell atmospheres that lock dislocations; and (3) a surface residual stress induced by the ion radiation damage. The CrN zones create a highly disordered-distorted regions that contribute to the residual surface stress, which results in high hardness [187]. In addition, the dislocation movement mechanism around small precipitates is by bowing, which also results in higher hardness [188]. Also, for higher nitrogen concentrations there is enough nitrogen to form Cottrell atmospheres. The first two cases are likely responsible for the increased hardness in gas and plasma nitriding, while all three cases could occur for higher energy nitriding.

In stainless steels, Cr is responsible for corrosion resistance as it creates a thin passive oxide layer which prevents further oxidation. Nitriding conducted at the temperature above 460°C results in the precipitation of CrN in large amounts [134]. Next to the CrN precipitates, Cr-depleted zones do not contain a sufficiently high chromium concentration, which are a subject to the active corrosion process. If the ratio between Cr-depleted areas and the entire surface of a sample increase, the corrosion behavior of the former areas can more and more control the corrosion behavior of the entire nitrided sample. Nitriding at temperatures below 450°C do not compromise the corrosion resistance because the Cr spatial segregation scale is still small. Despite the fact that small Cr domains are formed, they are likely close enough to each other to participate in the passive layer formation. It seems that in the regions between the domains the Cr concentration is lower than in ASS, but still sufficient. In addition, the corrosion resistance is even improved [87] due to the positive influence of ferrous nitrides on the chemical reactivity potential of the material.

Basso et al. [88] found that the ferromagnetic-paramagnetic transition takes place around the inflection in the nitrogen profile, which corresponds to the Cr concentration. It is suggested that the ferromagnetism due to N incorporation occurs by two different mechanisms, (1) the rearrangement of 3d electrons after changing Fe–Cr–Ni atomic distances [89] and/or (2) the formation of metallic nitrides [88]. The authors argue that the most important effect governing the ferromagnetism at N concentrations similar to Cr is the N–Cr interaction, which removes the chromium 3d electrons from the metal alloy valence band. This effectively leaves Fe and Ni, which are ferromagnetic [189]. The results of this thesis show that increasing nitrogen concentration results in Cr segregation

effectively leaving the zones rich in Fe and Ni. FeNi alloys are ferromagnetic [190], thus the segregation of Cr could be more important for the ferromagnetic-paramagnetic transition than the N–Cr interaction. It would also correlate with the assumption that the spinodal decomposition starts at low nitrogen concentrations. Also, the decomposition of ASS results in a large disorder and apparently the change in Fe–Cr–Ni atomic distances has a significant influence on ferromagnetism. As for ferromagnetism at higher nitrogen concentrations, all types of iron nitrides (Fe_{16}N_2 , Fe_4N , Fe_2N , $\text{Fe}_3\text{N}_{1+x}$) are ferromagnetic [191–193].

The findings of this work suggest an approach to tune the properties of alloys via interstitial diffusion. Spinodal decomposition is a fundamental process, thus, similar heterogeneous phases can be induced by saturating homogeneous alloys with chemically active species. The processing should be carried out at relatively low temperatures where diffusion of substitutional atoms is constrained. This implies a beneficial use of ionized environments to produce diffusing species. The most similar process is carburizing of stainless steels [194]. Cr also forms traps for C, although to a lesser extent due to lower affinity as compared to N [18]. The supersaturated carbon solid solution is metastable as well and tends to develop chromium carbides [39]. Thus, it can be expected that a very similar structure is developing during carburizing too. Another thermochemical diffusion surface treatment of steels is boronizing. Due to high B reactivity with Fe, single Fe_2B or a double intermetallic phase (Fe_2B , FeB) is obtained [195]. However, for high alloy steels with low iron concentration similar structures presumably could be obtained. Another topic where such approach could be applied is hydrogen storage. Hydrogen also forms interstitial hydrides, e.g. palladium has been known as an excellent metallic absorber of hydrogen [196]. A large hydrogen capacity and good desorbing properties were found in Ti–V–Mn alloys with modulated structure [197]. Thus, by a careful choice of alloying elements spinodal decomposition could be induced by hydrogen saturation. It should result in a precipitation of very fine hydrides, thereby increasing hydrogen solubility and release due to the presence of numerous interfaces.

Bibliography

- [1] A. M. JONES and S. J. BULL, *Surf. Coat. Technol.* **83**, 269 (1996).
- [2] R. WEI, *Surf. Coat. Technol.* **83**, 218 (1996).
- [3] D. L. WILLIAMSON, J. A. DAVIS, P. J. WILBUR, J. J. VAJO, R. WEI, and J. N. MATOSSIAN, *Nucl. Instrum. Methods Phys. Res. B* **127–128**, 930 (1997).
- [4] J. P. RIVIÈRE, J. P. MEHEUST, P. VILLAIN, C. TEMPLIER, M. CAHOREAU, G. ABRASONIS, and L. PRANEVIČIUS, *Surf. Coat. Technol.* **158–159**, 99 (2002).
- [5] S. HANNULA, P. NENONEN, and J. HIRVONEN, *Thin Solid Films* **181**, 343 (1989).
- [6] M. SAMANDI, B. SHEDDEN, D. SMITH, G. COLLINS, R. HUTCHINGS, and J. TENDYS, *Surf. Coat. Technol.* **59**, 261 (1993).
- [7] G. COLLINS, R. HUTCHINGS, K. SHORT, J. TENDYS, X. LI, and M. SAMANDI, *Surf. Coat. Technol.* **74–75**, 417 (1995).
- [8] D. L. WILLIAMSON, O. ÖZTÜRK, R. WEI, and P. J. WILBUR, *Surf. Coat. Technol.* **65**, 15 (1994).
- [9] M. P. FEWELL, D. R. G. MITCHELL, J. M. PRIEST, K. T. SHORT, and G. A. COLLINS, *Surf. Coat. Technol.* **131**, 300 (2000).
- [10] T. CZERWIEC, N. RENEVIER, and H. MICHEL, *Surf. Coat. Technol.* **131**, 267 (2000).
- [11] M. K. LEI and Z. L. ZHANG, *J. Vac. Sci. Technology A* **13**, 2986 (1995).
- [12] E. MENTHE and K.-T. RIE, *Surf. Coat. Technol.* **116–119**, 199 (1999).
- [13] Y. SUN, X. Y. LI, and T. BELL, *J. Mater. Sci.* **34**, 4793 (1999).
- [14] K. MARCHEV, M. LANDIS, R. VALLERIO, C. COOPER, and B. GIESSEN, *Surf. Coat. Technol.* **116–119**, 184 (1999).
- [15] V. SINGH, K. MARCHEV, C. COOPER, and E. MELETIS, *Surf. Coat. Technol.* **160**, 249 (2002).
- [16] E. I. MELETIS, V. SINGH, and J. C. JIANG, *J. Mater. Sci. Lett.* **21**, 1171 (2002).
- [17] J. BARANOWSKA, K. SZCZECINSKI, and M. WYSIECKI, *Surf. Coat. Technol.* **151–152**, 534 (2002).

- [18] T. CHRISTIANSEN and M. A. J. SOMERS, *Surf. Eng.* **21**, 445 (2005).
- [19] J. MICHALSKI, J. TACIKOWSKI, P. WACH, E. LUNARSKA, and H. BAUM, *Met. Sci. Heat Treat.* **47**, 516 (2005).
- [20] E. MENTHE, K.-T. RIE, J. SCHULTZE, and S. SIMSON, *Surf. Coat. Technol.* **74–75**, 412 (1995).
- [21] E. MENTHE, A. BULAK, J. OLFE, A. ZIMMERMANN, and K.-T. RIE, *Surf. Coat. Technol.* **133–134**, 259 (2000).
- [22] T. BACCI, F. BORGIOLI, E. GALVANETTO, and G. PRADELLI, *Surf. Coat. Technol.* **139**, 251 (2001).
- [23] K. MARCHEV, C. COOPER, J. BLUCHER, and B. GIESSEN, *Surf. Coat. Technol.* **99**, 225 (1998).
- [24] R. WEI, J. J. VAJO, J. N. MATOSSIAN, P. J. WILBUR, J. A. DAVIS, D. L. WILLIAMSON, and G. A. COLLINS, *Surf. Coat. Technol.* **83**, 235 (1996).
- [25] R. WEI, B. SHOGRIN, P. J. WILBUR, O. ÖZTÜRK, D. L. WILLIAMSON, I. IVANOV, and E. METIN, *J. Tribol.-T. Asme* **116**, 870 (1994).
- [26] S. BULL, A. JONES, and A. MCCABE, *Surf. Coat. Technol.* **83**, 257 (1996).
- [27] S. PARASCANDOLA, R. GUNZEL, R. GROTZSCHEL, E. RICHTER, and W. MOLLER, *Nucl. Instr. Meth. B* **136–138**, 1281 (1998).
- [28] N. RANDALL, N. RENEVIER, H. MICHEL, and P. COLLIGNON, *Vacuum* **48**, 849 (1997).
- [29] J. DE BAERDEMAEKER, J. COLAUX, G. TERWAGNE, and C. DAUWE, *Radiat. Phys. Chem.* **68**, 605 (2003).
- [30] A. SAKER, H. HE, T. CZERWIEC, X. LI, L. TRAN HUU, C. DONG, H. MICHEL, and C. FRANTZ, *Thin Solid Films* **516**, 1029 (2008).
- [31] K. ICHII, K. FUJIMURA, and T. TAKAO, *Technol. Rep. Kansai Univ.* **27**, 135 (1986).
- [32] K. MARCHEV, R. HIDALGO, M. LANDIS, R. VALLERIO, C. COOPER, and B. GIESSEN, *Surf. Coat. Technol.* **112**, 67 (1999).
- [33] T. L. CHRISTIANSEN, K. V. DAHL, and M. A. J. SOMERS, *Mater. Sci. Tech.* **24**, 159 (2008).
- [34] C. TEMPLIER, J. STINVILLE, P. VILLECHAISE, P. RENAULT, G. ABRASONIS, J. RIVIÈRE, A. MARTINAVICIUS, and M. DROUET, *Surf. Coat. Technol.* **204**, 2551 (2010).

- [35] X. XU, L. WANG, Z. YU, and Z. HEI, *Surf. Coat. Technol.* **132**, 270 (2000).
- [36] T. CHRISTIANSEN and M. A. J. SOMERS, *Scr. Mater.* **50**, 35 (2004).
- [37] F. BORGIOLI, A. FOSSATI, E. GALVANETTO, T. BACCI, and G. PRADELLI, *Surf. Coat. Technol.* **200**, 5505 (2006).
- [38] J. ODDERSHEDE, T. L. CHRISTIANSEN, K. STÅHL, and M. A. J. SOMERS, *J. Mater. Sci.* **43**, 5358 (2008).
- [39] T. L. CHRISTIANSEN and M. A. J. SOMERS, *Int. J. Mater. Res.* **100**, 1361 (2009).
- [40] J. ODDERSHEDE, T. L. CHRISTIANSEN, K. STÅHL, and M. A. J. SOMERS, *Scr. Mater.* **62**, 290 (2010).
- [41] D. WILLIAMSON, J. DAVIS, and P. WILBUR, *Surf. Coat. Technol.* **103–104**, 178 (1998).
- [42] F. PEDRAZA, M. REFFASS, G. ABRASONIS, C. SAVALL, J. P. RIVIÈRE, and J. F. DINHUT, *Surf. Coat. Technol.* **176**, 236 (2004).
- [43] X. L. XU, L. WANG, Z. W. YU, and Z. K. HEI, *Surf. Coat. Technol.* **192**, 220 (2005).
- [44] F. PEDRAZA, C. SAVALL, G. ABRASONIS, J. P. RIVIÈRE, J. F. DINHUT, and J. L. GROSSEAU-POUSSARD, *Thin Solid Films* **515**, 3661 (2007).
- [45] S. LEIGH, M. SAMANDI, G. A. COLLINS, K. T. SHORT, P. MARTIN, and L. WIELUNSKI, *Surf. Coat. Technol.* **85**, 37 (1996).
- [46] J. F. LIN, K. W. CHEN, C. C. WEI, and C. F. AI, *Surf. Coat. Technol.* **197**, 28 (2005).
- [47] N. TSUBOUCHI, Y. MOKUNO, A. CHAYAHARA, and Y. HORINO, *Surf. Coat. Technol.* **196**, 271 (2005).
- [48] O. ÖZTÜRK and D. L. WILLIAMSON, *J. Appl. Phys.* **77**, 3839 (1995).
- [49] C. MURATORE, S. G. WALTON, D. LEONHARDT, R. F. FERNSLER, D. D. BLACKWELL, and R. A. MEGER, *J. Vac. Sci. Technol. A* **22**, 1530 (2004).
- [50] G. ABRASONIS, J. P. RIVIÈRE, C. TEMPLIER, L. PRANEVIČIUS, and N. P. BARRADAS, *J. Appl. Phys.* **97**, 124906 (2005).
- [51] H. HE, T. CZERWIEC, C. DONG, and H. MICHEL, *Surf. Coat. Technol.* **163–164**, 331 (2003).
- [52] G. ABRASONIS, J. P. RIVIÈRE, C. TEMPLIER, A. DECLÉMY, S. MUZARD, and L. PRANEVIČIUS, *Surf. Coat. Technol.* **196**, 262 (2005).

- [53] G. ABRASONIS, J. P. RIVIÈRE, C. TEMPLIER, A. DECLÉMY, L. PRANEVIČIUS, and X. MILHET, *J. Appl. Phys.* **97**, 1 (2005).
- [54] G. ABRASONIS, J. P. RIVIÈRE, C. TEMPLIER, S. MUZARD, and L. PRANEVIČIUS, *Surf. Coat. Technol.* **196**, 279 (2005).
- [55] S. GRIGULL and S. PARASCANDOLA, *J. Appl. Phys.* **88**, 6925 (2000).
- [56] K. LO, C. SHEK, and J. LAI, *Mater. Sci. Eng. R* **65**, 39 (2009).
- [57] R. W. K. HONEYCOMBE and H. K. D. H. BHADSHIA, *Steels: Microstructure and Properties*, 2nd edition, Butterworths–Hienemann, London, 1995.
- [58] H. SCHNEIDER, *Foundry Trade Journal* **108**, 562 (1960).
- [59] J. M. GALLEGO, S. Y. GRACHEV, D. M. BORSA, D. O. BOERMA, D. ĚCIJA, and R. MIRANDA, *Phys. Rev. B* **70**, 115417 (2004).
- [60] B. J. KOOI, M. A. J. SOMERS, and E. J. MITTEMEIJER, *Metall. Mater. Trans. A* **27**, 1063 (1996).
- [61] N. HEIMAN and N. S. KAZAMA, *J. Appl. Phys.* **52**, 3562 (1981).
- [62] A. OUELDEENNAOUA, E. BAUER-GROSSE, M. FOOS, and C. FRANTZ, *Scripta Metall.* **19**, 1503 (1985).
- [63] H. NAKAGAWA, S. NASU, H. FUJII, M. TAKAHASHI, and F. KANAMARU, *Hyperfine Interact.* **69**, 455 (1992).
- [64] K. SUZUKI, H. MORITA, T. KANEKO, H. YOSHIDA, and H. FUJIMORI, *J. Alloys Compd.* **201**, 11 (1993).
- [65] J. PHILIBERT, *Atom Movements, Diffusion and Mass Transport in Solids*, Les Editions de Physique, Les Ulis, France, 1991.
- [66] J. HIRVONEN and A. ANTTILA, *Appl. Phys. Lett.* **46**, 835 (1985).
- [67] D. ASKELAND and P. PHULE, *Essentials of Materials Science and Engineering*, Thomson Publishers, Toronto, Canada, 2004.
- [68] J. E. CAHN, JOHN W. AND HILLIARD, *J. Chem. Phys.* **28**, 258 (1958).
- [69] J. E. CAHN, JOHN W. AND HILLIARD, *J. Chem. Phys.* **31**, 688 (1959).
- [70] J. W. CAHN, *Acta Metall.* **8**, 554 (1960).
- [71] V. P. SKRIPOV and A. V. SKRIPOV, *Usp. Fiz. Nauk* **128**, 193 (1979).
- [72] R. D. DOHERTY, *In Physical Metallurgy*, pp. 1364–1370, North-Holland, Amsterdam, (Eds R. W. Cahn, P. Haasen) 4th edition, 1996.

- [73] P. HASSEN, *Physical Metallurgy*, Cambridge University Press, New York, 1978.
- [74] J. CAHN, *Acta Metall.* **9**, 795 (1961).
- [75] R. RACHBAUER, E. STERGAR, S. MASSL, M. MOSER, and P. MAYRHOFER, *Scripta Mater.* **61**, 725 (2009).
- [76] C. CAPDEVILA, M. MILLER, K. RUSSELL, J. CHAO, and J. GONZALEZ-CARRASCO, *Mater. Sci. Eng. A* **490**, 277 (2008).
- [77] M. NASTASI, J. MAYER, and J. K. HIRVONEN, *Ion-Solid Interactions: Fundamentals and Applications*, Cambridge University Press, 2004.
- [78] Y. ZENGLIANG and Y. LIANGDENG, *Introduction to Ion beam biotechnology*, Springer, 2006.
- [79] J. BIERSACK and L. HAGGMARK, *Nucl. Instr. Meth.* **174**, 257 (1980).
- [80] J. ZIEGLER, J. BIERSACK, and U. LITTMARK, *The Stopping and Range of Ions in Solids*, Pergamon Press, New York, 1985.
- [81] U. K. MUDALI, H. S. KHATAK, and B. RAJ, *Mater. Manuf. Process* **19**, 61 (2004).
- [82] L. GONTIJO, R. MACHADO, S. KURI, L. CASTELETTI, and P. NASCENTE, *Thin Solid Films* **515**, 1093 (2006).
- [83] A. SAKER, C. LEROY, H. MICHEL, and C. FRANTZ, *Mater. Sci. Eng. A* **140**, 702 (1991).
- [84] D. WILLIAMSON, O. ÖZTÜRK, S. GLICK, R. WEI, and P. WILBUR, *Nucl. Instr. Meth. B* **59–60**, 737 (1991).
- [85] J. RIVIERE, P. MEHEUST, and J. VILLAIN, *Surf. Coat. Technol.* **158–159**, 647 (2002).
- [86] S. MANDL, R. GUNZEL, E. RICHTER, and W. MOLLER, *Surf. Coat. Technol.* **100–101**, 372 (1998).
- [87] A. FOSSATI, F. BORGIOLI, E. GALVANETTO, and T. BACCI, *Corros. Sci.* **48**, 1513 (2006).
- [88] R. L. O. BASSO, V. L. PIMENTEL, S. WEBER, G. MARCOS, T. CZERWIEC, I. J. R. BAUMVOL, and C. A. FIGUEROA, *J. Appl. Phys.* **105**, 124914 (2009).
- [89] O. ÖZTÜRK and D. L. WILLIAMSON, *J. Appl. Phys.* **77**, 3839 (1995).
- [90] C. BLAWERT, B. MORDIKE, Y. JIRASKOVA, and O. SCHNEEWEISS, *Surf. Coat. Technol.* **116–119**, 189 (1999).
- [91] L. GONTIJO, R. MACHADO, E. MIOLA, L. CASTELETTI, N. ALCANTARA, and P. NASCENTE, *Mater. Sci. Eng. A* **431**, 315 (2006).

- [92] Z. L. ZHANG and T. BELL, *Surface Eng.* **1**, 131 (1985).
- [93] T. CHRISTIANSEN and M. A. J. SOMERS, *Metall. Mater. Trans. A* **37A**, 675 (2006).
- [94] A. FOSSATI, F. BORGIOLI, E. GALVANETTO, and T. BACCI, *Surf. Coat. Technol.* **200**, 3511 (2006).
- [95] G. A. COLLINS, R. HUTCHINGS, K. T. SHORT, J. TENDYS, X. LI, and M. SAMANDI, *Surf. Coat. Technol.* **74–75**, 417 (1995).
- [96] A. MARTINAVIČIUS, G. ABRASONIS, W. MÖLLER, J. P. RIVIÈRE, C. TEMPLIER, A. DECLÉMY, and Y. CHUMLYAKOV, *J. Appl. Phys.* **105**, 093502 (2009).
- [97] J. BUHAGIAR and H. DONG, *In Surface Modification Technologies 21*, pp. 509–518, Valar Docs, Chennai, India, 2008.
- [98] O. ÖZTÜRK and D. L. WILLIAMSON, *Hyperfine Interactions* **92**, 1329 (1994).
- [99] M. LEI and X. ZHU, *Biomaterials* **22**, 641 (2001).
- [100] J. C. JIANG and E. I. MELETIS, *J. Appl. Phys.* **88**, 4026 (2000).
- [101] X. XIAOLEI, W. LIANG, Y. ZHIWEI, and H. ZUKUN, *Surf. Coat. Technol.* **192**, 220 (2005).
- [102] X. Y. LI, Y. SUN, and T. BELL, *Z. Metallkd.* **90**, 901 (1999).
- [103] K. ODA, N. KONDO, and K. SHIBATA, *Isij Int.* **30**, 625 (1990).
- [104] P. KIZLER, G. FROMMEYER, and R. ROSENKRANZ, *Z. Metallkd* **85**, 705 (1994).
- [105] A. MUNOZ-PAEZ, J. I. F. PERUCHENA, J. P. ESPINOS, A. JUSTO, F. CASTANEDA, S. DIAZ-MORENO, and D. T. BOWRON, *Chem. Mater.* **14**, 3220 (2002).
- [106] A. KUHL, D. BERGNER, H. J. ULLRICH, M. SCHLAUBITZ, and P. KARDUCK, *Mikrochimica Acta* **107**, 295 (1992).
- [107] H. KUWAHARA, H. MATSUOKA, J. TAKADA, S. KIKUCHI, Y. TOMII, and I. TAMURA, *Oxid. Met.* **36**, 143 (1991).
- [108] S. PARASCANDOLA, W. MÖLLER, and D. L. WILLIAMSON, *Appl. Phys. Lett.* **76**, 2194 (2000).
- [109] S. MÄNDL, *Plasma Process. Polym.* **4**, 239 (2007).
- [110] S. MÄNDL and B. RAUSCHENBACH, *J. Appl. Phys.* **91**, 9737 (2002).
- [111] G. ABRASONIS, W. MÖLLER, and X. X. MA, *Phys. Rev. Lett.* **96**, 065901 (2006).
- [112] D. MANOVA, J. GERLACH, F. SCHOLZE, S. MANDL, and H. NEUMANN, *Surf. Coat. Technol.* **204**, 2919 (2010).

- [113] T. CZERWIEC, Hdr, *Procedes de traitement thermochimique appliques aux surfaces metalliques: diagnostics des plasmas et des post-decharges et caracterisation des surfaces transformees*, 2008.
- [114] S. MÄNDL and B. RAUSCHENBACH, *J. Appl. Phys.* **88**, 3323 (2000).
- [115] S. PARASCANDOLA, O. KRUSE, E. RICHTER, and W. MOELLER, *J. Vac. Sci. Technol. B* **17**, 855 (1999).
- [116] V. I. DIMITROV, G. KNUYT, L. M. STALS, J. D'HAEN, and C. QUAEYHAEGENS, *Appl. Phys. A* **67**, 183 (1998).
- [117] S. PARASCANDOLA, *Nitrogen transport during ion nitriding of austenitic stainless steel*, PhD thesis, Forschungszentrum Rossendorf, Germany, 2001.
- [118] I. KARAMAN, H. SEHITOGLU, H. MAIER, and Y. CHUMLYAKOV, *Acta Mater.* **49**, 3919 (2001).
- [119] L. MAROT, A. STRABONI, and M. DROUET, *Surf. Coat. Technol.* **142–144**, 384 (2001).
- [120] J. PERRIERE, J. SIEJKA, N. REMILI, A. LAURENT, A. STRABONI, and B. VUILLERMOZ, *J. Appl. Phys.* **59**, 2752 (1986).
- [121] M. ZEUNER, J. MEICHSNER, H. NEUMANN, F. SCHOLZE, and F. BIGL, *J. Appl. Phys.* **80**, 611 (1996).
- [122] M. E. CHABICA, D. L. WILLIAMSON, R. WEI, and P. J. WILBUR, *Surf. Coat. Technol.* **51**, 24 (1992).
- [123] N. P. BARRADAS, S. PARASCANDOLA, B. J. SEALY, R. GRÖTZSCHEL, and U. KREISSIG, *Nucl. Instr. Meth. B* **161**, 308 (2000).
- [124] A. GURBICH and S. MOLODTSOV, *Nucl. Instr. Meth. B* **266**, 1206 (2008).
- [125] W. ANWAND, S. PARASCANDOLA, E. RICHTER, G. BRAUER, P. G. COLEMAN, and W. MÖLLER, *Nucl. Instr. Meth. B* **136–138**, 768 (1998).
- [126] D. L. WILLIAMSON, L. WANG, R. WEI, and P. J. WILBUR, *Mater. Lett.* **9**, 302 (1990).
- [127] A. L. ANKUDINOV, C. E. BOULDIN, J. J. REHR, J. SIMS, and H. HUNG, *Phys. Rev. B* **65**, 104107 (2002).
- [128] E. STERN, M. NEWVILLE, B. RAVEL, D. HASKEL, and Y. YACOBY, *Physica B* **208–209**, 117 (1995).
- [129] B. RAVEL and M. NEWVILLE, *J. Synchrotron Radiat.* **12**, 537 (2005).
- [130] L. TRÖGER, D. ARVANITIS, K. BABERSCHKE, H. MICHAELIS, U. GRIMM, and E. ZSCHECH, *Phys. Rev. B* **46**, 3283 (1992).

- [131] T. RESSLER, *J. Synchrotron Radiat.* **5**, 118 (1998).
- [132] T. GRESSMANN, M. WOHLSCHLOGEL, S. SHANG, U. WELZEL, A. LEINWEBER, E. J. MITTEMEIJER, and Z. K. LIU, *Acta Mater.* **55**, 5833 (2007).
- [133] M. SAMANDI, B. A. SHEDDEN, T. BELL, G. A. COLLINS, R. HUTCHINGS, and J. TENDYS, *J. Vac. Sci. Technol. B* **12**, 935 (1994).
- [134] F. BORGIOLI, A. FOSSATI, E. GALVANETTO, and T. BACCI, *Surf. Coat. Technol.* **200**, 2474 (2005).
- [135] C. BLAWERT, B. MORDIKE, G. COLLINS, K. SHORT, Y. JIRASKOVA, O. SCHNEEWEISS, and V. PERINA, *Surf. Coat. Technol.* **128–129**, 219 (2000).
- [136] J. STINVILLE, P. VILLECHAISE, C. TEMPLIER, J. RIVIERE, and M. DROUET, *Surf. Coat. Technol.* **204**, 1947 (2010).
- [137] S. RAO, B. HE, C. HOUSKA, and K. GRABOWSKI, *J. Appl. Phys.* **69**, 8111 (1991).
- [138] J. Y. EOM, V. S. RAO, H. S. KWON, K. S. NAM, and S. C. KWON, *J. Mater. Res.* **18**, 861 (2003).
- [139] M. KEDDAM, M. DJEGHLAL, and L. BARRALLIER, *Appl. Surf. Sci.* **242**, 369 (2005).
- [140] R. E. JONES JR., R. L. WHITE, J. L. WILLIAMS, and X.-W. QIAN, *IEEE Trans. Magn.* **29**, 3966 (1993).
- [141] M. OLZON-DIONYSIO, S. DE SOUZA, R. BASSO, and S. DE SOUZA, *Surf. Coat. Technol.* **202**, 3607 (2008).
- [142] G. N. GREAVES, P. J. DURHAM, G. DIAKUN, and P. QUINN, *Nature* **294**, 139 (1981).
- [143] J. J. KIM, H. MAKINO, M. SAKURAI, D. C. OH, T. HANADA, M. W. CHO, T. YAO, S. EMURA, and K. KOBAYASHI, *J. Vac. Sci. Technol. B* **23**, 1308 (2005).
- [144] M. HASHIMOTO, S. EMURA, H. TANAKA, T. HONMA, N. UMESAKI, S. HASEGAWA, and H. ASAHI, *J. Appl. Phys.* **100**, 103907 (2006).
- [145] A. T. PAXTON, M. SCHILFGAARDE VAN, M. MACKENZIE, and A. J. CRAVEN, *J. Phys.: Condens. Matter* **12**, 729 (2000).
- [146] R. KONINGSBERGER, D. C. AND PRINS, *X-ray Absorption; Principles, Applications, Techniques of EXAFS, SEXAFS and XANES*, John Wiley and Sons, New York, 1988.
- [147] S. KIMURA, S. EMURA, K. TOKUDA, Y. ZHOU, S. HASEGAWA, and H. ASAHI, *J. Cryst. Growth* **311**, 2046 (2009).

- [148] P. SCHILLING and R. C. TITTSWORTH, *J. Synchrotron Radiat.* **6**, 497 (1999).
- [149] P. J. SCHILLING, V. PALSHIN, R. C. TITTSWORTH, J. H. HE, and E. MA, *Phys. Rev. B* **68**, 224204 (2003).
- [150] H. MARUYAMA, *J. Synchrotron Radiat.* **8**, 125 (2001).
- [151] M. SIFKOVITS, H. SMOLINSKI, S. HELLWIG, and W. WEBER, *J. Magn. Magn. Mater.* **204**, 191 (1999).
- [152] P. SCHILLING, J.-H. HE, and E. MA, *J. Phys. IV Feance* **7**, 1221 (1997).
- [153] E. YANASE, K. ARAI, I. WATANABE, M. TAKAHASHI, and Y. DAKE, *J. Synchrotron Radiat.* **8**, 490 (2001).
- [154] B. RAVEL, *J. Alloys Compd.* **401**, 118 (2005).
- [155] S. CAMMELLI, C. DEGUELDRE, G. KURI, and J. BERTSCH, *Nucl. Instr. Meth. B* **266**, 4775 (2008).
- [156] X. Z. LI, J. ZHANG, and D. J. SELLMYER, *J. Synchrotron Radiat.* **37**, 1010 (2004).
- [157] L. CHENG, A. BOTTGER, T. DE KEIJSER, and E. MITTEMEIJER, *Scripta Metall. Mater.* **24**, 509 (1990).
- [158] F. TESSIER, A. NAVROTSKY, R. NIEWA, A. LEINWEBER, H. JACOBS, S. KIKKAWA, M. TAKAHASHI, F. KANAMARU, and F. DISALVO, *Solid State Sci.* **2**, 457 (2000).
- [159] B. K. THEO, *EXAFS: Basic Principles and Data Analysis*, Springer-Verlag, Berlin, 1986.
- [160] P. EISENBERGER and G. S. BROWN, *Solid State Commun.* **29**, 481 (1979).
- [161] M. A. J. SOMERS, R. LANKREIJER, and E. MITTEMEIJER, *Phil. Mag. A* **57**, 353 (1989).
- [162] S. J. ROTHMAN, L. J. NOWICKI, and G. E. MURCH, *J. Phys. F: Metal Phys.* **10**, 383 (1980).
- [163] J. CAHN, *Acta Metall.* **10**, 179 (1962).
- [164] Y. BABA and T. SASAKI, *Mater. Sci. Eng. A* **115**, 203 (1989).
- [165] T. SASAKI, Y. BABA, and H. YAMAMOTO, *Vacuum* **41**, 185 (1990).
- [166] K. FANCEY, A. LEYLAND, D. EGERTON, D. TORRES, and A. MATTHEWS, *Surf. Coat. Technol.* **76-77**, 694 (1995).
- [167] O. ÖZTÜRK and D. L. WILLIAMSON, *Surf. Coat. Technol.* **158**, 288 (2002).

- [168] S. SIENZ, S. MANDL, and B. RAUSCHENBACH, *Surf. Coat. Technol.* **156**, 185 (2002).
- [169] Y. JIRÁSKOVÁ, G. BRAUER, O. SCHNEEWEISS, C. BLAWERT, W. ANWAND, and P. G. COLEMAN, *Appl. Surf. Sci.* **194**, 145 (2002).
- [170] J. STINVILLE, P. VILLECHAISE, C. TEMPLIER, J. RIVIERE, and M. DROUET, *Acta Mater.* **58**, 2814 (2010).
- [171] J. P. RIVIÈRE, C. TEMPLIER, A. DECLÉMY, O. REDJDAL, Y. CHUMLYAKOV, and G. ABRASONIS, *Surf. Coat. Technol.* **201**, 8210 (2007).
- [172] H. B. HUNTINGTON, G. A. SHIRN, and E. S. WAJDA, *Phys. Rev.* **99**, 1085 (1955).
- [173] C. ZENER, *J. Appl. Phys.* **22**, 372 (1951).
- [174] D. E. JIANG and E. A. CARTER, *Phys. Rev. B* **67** (2003).
- [175] J. GATH, Master's thesis, The Technical University of Denmark, Denmark, 2007.
- [176] M. R. DAYMOND and P. J. BOUCHARD, *Metall. Mater. Trans. A* **37A**, 1863 (2006).
- [177] J. C.-M. LI, *Met. Trans. A* **9**, 1353 (1978).
- [178] K. GEMMA, T. OHTSUKA, T. FUJIWARA, and M. KAWAKAMI, *J. Mater. Sci.* **36**, 5231 (2001).
- [179] M. MANLEY, *Acta Mater.* **58**, 2926 (2010).
- [180] P. JESSNER, R. DANOIX, B. HANNOYER, and F. DANOIX, *Ultramicroscopy* **109**, 530 (2009).
- [181] J. WILDE, A. CERESO, and G. SMITH, *Scripta Mater.* **43**, 39 (2000).
- [182] A. BROKMAN and F. R. TULER, *J. Appl. Phys.* **52**, 468 (1981).
- [183] M. K. MILLER, R. E. STOLLER, and K. F. RUSSELL, *J. Nucl. Mater.* **230**, 219 (1996).
- [184] F. PLEITER and C. HOHENEMSER, *Phys. Rev. B* **25**, 106 (1982).
- [185] J. TAKAHASHI, K. KAWASAKI, K. KAWAKAMI, and M. SUGIYAMA, *Surf. Interface Anal.* **39**, 232 (2007).
- [186] M. MEYERS and K. CHAWLA, *Mechanical Behavior of Materials*, Prentice Hall, USA, 1999.
- [187] C. FOERSTER, J. SOUZA, C. SILVA, M. UEDA, N. KUROMOTO, F. SERBENA, S. SILVA, and C. LEPIENSKI, *Nucl. Instr. Meth. B* **257**, 727 (2007).

- [188] C. FOERSTER, F. SERBENA, S. DA SILVA, C. LEPIENSKI, C. DE M. SIQUEIRA, and M. UEDA, *Nucl. Instr. Meth. B* **257**, 732 (2007).
- [189] M. SCHRÖTER, H. EBERT, H. AKAI, P. ENTEL, E. HOFFMANN, and G. G. REDDY, *Phys. Rev. B* **52**, 188 (1995).
- [190] A. V. RUBAN, S. KHMELEVSKYI, P. MOHN, and B. JOHANSSON, *Phys. Rev. B* **76**, 14420 (2007).
- [191] Y. KONG, J. PELZL, and F. LI, *J. Magn. Magn. Mater.* **195**, 483 (1999).
- [192] S. MATAR, B. SIBERCHICOT, M. PENICAUD, and G. DEMAZEAU, *J. Phys. I* **2**, 1819 (1992).
- [193] K. H. EICKEL and W. PITSCH, *Phys. Status Solidi* **39**, 121 (1970).
- [194] T. CZERWIEC, H. HE, G. MARCOS, T. THIRIET, S. WEBER, and H. MICHEL, *Plasma Process. Polym.* **6**, 401 (2009).
- [195] I. OZBEK and C. BINDAL, *Surf. Coat. Technol.* **154**, 14 (2002).
- [196] T. GRAHAM, *Philosophical Transactions of the Royal Society of London* **156**, 399 (1866).
- [197] H. IBA and E. AKIBA, *J. Alloys Compd.* **253–254**, 21 (1997).

Erklärung

Hiermit versichere ich, dass ich die vorliegende Arbeit ohne unzulässige Hilfe Dritter und ohne Benutzung anderer als der angegebenen Hilfsmittel angefertigt habe. Die aus fremden Quellen direkt oder indirekt übernommenen Gedanken sind als solche kenntlich gemacht. Die Arbeit wurde bisher weder im Inland noch im Ausland in gleicher oder ähnlicher Form einer anderen Prüfungsbehörde vorgelegt.

Diese Dissertation wurde angefertigt im

Forschungszentrum Dresden-Rossendorf
Institut für Ionenstrahlphysik und Materialforschung
Postfach 51 01 19
01314 Dresden

Die wissenschaftliche Betreuung der Arbeit erfolgte durch Prof. Dr. Wolfhard Möller.

Ich versichere, an keiner Institution, auch nicht im Ausland, jemals den Antrag auf Eröffnung eines Promotionsverfahrens gestellt zu haben.

Ich erkenne die Promotionsordnung der Fakultät Mathematik und Naturwissenschaften der Technischen Universität Dresden an.

Andrius Martinavičius
Dresden, October 2010